공학박사학위논문

제습제 코팅 열교환기를 적용한 전기 자동차용 히트펌프 시스템 성능 분석

Performance analysis of a heat pump system with a desiccant coated heat exchanger for an electric vehicle

2021년 8월

서울대학교 대학원

기계항공공학부

나 선 익

제습제 코팅 열교환기를 적용한 전기자동차용 히트펌프 시스템 성능 분석

Performance analysis of a heat pump system with a desiccant coated heat exchanger for an electric vehicle

지도교수 김 민 수

이 논문을 공학박사 학위논문으로 제출함

2021 년 4 월

서울대학교 대학원

기계항공공학부

나 선 익

나선익의 공학박사 학위논문을 인준함

2021 년 6 월

위 원 장 : 민 경 덕

부위원장 : 김 민 수

위 원 : 송 한 호

위 원 : 도 형 록

위 원 : 김 민 성

Abstract

Performance analysis of a heat pump system with a desiccant coated heat exchanger for an electric vehicle

NA, Sun-Ik
Department of Mechanical and Aerospace Engineering
The Graduate School
Seoul National University

In this study, a heat pump system of an electric vehicle (EV) with a novel dehumidifier is suggested and validated by modeling and experiment. The aim of the study is the determination of the energy consumption of the proposed system.

The driving range of a conventional EV sharply drops when operating the MHP system for heating or defogging. Because the traditional MHP consumes a lot of energy since it used the condensing method to remove moisture. It

means that the air temperature must be lower than dew points to occurs condensation on the metal fins of a heat exchanger, then the air should be reheated to supply into the cabin. In this study, to solve this irrational process for dehumidification, a solid desiccant coated heat exchanger (DCHE) is introduced which is able to heat and mass transfer simultaneously for removing water vapor in the cabin air and recovering waste heat from power electronics and electric machineries (PEEM).

To attach the desiccant material onto the metal fin of a heat exchanger, a binder should be necessary. Thus, the proper pair of the desiccant and binder is selected. After analyzing the physical properties of the adsorbent, the optimum binder contents ratio is obtained. Then, the numerical model of the DCHE was developed base on the thermal resistance method to predict the adsorption performance of the DCHE. To validate the predicted results, the DCHE was fabricated and the test facility was also constructed. The simulation results show good agreement with the experimental data.

To obtain the power consumption of the MHP, the numerical model of the MHP was developed. The compressor characteristics were determined by preliminary test since it is a crucial component of the MHP and it strongly affects the performance of the MHP system. Similar to the DCHE model, heat exchangers of the MHP also modeled using the thermal resistance method by

discrete as small segments. To validate the developed MHP model, the experimental apparatus was constructed and conducted experiments. As a result, the simulation results reveal small differences as compared with the experimental data.

Owing to determine the effect of the DCHE on the energy consumption of the MHP to satisfy the cabin target condition, the simulation was conducted by integrated the developed numerical model in the Simulink program. Simulation results reveal that the system with DCHE achieves a reduction in energy consumption as compared to the traditional system. Because the DCHE led to decreasing the operation time of the MHP by adsorption the water vapor in the cabin air, and by heating to approach the cabin air temperature to the setpoint.

In conclusion, the novel configuration which is utilized the DCHE in the automobile heat pump system is suggested in this study. And the DCHE effects on the energy reduction of the automobile heat pump system were investigated. Conclusively, the DCHE helps to reduce energy consumption.

Keyword: Desiccant coated heat exchanger (DCHE), Electric vehicle (EV), Heat pump, Dehumidification, Heating

Student Number: 2017-36824

Contents

List of Figures

List of Tables

Nomenclature

a	Specific area $[\mathrm{m}^2 \cdot \mathrm{g}]$
A	Area $[\mathrm{m}^2]$
C	Constant $[-]$
c_p	Specific heat capacity $[\mathrm{kJ} \cdot \mathrm{kg}^{-1} \cdot \mathrm{K}^{-1}]$
C_w	Water contents in a specific desiccant material $[\mathrm{kg_w} \cdot \mathrm{kg_d^{-1}}]$
COP	Coefficient of performance $[-]$
D_h	Hydraulic diameter $[\mathrm{m}]$
d_{pore}	Pore diameter $[\mathrm{m}]$
D_{va}	Binary diffusivity of water vapor in the air $[\mathrm{m}^2 \cdot \mathrm{s}^{-1}]$
D_{vd}	Overall diffusion coefficient in the desiccant $[\mathrm{m}^2 \cdot \mathrm{s}^{-1}]$
D_{vK}	Knudsen diffusivity $[\mathrm{m}^2 \cdot \mathrm{s}^{-1}]$
D_{vm}	Molecular diffusivity $[\mathrm{m}^2 \cdot \mathrm{s}^{-1}]$
D_{vp}^*	Effective pore diffusion coefficient $[\mathrm{m}^2 \cdot \mathrm{s}^{-1}]$
D_{vs}^*	Effective surface diffusion coefficient $[\mathrm{m}^2 \cdot \mathrm{s}^{-1}]$
E_m	Metabolic rate $[\mathrm{W}]$
f	Friction factor $[\mathrm{Pa} \cdot \mathrm{m}^{-1}]$
h^H	Heat transfer coefficient $[\mathrm{W} \cdot \mathrm{m}^{-2} \cdot \mathrm{K}^{-1}]$
h^M	Mass transfer coefficient $[\mathrm{m} \cdot \mathrm{s}^{-1}]$

i	Specific enthalpy $[\mathrm{kJ} \cdot \mathrm{kg}^{-1}]$
i_{fg}	Specific enthalpy of condensation/vaporization $[\mathrm{kJ} \cdot \mathrm{kg}^{-1}]$
k	Thermal conductivity $[\mathrm{W} \cdot \mathrm{m}^{-1} \cdot \mathrm{K}^{-1}]$
M	Molar mass $[\mathrm{kg} \cdot \mathrm{mol}^{-1}]$
$m, \dot{m}$	Mass [kg], mass flow rate $[\mathrm{kg} \cdot \mathrm{s}^{-1}]$
n	Specific volume $[\mathrm{m}^3 \cdot \mathrm{kg}^{-1}]$
N	Number, count
P, p	Pressure [Pa]
$Q, \dot{Q}$	Heat [J], heat transfer rate [W]
r	Radius [m]
R	Thermal resistance $[\mathrm{K} \cdot \mathrm{W}^{-1}]$
R^*	Gas constant
t	Time [s]
T	Temperature [°C]
U	Overall heat transfer coefficient $[\mathrm{W} \cdot \mathrm{K}^{-1}]$
V	Velocity $[\mathrm{m} \cdot \mathrm{s}^{-1}]$
v^{diff}	Diffusion volume
Vol	Volumetric $[\mathrm{m}^3]$
w	Air humidity ratio $[\mathrm{kg}_w \cdot \mathrm{kg}_{\mathrm{DA}}^{-1}]$
$W, \dot{W}$	Work [J], work rate [W]

Y	Thermal sensation $[-]$

Greek

δ	Error
γ	Surface tension
ε	Effectiveness
ε_d	Desiccant porosity
η_{isen}	Isentropic efficiency
η_{mech}	Mechanical efficiency
η_{vol}	Volumetric efficiency
μ	Dynamic viscosity
ρ	Density
ψ	Dimensionless ratio
ϕ	Relative humidity

Subscript

a	Air
car	Vehicle
$COMP$	Compressor
$COND$	Condenser

$conv$	Convective
CV	Control volume
d	Desiccant
D	Dehumidification
$DCHE$	Desiccant coated heat exchanger
EA	Exhaust air
eq	Equivalent
f	Fin
H	Heating
in	Inside, inlet
f	Fin
inf	Infiltration
m	Monolayer
men	Human
OA	Outdoor air
out	Outside, outlet
r	Refrigerant
R	Regeneration
RA	Return air
SA	Supply air

sat	Saturated
sol	Solar
t	Tube
v	Water vapor
V	Vapor phase
w	Water, coolant
x	Quality

Chapter 1. Introduction

1.1. The motivation of the study

Human being has overconsumed natural resource. Now, we need solutions and practical action. Since the Industrial Revolution, humidity has over-consumed to flourish the economy by pursuing a high-grow rate with less consideration about the byproduct which negative impact on the global ecosystem. Thus, the environment has rapidly changed and it is the gravest threat to not only mankind but also lives on the Earth. The annual mean global surface temperature has increased by more than 1℃ compare with the pre-industrial level, and two-thirds of global warming has occurred since 1975 [1]. Moreover, the global temperature is expected to further rise by at least 1℃ by 2024 [2]. This means that recently, the climate has been changing even more quickly. According to the Intergovernmental Panel on Climate Change (IPCC) fifth assessment report (AR5) [3], global warming might have led to an increase in the frequency and duration of a marine heatwave, sea level, and intensity of heavy precipitation events. It causes a huge impact ecosystem and becomes a risk for food security, poverty, furthermore health, well-being, and land uses.

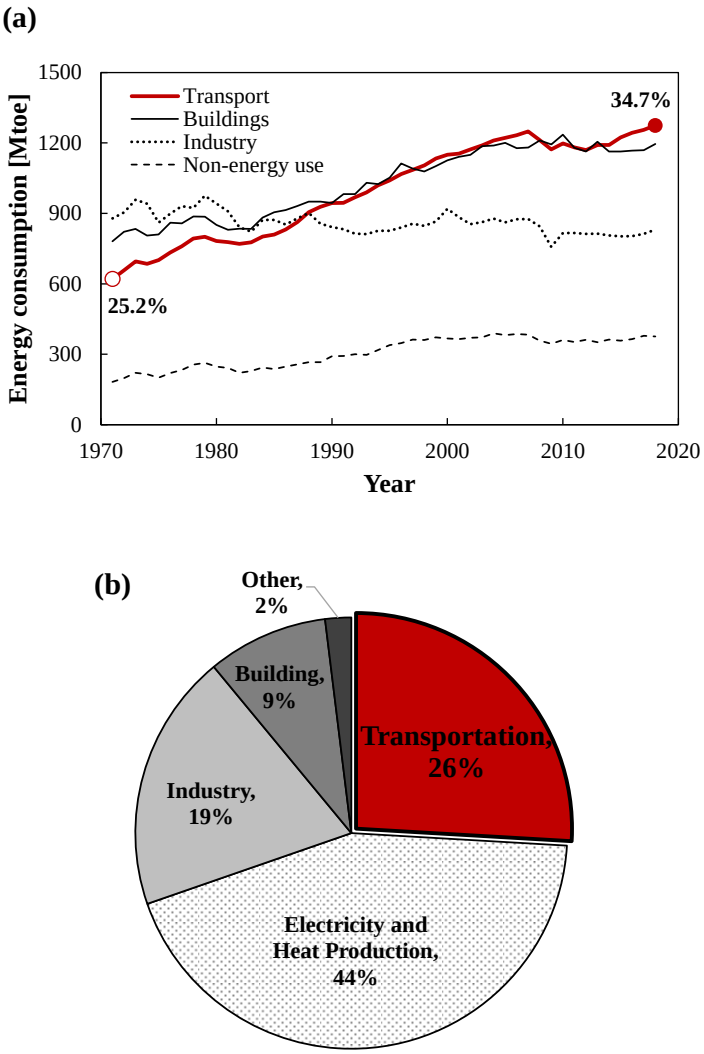

Figure 1.1 Portion of the transportation sector on the energy consumption and CO_2 emissions; (a) Comprehensive energy balances for all the world's energy-consuming of over 180 countries [4], (b) Global CO_2 emissions by sector from fuel combustion [5].

In order to restrain global warming, many countries have enacted strict environmental regulations for conventional internal combustion vehicles that emit greenhouse gases, such as CO_2. Moreover, more than 14 countries have decided that they will ban the sale of petrol and diesel cars by the 2040s. Because transportation consumptions have increased since the 1970s up to about 35% of total energy consumption [4] and the transportation sector is responsible for a quarter of the global CO_2 emission from fuel combustion [5] as depicted in **Figure 1.1**. In these circumstances, car makers are presenting their visions of phasing out internal combustion engines (ICE) to avoid regulation and protect the environment. Instead, electric vehicle (EV) manufacturing capacity is being expanded, and sales have been increasing rapidly in global markets [6, 7].

The typical heat pump system in an electric vehicle is composed of a refrigerant compressor, heat exchangers, and expansion device as shown in **Figure 1.2**. In order to facilitate air inflow when the vehicle is running, the outdoor heat exchanger is located in front of the vehicle. And indoor heat exchangers such as indoor evaporator (IDEVA) and indoor condenser (IDCOND) are installed near the driver seat. In a future EV, the space for an HVAC system might be enlarged due to the conventional engine room will be vanished.

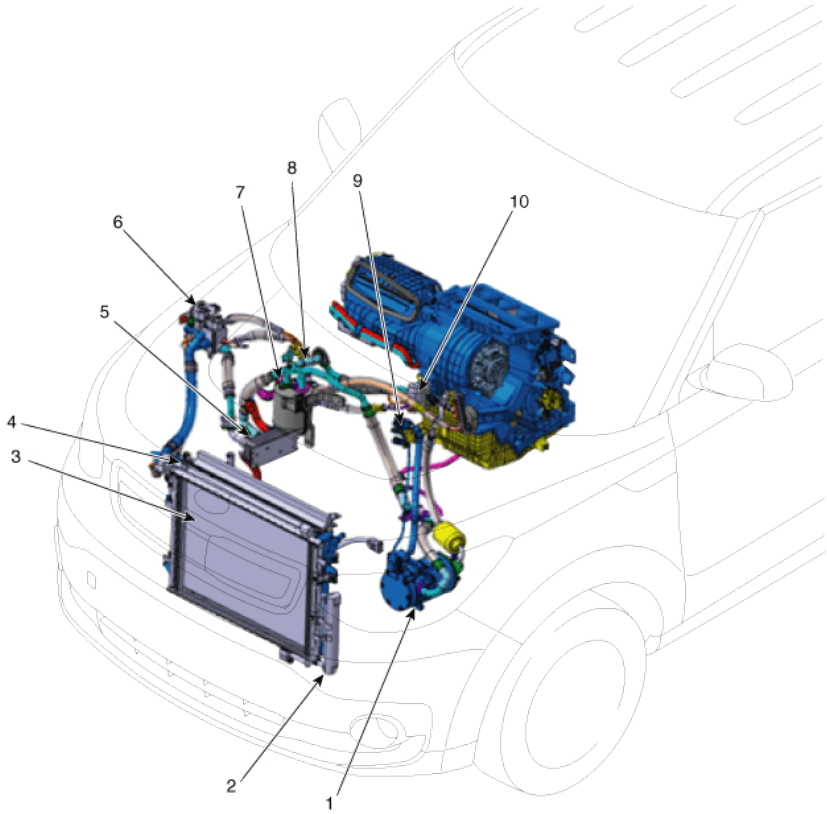

Figure 1.2 Component location of the automobile heat pump system in the KIA Soul EV [8]; (1) Compressor, (2) Reciever-drier, (3) outdoor heat exchanger (exterior condenser), (4) refrigerant temperature sensor #1, (5) internal heat exchanger (chiller), (6) 3 ways solenoid valve assembly, (7) accumulator, (8) 2 ways solenoid valve assembly, (9) refrigerant temperature sensor #2, (10) expansion valve.

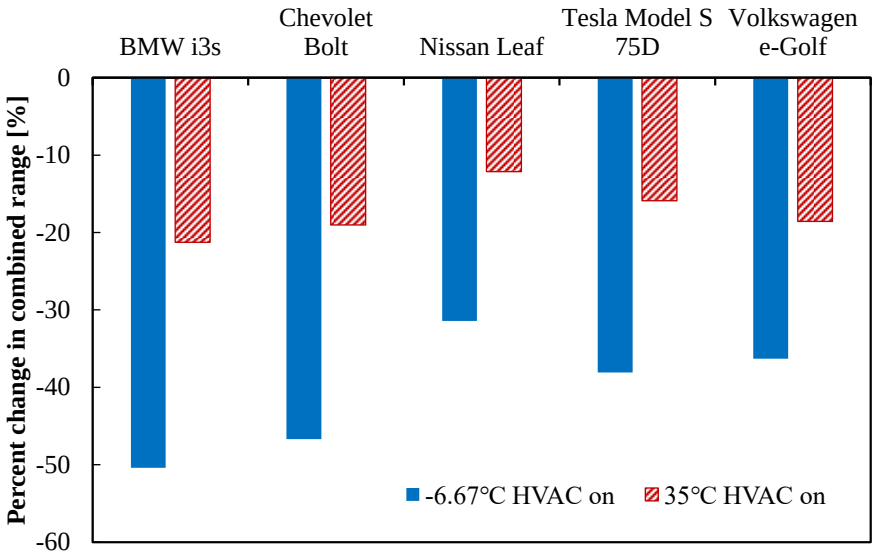

Figure 1.3 Percent change in combined driving range relative to testing conducted at 23.9ºC [9].

In particular, when an automotive heat pump system (MHP) consumes a lot of energy to deal with the heating loads in winter seasons, this causes a drastic decrease in the driving distance of the electric vehicle [9-11] as shown in **Figure 1.3**. This is one of the barriers to purchasing an EV instead of a conventional internal combustion vehicle, due to anxiety [12]. To solve the problem, installing more battery packs in the EV seems to be an inappropriate solution. Because it would cause price rise and vehicle weight increase, which leads to a reduction in the range and efficiency. Therefore, it is necessary to reduce energy consumption for both air heating and defogging. The water vapor contained in the occupant's exhaled air forms fog on the window during cold weather conditions. The fog interferes with safe driving, therefore must be removed, which represents a large portion of heating loads. To heat the air, the outdoor heat exchanger (ODHX) plays the role of an evaporator during heating mode in a conventional system, as shown in **Figure 1.4(a)**. When the windshield temperature is lower than the dew point, fog will form on the window, and the dehumidification process will operate. A traditional method for removing moisture in the air, especially in a vehicle, is that air temperature drops to below dew point, and then water vapor in the air condenses at the indoor evaporator (IDEVA), as shown in **Figure 1.4(b)**.

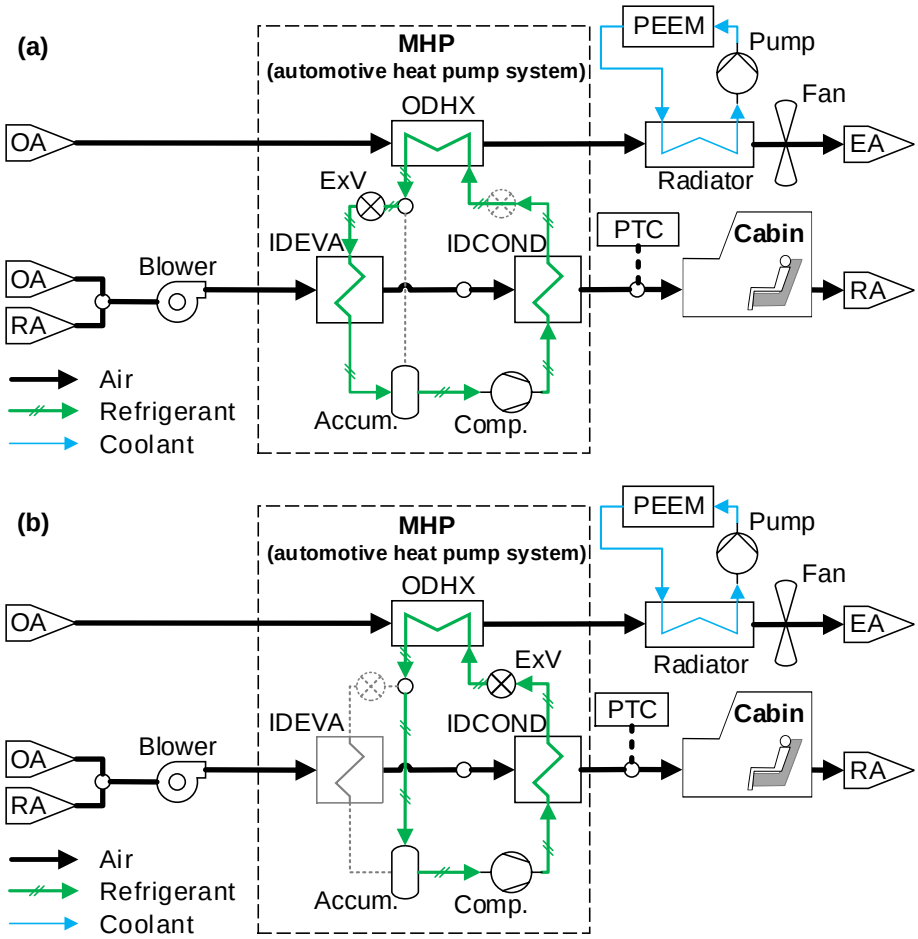

Figure 1.4 Diagram of the conventional automotive heat pump system for (a) Condensing mode, and (b) Heating mode.

But the dehumidified air needs heating again to supply the cabin since the air temperature is too low; thereby inevitably a lot of energy is required to conduct the condensing method, as shown in **Figure 1.5**. In contrast with the condensing method, the solid desiccant dehumidification has merit for saving energy because the water vapor is directly captured into the adsorbent without unnecessary cooling and re-heating processes.

The enthalpy of supplied air should be reduced upon the adsorption process according to the enthalpy relation with Gibbs free energy and the entropy is given by **Eq. (1.1)**. Because the change of entropy of the supplied air is negative since the degree of translational freedom of adsorptive in gaseous might be reduced when it is attached to the surface. And the Gibbs free energy is negative since the adsorption process is spontaneous unless the adsorbent is saturated.

$$\Delta H = \Delta G + T\Delta S \qquad \text{Eq. (1.1)}$$

Solid desiccant has the other strength, not only the decreasing the enthalpy of the supplier air, but also it is able to use heat sources at the low-temperature region of around 60°C when releasing the moisture, i.e. regeneration. Because the solid desiccant, such as silica-gel, adsorbs water molecules by weak electrostatic force, e.g., van der Waals force.

Another way to reduce energy consumption for heating is that a compressor operates under favorable conditions by heat recovery. The reason is that the compressor is the most energy-consuming device in the MHP, and it tends to require less energy by decreasing the pressure ratio as the evaporating temperature rises. Therefore, the waste heat from the power electronics and electric machineries (PEEM), such as motors, inverters, and batteries, should be recovered by heat transfer to the refrigerant cycle, using an additional heat exchanger.

To satisfy the abovementioned requirements, which are simultaneous heat and mass transfer, this study introduces the desiccant coated heat exchanger (DCHE). As the name suggests, the DCHE is a heat exchanger that has absorbents attached to the fins. And then, the energy analysis should be conducted to determine the effect of the DCHE on the electric vehicle.

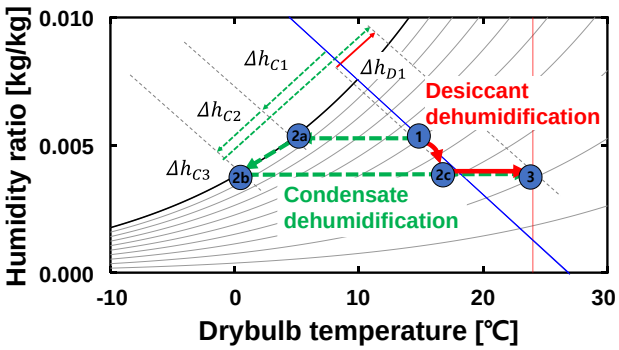

Figure 1.5 Progress according to the condensate dehumidification and desiccant dehumidification on the psychometric chart.

1.2. Literature survey

1.2.1. Desiccant coated heat exchanger

Desiccant technologies have been developed in the building field. Because the energy contribution from buildings is almost 40% of the total energy consumption in the world [13]. Among the building energy, 70% of it is a latent component [14]. Hence, dehumidification technologies are utilized to reduce energy consumption. For instance, the fixed-bed and the rotary type desiccant dehumidifiers are widely used in a building. Pennington introduced the coupled system with a dehumidifier, a regenerator, and double regenerative evaporative coolers [15]. Munters improved Pennington's system by utilizing parallel passages [16]. Dunkle built rotary wheels to increase the capacity and efficiency of the dehumidification system [17].

To improve the performance of the adsorption, inter-cooling technologies have been considered during the dehumidification process. Worek and Moon proposed the potential of desiccant integrated into a vapor compression system by conducting theoretical analysis [18]. Dhar also shows the energy saving of a desiccant integrating system as a simulation [19]. Ge *et al.* experimented to determine the effect of internal cooling during dehumidification [20]. Before attracting attention to the DCHE, a hybrid desiccant-assisted pre-conditioner

and split cooling coil system have developed [21, 22]. The hybrid system was designed to control not only moisture removal by desiccant but also sensible heat removal by a cooling coil. But the hybrid system was worked by the liquid desiccant, thereby, it has vessels for desorption (also known as the regeneration) under vacuum conditions. The vacuum system is hardly fabricated in small size. It is not a severe problem for the stationary system that has less limitation of the install space. Meanwhile, the automobile is usually required that the system should be compact or multifunction to overcome its insufficient volume.

The DCHE was introduced to enhanced adsorption performance by cooling the solid adsorbent under atmospheric air pressure. To ensure the feasibility and to enhance the performance, the research about the DCHE has been widely conducted as classified in **Figure 1.6**. Some of the research has been studied about the coated desiccant material since the dehumidification performance depends on the sorption characteristic of it. Not only the material technologies but also the fabricating method of the DCHE have been developed to improve its performance. Ng *et al.* determined the thermodynamic characteristics of the silica gel-water working pair by experiment [23]. Ge *et al.* reported that the silica type adsorbent performs better than the general polymer type desiccant [20], and by comparing experimental results, suggested the method of impregnating potassium formate into silica gel to improve adsorption

capacity [24]. Restuccia *et al.* tested the adsorption chiller using by applying hydrophobic Y zeolite. But, it was designed to use methanol as adsorbate, not water vapor [25]. Vivekh *et al.* developed a new composite desiccant, based on super absorbent polymer and anhydrous lithium chloride powder, which showed enhanced water sorption capacity [26]. Fang *et al.* suggested that the lithium and magnesium modified ion exchanger resin is a good candidate for adsorption material to fabricate the DCHE [27]. Park and Lee investigated the heat and mass transfer coefficient characteristics for a zeolite-coated heat exchanger [28]. Aung *et al.* conducted experiments using zeolite FAM Z01 as an adsorbent for an adsorption chiller [29]. Even though the Fe-substituted material from aluminophosphate $AlPO_4$-5 (known as $FAPO_4$-5) shows the good adsorption performance, the deliquescence of adsorbents is able to corrosion the metal fin of the DCHE [30].

Many research groups have performed studied numerical studies to predict the performance of the DCHE. Hua *et al.* parametric analysis using graphic general solution based on dimensionless indexes [31]. Liu *et al.* suggested the numerical model of the air-cooled DCHE which is similar to the rotary wheel [32]. Hua *et al.* developed a three-dimensional mathematical model to predict the performance of the DCHE [33]. Higashi *et al.* analyzed the mass and heat transfer of the DCHE by theoretical calculation [34]. Tu *et al.* developed a

numerical model considering the thermal inertial of the DCHE since it might affect the transient thermal response of the DCHE [35].

Hitherto the DCHE has been studied for application in building heating, ventilation, and air conditioning (HVAC) [36, 37]. However, there have been few studies on the DCHE system applied to a vehicle. Suzuki suggested the design idea of the application of an adsorption cooling system to an automobile [38]. Vasta *et al.* conducted the lab-test of a mobile adsorption air-conditioner using a heat exchanger filled with adsorbent grains, rather than directly coated metallic fin [39]. However, they have not researched to investigate the effect of the DCHE with the heat pump system to deal with cabin thermal load. Alahmer calculated a cooling load of a cabin simply, but he only considered a rotary desiccant wheel for dehumidification [40].

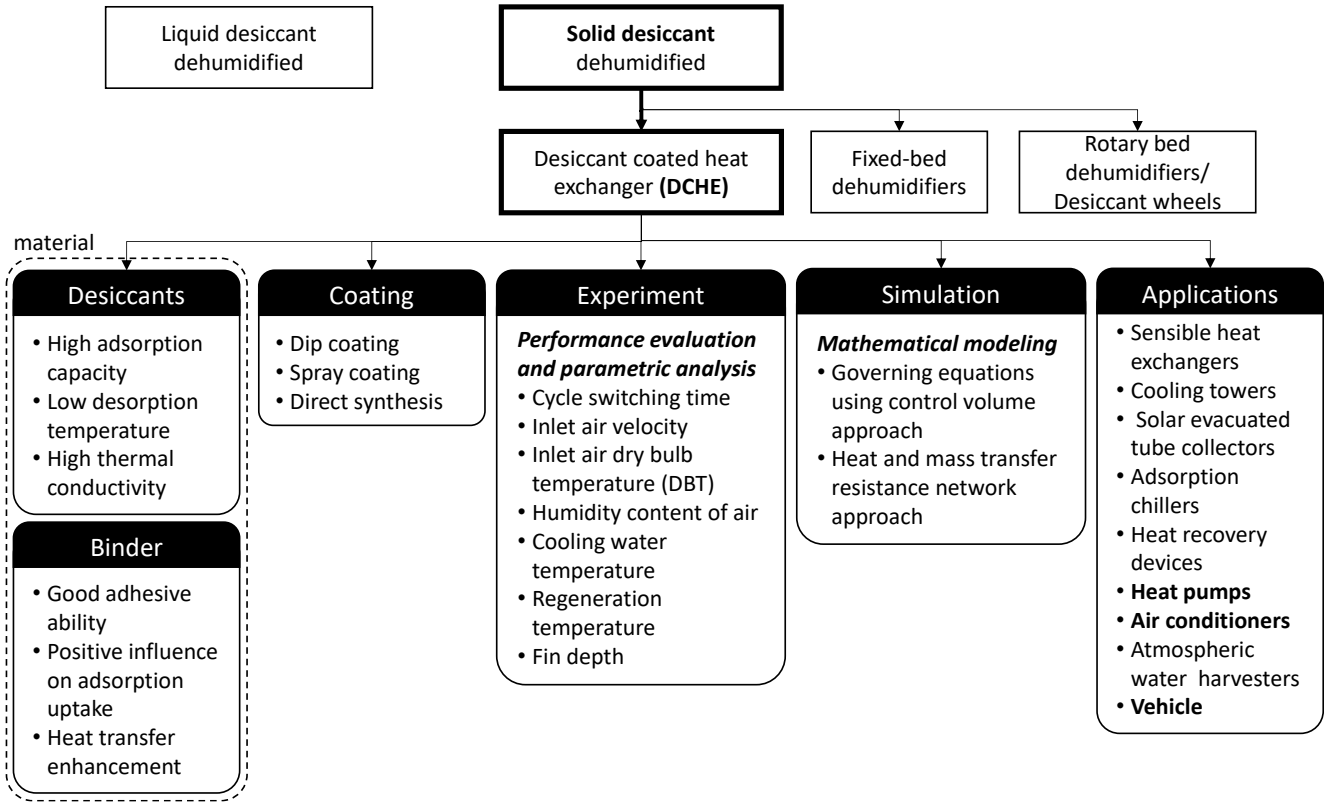

Figure 1.6 Classification related to the DCHE research.

1.3. Objectives and scopes

In order to investigate the energy consumption of the integrated system which is combined with the automobile heat pump system and a desiccant coated heat exchanger, it is essential to construct a cabin thermal model, a vapor compression cycle model, and a desiccant coated heat exchanger model.

In Chapter 2, the thermal load of an electric vehicle cabin was obtained by using a developed numerical model. The thermodynamic and physical properties of the moist air are calculated according to relative humidity. The cabin thermal model was validated by comparing it with the result of another research group. After that, the heating load was calculated on various predefined conditions such as the number of passengers or the driving velocity profile of the vehicle.

Chapter 3 presents the desiccant-coated heat exchanger. The adsorption principle is briefly addressed in the first section of the chapter. Then, the pair of desiccant and binder was investigated according to the content ratio of the binder. The physical properties of the adsorbent are obtained by various measurement methods. For instance, the surface area and volume were determined by the BET method. Owing to acquire the water vapor adsorption performance of the adsorbent, the adsorption test was conducted by the vapor

sorption volumetric gas sorption analyzer. Then, the numerical model of the additional heat exchanger was constructed by divided small elements using thermal resistances. To validate the developed model, the experimental apparatus was fabricated. Compare with the simulation result and experimental data, the DCHE model was validated.

Chapter 4 is discussed that the numerical model of the vapor compression cycle for an electric vehicle was developed. To construct the numerical model of the heat pump system, heat exchangers such as the outdoor heat exchanger, the indoor evaporator, and the indoor condenser are also evaluated and vitrificated. To validate the developed numerical model of the heat pump system, experimental research was also conducted. Under the standard testing condition, the performance of the experimental heat pump system was measured on various charge amounts of the refrigerant. The conventional automobile heat pump system used the R-134a as a refrigerant. But it must be phased out due to its high global warming potential. Thus, the alternative refrigerant was considered by thermodynamic analysis. To match up with the alternative refrigerant, the lubricant candidate was also discussed. Owing to observing the effect of changing refrigerant type, the experiment was conducted. After that, the developed numerical model of the automobile heat pump system is validated by comparing with the experimental data and the simulation result.

Finally, in Chapter 5, the energy analysis of the overall system is discussed. The energy consumption of the automobile heat pump for an electric vehicle was simulated using the developed numerical model by integrating on the Simulink. To utilize the DCHE in the conventional automobile heat pump system, a configuration is suggested in this study. Owing to the effect of the additional heat exchanger on energy consumption, the simulation was conducted on various operating conditions. To overcome the intermittent dehumidification process of the suggested configuration which used a single DCHE, the system was modified to operate continuously by using double DCHE. And the energy analysis of the system was also conducted.

Chapter 2. Electric vehicle thermal loads analysis

2.1. Introduction of the cabin model

In order to determine the energy consumption of the automobile heat pump (MHP) system, the cabin thermal model is essential evaluated. Because the MHP should work to satisfy the thermal load. Hence, the energy consumption of MHP is strongly dependent on the thermal load of the cabin.

Many research groups have been developed the cabin model to meet their purposes. Huang [41] developed the mathematical cabin model considering the thermal load from solar, and passengers. His model is composed of four coupled nonlinear ordinary differential equations. Two energy balance equations are related to air and interior mass, the other equations are for the mass balance of dry air and moisture. Gado [42] built the test facility to investigate the dynamic performance of a typical automobile air-conditioning system. And he developed the cabin model as compared with experimental data which is obtained from a test facility. And his model is compared with Huang's cabin model to validate. Brèque and Nemer [43] consider the conduction, convection, radiation heat transfer as well as the mass balance of the water vapor in the passenger compartment. Rugh *et al.* [44] determined the overall heat transfer coefficient of the vehicle metal body by experiment. And they argued that the solar

reflective film helps to decrease the cooling load by reducing the solar energy into the cabin. Similarly, Levinson *et al.* [45] suggested the cabin model for investigating the effect of vehicle color on solar heat gain. However, they focused on the cooling load according to the solar heat gain. Khayyam *et al.* [46] studied the cabin model which is considered the metabolic heat load, direct solar radiation load, diffuse solar radiation load, reflected radiation load, and engine heat load. He adopted the PID controller for energy management by controlling the air temperature and the air flow rate. But he was only considered energy balance but he had not focused on moisture mass balance accurately. Recently, Kim developed the cabin model to simulate an integrated electric vehicle thermal management system (TMS) [47]. However, this cabin model is insufficient consideration about the water generation from the human body.

In this study, the cabin model should be evaluated and modified not only energy balance but also moisture mass balance to investigate moisture effect on the passenger compartment based on Kim's cabin model [47].

2.2. Numerical model of the cabin thermal load

The cabin model is constructed to determine the thermal load that requires energy to attain thermal comfort for the driver and passenger. The model would

interact with the performance of the automobile heat pump (MHP). For this purpose, the cabin model was developed using mass and energy balance, as depicted in **Figure 2.1**. The mass balance of air and water vapor is calculated in **Eq. (2.1)** and **Eq. (2.2)**. And the energy balance of air in the cabin and interior was derived using the first law of thermodynamics as in **Eq. (2.3)** and **Eq. (2.4)** under the assumptions that the air kinetic and potential energies are negligible [47]. And the energy and mass distribution are postulated evenly in a cabin. The nonlinear ordinary differential equations were solved to obtain the thermal load of the cabin. The cabin thermal load depends not only on the environmental conditions but also on the human metabolic rate and vehicle driving speed. It is summarized that the physical and thermodynamic properties of a vehicle such as a cabin air volume, outer surface area, and heat transfer coefficients in **Table 2.1**.

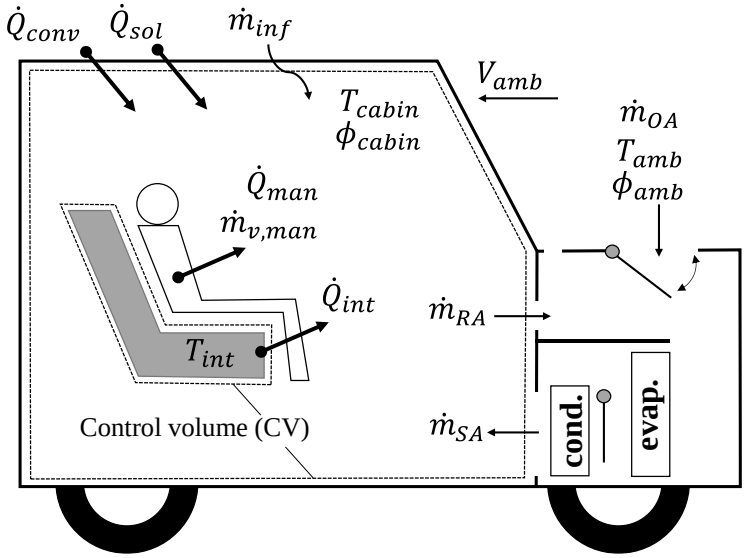

Figure 2.1 Schematic of the cabin model.

$$\frac{dm_{a,CV}}{dt} = \dot{m}_{a,inf} + \dot{m}_{SA} - \dot{m}_{RA} = 0 \qquad \text{Eq. (2.1)}$$

$$\frac{d}{dt}(m_{CV}w_{CV}) = (\dot{m}_a w)_{SA} + (\dot{m}_a w)_{inf} + \dot{m}_{v,man} - (\dot{m}_a w)_{RA} \qquad \text{Eq. (2.2)}$$

$$\frac{d}{dt}(m_a i) = \Omega \cdot \dot{Q}_{sol} + \dot{Q}_{conv} + \dot{Q}_{men} + \dot{Q}_{inte} + (\dot{m}_a i)_{inf} + (\dot{m}_a i)_{SA} - (\dot{m}_a i)_{RA} \qquad \text{Eq. (2.3)}$$

$$(mc_p)_{inte}\frac{dT_{inte}}{dt} = (1-\Omega)\cdot \dot{Q}_{sol} - \dot{Q}_{inte} \qquad \text{Eq. (2.4)}$$

where, Ω is the absorbing ratio of solar energy into cabin air, and $\dot{Q}_{sol}$ is the solar radiation. In **Eq. (2.3)**, $\dot{Q}_{conv}$ represents the convection heat transfer rate between outside air that is calculated as **Eq. (2.5)**.

$$\dot{Q}_{conv} = U_{conv}A_{car,outer}(T_{cabin} - T_{OA}) \qquad \text{Eq. (2.5)}$$

$$\dot{Q}_{men} = A_{manskin}\left[E_{m,driver} + (N \cdot E_m)_{companion}\right] \qquad \text{Eq. (2.6)}$$

$$\dot{Q}_{inte} = U_{inte}A_{inte}(T_{inte} - T_{cabin}) \qquad \text{Eq. (2.7)}$$

The metabolic heat of passengers ($\dot{Q}_{men}$) is calculated by **Eq. (2.6)**. The metabolic rates of a driver ($E_{m,driver}$) and a fellow passenger ($E_{m,companion}$) are 87.3 and 58.2 W/m^2, respectively. The skin surface area of a human body, $A_{manskin}$ [m^2], is relative with the weight and height as proposed in **Eq. (2.8)** [48]. In this study, all passenger's weight and height are sat as 170 cm, 70 kg, thus the skin surface area of a passenger, $A_{manskin}$, is 1.8 m^2.

$$A_{manskin} = 71.84 \cdot 10^{-4} \cdot m_{\text{man}}^{0.425} \cdot H_{\text{man}}^{0.725} \quad \text{Eq. (2.8)}$$

Water moisture releases from the human body during breath or evaporates from the skin. An adult generates humidity in a range from 20 to 180 g/h depends on various conditions [49]. Approximately, an adult insensibly losses about 45 ml of water per hour [50], 0.6 to 2.3 L per day [51] from the body through respiration and evaporation. To estimate the water generation from passengers in a vehicle, the water loss rate from the human body is obtained by **Eq. (2.9)** subjected to the number of passengers and their activities. The respiration rate ($\dot{m}_{res}$ [kg_{air}/s]) is a function of metabolic rate as shown in **Eq. (2.10)** [52]. The water content in the exhaled air ($\breve{m}_{v,res}$ [kg/kg_{air}]) is depended on the inspired air temperature as following in **Eq. (2.11)** [53]. Plus, the evaporated water from the skin of a passenger ($\dot{m}_{v,skin}$) is able to obtain by multiply the average value of the transepidermal water loss ($\overline{\text{TWEL}}$), skin area, and the number of passengers as described in **Eq. (2.12)** [54].

$$\dot{m}_{v,men} = \bar{m}_{v,res} \cdot \dot{m}_{res} + \dot{m}_{v,skin} \quad \text{Eq. (2.9)}$$

$$\dot{m}_{res} = 2.58 \cdot 10^{-6} \cdot \left[E_{m,driver} + (N \cdot E_m)_{companion}\right] \quad \text{Eq. (2.10)}$$

$$\breve{m}_{v,res} = [23.38 + 0.165 \cdot (T_{cabin} - 273.15)] \cdot 10^{-3} \quad \text{Eq. (2.11)}$$

$$\dot{m}_{v,skin} = \overline{\text{TWEL}} \cdot A_{manskin}\left(N_{dirver} + N_{companion}\right) \quad \text{Eq. (2.12)}$$

To determine the time of the fogging up, the windshield temperature should be obtained. Thus, the window temperature of the cabin side is

calculated as following **Eq. (2.13)**. The overall heat transfer coefficient of the vehicle is an empirical correlation according to the car velocity [55] as shown in **Eq. (2.14)**. In the part of the glass, the constant heat transfer coefficient is used under the assumption that the air mass flow rate maintains uniformity [56].

$$T_{window,inside} = T_{cabin} - \frac{U_{overall}}{U_{inside}}(T_{cabin} - T_{OA}) \quad \text{Eq. (2.13)}$$

$$U_{overall} = 2.996\mathrm{V}^{0.0708} \quad \text{Eq. (2.14)}$$

The mixing ratio of outdoor air (ψ_{OA}) is defined as the ratio of the outside air mass flow rate to supply the air mass flow rate as presented in **Eq. (2.15)**. According to the mixing ratio of outdoor air, the temperature and humidity ratio of the return air are determined as follow in **Eq. (2.16)** and **Eq. (2.17)**:

$$\psi_{OA} \equiv \frac{\dot{m}_{OA}}{\dot{m}_{SA}} = \frac{\dot{m}_{OA}}{\dot{m}_{RA} + \dot{m}_{OA}} \quad \text{Eq. (2.15)}$$

$$T_{RA} = \psi_{OA}T_{OA} + (1 - \psi_{OA})T_{cabin} \quad \text{Eq. (2.16)}$$

$$w_{RA} = \psi_{OA}w_{OA} + (1 - \psi_{OA})w_{cabin} \quad \text{Eq. (2.17)}$$

Table 2.1 The cabin envelope and environmental conditions.

Parameter	Value	Unit
Cabin volume	2.79	[m^3]
Vehicle outer surface area	16.04	[m^2]
Specific heat capacity of the interior	1.50	[kJ kg^{-1} K^{-1}]
Mass of the interior	150	[kg]
Heat transfer coefficient of the interior	100	[W m^{-2} K^{-1}]
The surface area of the interior	6.7	[m^2]
Heat transfer coefficient of inside windows	11	[W m^{-2} K^{-1}]
Solar irradiation	0	[W m^{-2}]

2.3. Numerical model of the wet air

The thermophysical and transport properties of the wet air should be calculated according to the relative humidity. The values of thermal properties such as density (ρ_{air}), specific enthalpy (i_{air}), and specific heat capacity ($c_{p,air}$) have a difference with the dry air since the molar fraction of the water molecule. The specific heat capacity shows the higher heat capacity as increasing the relative humidity as shown in **Figure 2.2**(a). In the case of density, the bulk density of air is decreasing as high containment of water molecules as presented in **Figure 2.2**(b). Since the heat capacity of water, the specific enthalpy trends also similar to the density as illustrated in **Figure 2.3**(b). The other properties such as thermal conductivity, viscosity, thermal diffusivity, and Prandtl number were also calculated using the polynomial equations [57]. For instance, the specific heat capacity and the density of the wet air are obtained by **Eq. (2.18)** and **Eq. (2.19)** using the coefficient which is noted in **Table 2.2** and **Table 2.3**.

$$c_{p,wetair} = SC_0 + SC_1 t + SC_2 t^2 + SC_3 t^3 + SC_4 t^4 + SC_5 t^5 \qquad \text{Eq. (2.18)}$$

$$\rho_{wetair} = SD_0 + SD_1 t + SD_2 t^2 + SD_3 t^3 \qquad \text{Eq. (2.19)}$$

Where, t is Celsius temperature [°C].

Table 2.2 Specific heat capacity coefficient of moist air [57].

Coefficient	SC_0	$SC_1 \times 10^{-3}$	$SC_2 \times 10^{-4}$	$SC_3 \times 10^{-6}$	$SC_4 \times 10^{-8}$	$SC_5 \times 10^{-10}$
ϕ = 0%	1.00505801	0.03965404	0.00415208	−0.0001947	−0.0001822	0.00007234
ϕ = 10%	1.00542257	0.04752800	0.02043170	0.00316020	0.00694067	0.03848719
ϕ = 20%	1.00575548	0.07070698	0.02202137	0.05916757	−0.0658079	0.12269542
ϕ = 30%	1.00604457	0.11486602	0.00361064	0.18601282	−0.2443521	0.26586309
ϕ = 40%	1.00627389	0.18754592	−0.0417626	0.40720632	−0.5617547	0.48455021
ϕ = 50%	1.00642118	0.29876509	−0.1232265	0.75329857	−1.0606209	0.79988700
ϕ = 60%	1.00645895	0.46123693	−0.2523949	1.26309166	−1.7948305	1.23841889
ϕ = 70%	1.00635015	0.69181828	−0.4445412	1.98725333	−2.8342130	1.83424607
ϕ = 80%	1.00604550	1.01262440	−0.7195895	2.99154978	−4.2689148	2.63109504
ϕ = 90%	1.00548110	1.45262900	−1.1036553	4.36191084	−6.2161311	3.68543936
ϕ = 100%	1.00457142	2.05063275	−1.6315370	6.21230030	−8.8304788	5.07130703

Table 2.3 Moist air density coefficient [57].

Coefficient	$\mathbf{SD_0}$	$\mathbf{SD_1 \times 10^{-3}}$	$\mathbf{SD_2 \times 10^{-5}}$	$\mathbf{SD_3 \times 10^{-7}}$
ϕ = 0%	1.293076926	−4.668788752	1.616496527	−0.270258690
ϕ = 10%	1.293108555	−4.755745337	1.840833144	−0.768566623
ϕ = 20%	1.293140234	−4.842714106	2.065234104	−1.266930718
ϕ = 30%	1.293172031	−4.929691585	2.289622204	−1.765272412
ϕ = 40%	1.293203823	−5.016669259	2.514022965	−2.263626682
ϕ = 50%	1.293235188	−5.103624740	2.738382420	−2.761958201
ϕ = 60%	1.293266904	−5.190564282	2.962671829	−3.260235828
ϕ = 70%	1.293298927	−5.277566167	3.187131352	−3.758628812
ϕ = 80%	1.293330395	−5.364522222	3.411479567	−4.256947646
ϕ = 90%	1.293362125	−5.451485999	3.635853785	−4.755289659
ϕ = 100%	1.293393662	−5.538444326	3.860201577	−5.253606500

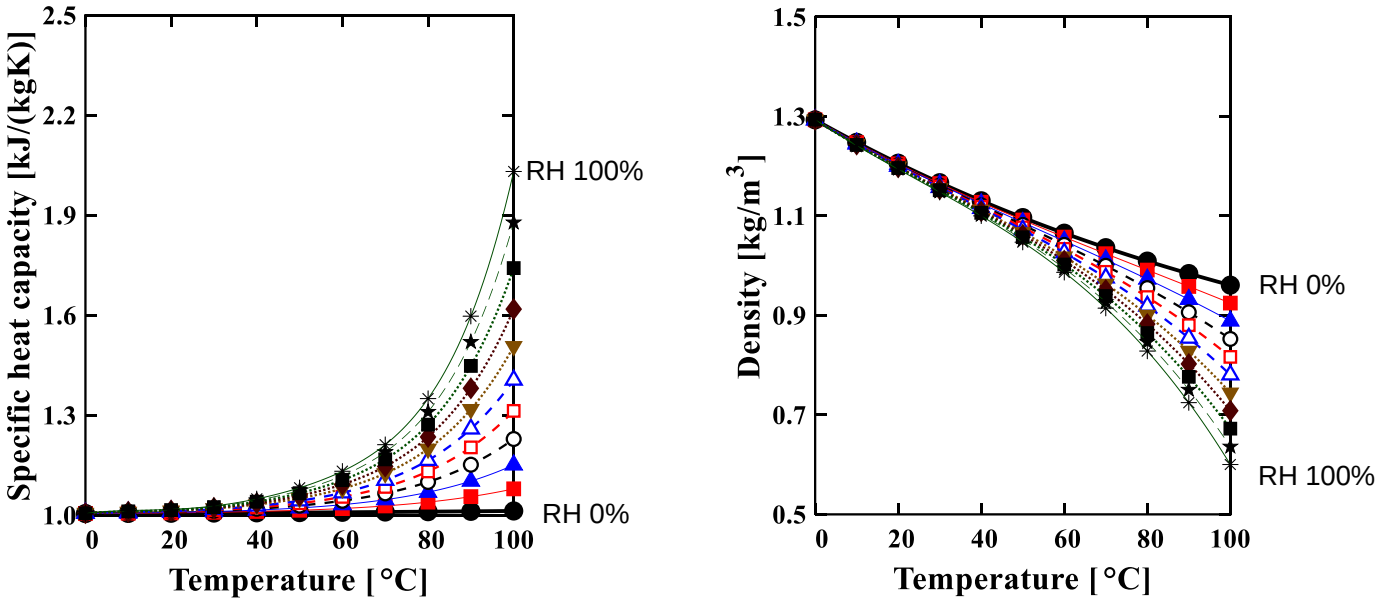

(a) (b)

Figure 2.2 Thermophysical of the wet air according to the relative humidity; (a) specific heat capacity, (b) density.

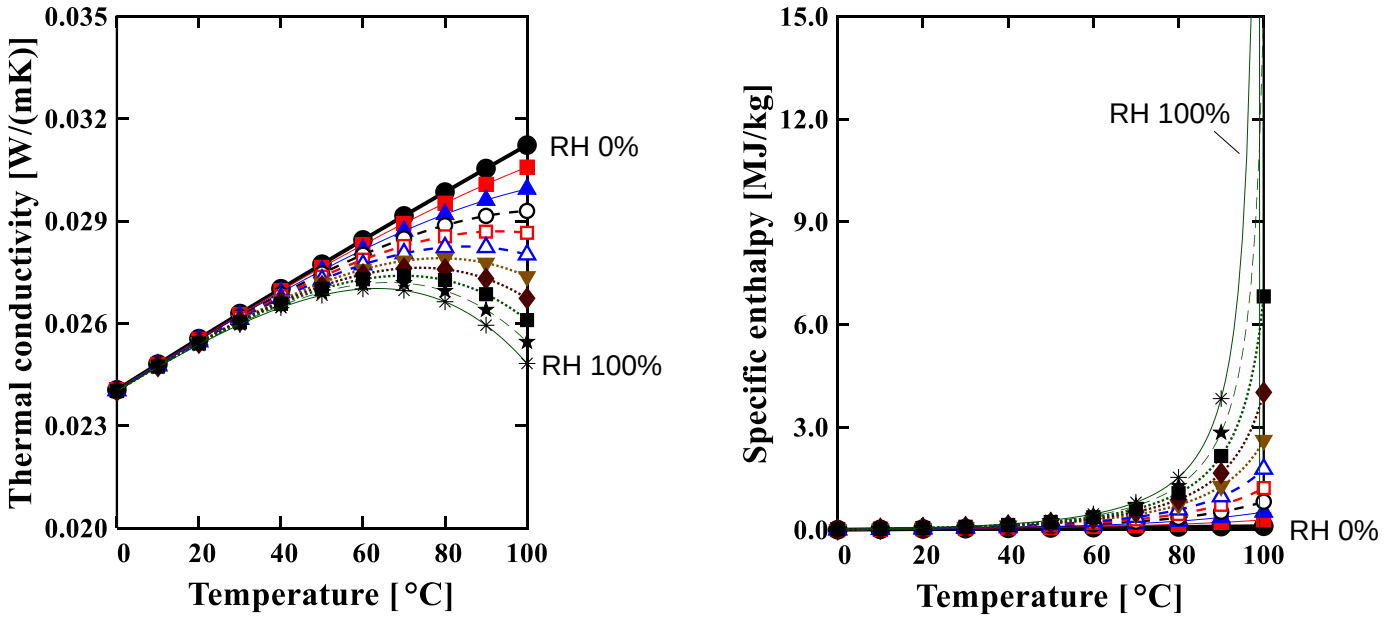

(a) (b)

Figure 2.3 Thermophysical of the wet air according to the relative humidity; (a) thermal conductivity, (b) specific enthalpy.

The dew point is obtained using the **Eq. (2.20)**, where the molar mass of water vapor (M_v) and dry air (M_{DA}) are 0.0180153 and 0.028964 [kg/mol], respectively.

$$T_{DP} = \frac{M_v}{M_{DA}}\left(\frac{\phi P_{v,sat}}{P_{atm} - \phi P_{v,sat}}\right) \qquad \text{Eq. (2.20)}$$

The saturation vapor pressure ($P_{v,sat}$) [Pa] is calculated as following **Eq. (2.21)** [58] which is referred according to a handbook of the American Society of Heating, Refrigerating and Air-Conditioning Engineers (ASHRAE) [59].

$$P_{v,sat} = \exp\left[\frac{\mathrm{C}_8}{T} + \mathrm{C}_9 + \mathrm{C}_{10}T + \mathrm{C}_{11}T^2 + \mathrm{C}_{12}T^3 + \mathrm{C}_{13}\ln(T)\right] \qquad \text{Eq. (2.21)}$$

where, the constants are $\mathrm{C}_8 = -5.8002206 \cdot 10^3$, $\mathrm{C}_9 = 1.3914993$, $\mathrm{C}_{10} = -4.8640239 \cdot 10^{-2}$, $\mathrm{C}_{11} = 4.1764768 \cdot 10^{-5}$, $\mathrm{C}_{12} = -1.4452093 \cdot 10^{-8}$, $\mathrm{C}_{13} = 6.5459673$.

2.4. Validation of the cabin model

To validation the developed cabin model, the calculated load is compared with the other research group's result [41]. To comparison, the operation conditions of the cabin model are predefined as shown in **Table 2.4** to match the reference's condition.

The root mean squared error ($RMSE$) and the root mean squared relative error ($RMSRE$) of the cabin air temperature and relative humidity are calculated

to compare with reference data and the simulation results of the developed model as following the **Eq. (2.22)** and **Eq. (2.23)**, respectively.

$$RMSE_x = \sqrt{\frac{1}{n}\sum_{i=1}^{n}\left(x_{ref} - x_{sim}\right)^2}\Bigg|_{x=T,\phi} \qquad \text{Eq. (2.22)}$$

$$RMSRE_x = \sqrt{\frac{1}{n}\sum_{i=1}^{n}\left(\frac{x_{ref} - x_{sim}}{x_{ref}}\right)^2} \times 100\%\Bigg|_{x=T,\phi} \qquad \text{Eq. (2.23)}$$

As a result, the root mean squared error ($RMSE_T$) and the root mean squared relative error ($RMSRE_T$) of the cabin air temperature are 1.51 and 5.27%. In case of the relative humidity, the $RMSE_{RH}$ and $RMSRE_{RH}$ are calculated as 2.45 and 9.91%. Therefore, the developed model shows good agreement with the reference data.

Table 2.4 Operation conditions of the cabin model to the validation.

Parameter	Value	Unit
Initial temperature of the cabin	60.0	[°C]
Initial relative humidity of the cabin	60.0	[%]
Ambient temperature	43.3	[°C]
Ambient relative humidity	65.0	[%]
Solar radiation	950	[W/m^2]
Infiltration rate	0.02832	[m^3/s]
Number of passengers	1	[–]

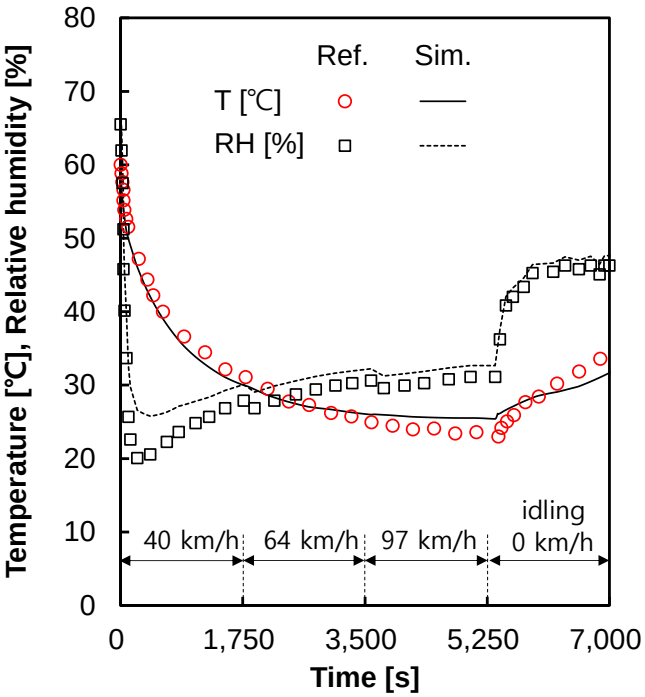

Figure 2.4 Comparison results of the cabin temperature on the various speed of the vehicle.

2.5. Sensitivity analysis of the cabin model

Owing to determine the thermal load of the cabin, the parameters are predefined. The initial temperature of the cabin air and interior was set as 5°C. The velocity of the vehicle is 50 km/h constantly during 13,700 s. A heating device works when the cabin air temperature is below the target cabin air temperature (24°C). The cabin air is recirculated without mixing with outdoor air, i.e. ψ_{OA} is 0. The ambient temperature is 7°C and the absolute humidity is 0.004 kg/kg. The mass flow rate of the supply air is 0.135 kg/s. The solar radiation is 0 as considering the nighttime. The infiltration is negligible.

When people feel cold, the thermal sensation value is negative. In contrast, the positive value means the warm and hot conditions for a human. The thermal sensation value is a function of the dry bulb and wet bulb temperature as given **Eq. (2.24)** [60]. It is evaluated for a young adult with sedentary activity and wearing clothing with a thermal resistance of 0.5 clo. The clo means that the clothing and thermal insulation, 1 clo correspond to the 0.155 $[(\mathrm{m}^2 \cdot \mathrm{K})/\mathrm{W}]$.

$$Y = 0.252 \cdot T_{air} + 0.240 \cdot P_v - 6.859 \qquad \text{Eq. (2.24)}$$

where, P_v is vapor pressure which is obtained the dew point temperature using **Eq. (2.21)**, which differs from the vapor saturated pressure ($P_{v,sat}$).

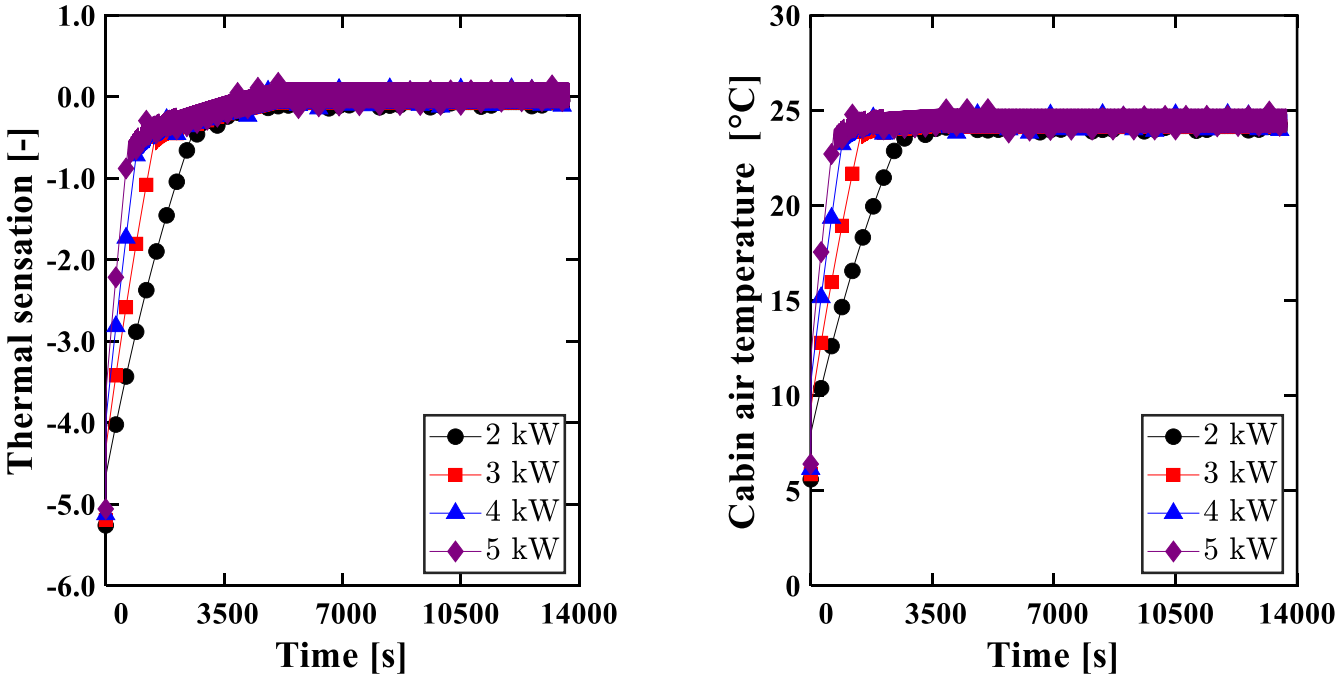

(a) (b)

Figure 2.5 The approach time subject to the heat capacity of a heating device: (a) thermal sensation, and (b) cabin air temperature.

When the thermal sensation reaches the 0 value, the people feel thermal neutral, neither hot nor cold. As shown in **Figure 2.5(a)**, the time for the thermal sensation to reach zero is faster as the capacity of the heating device increase. But total heating loads, which are operating during the 13,700 s, are not significantly different regardless of the heating capacity of the device.

2.5.1. Ambient temperature and the number of passengers

In order to investigate the effect of the ambient temperature and the number of persons on the cabin thermal loads, the calculation is conducted. The capacity of the heating device is 3 kW in this section. Other predefined parameters are described in the above section.

As a result, the heating loads are obtained at various ambient temperatures and the number of passengers as shown in **Figure 2.6**. When the air temperature is cooler, the heating load of the cabin is increased because the metabolic heat generation is large according to **Eq. (2.6)**.

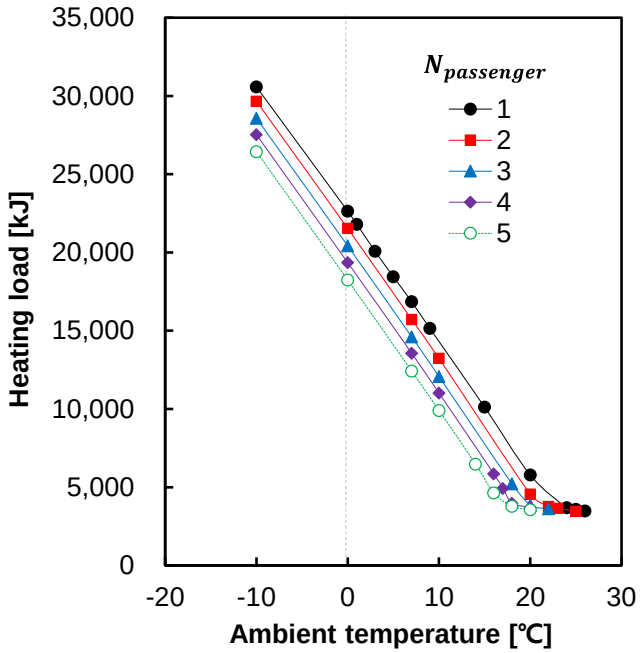

Figure 2.6 Heating load according to the ambient temperature and number of passengers.

2.5.2. Vehicle velocity profile

Owing to determine the effect of the vehicle velocity on the heating load, the various driving profile is considered. The driving velocity profiles are summarized in **Figure 2.7**. The new European driving cycle (NEDC) is designed to estimate the fuel efficiency and emission of a light-duty vehicle according to the EEC Directive 90/C81/01. It is combined with the 4 repeated urban driving cycles (UDC, it is also known as ECE-15) and the single extra-urban driving cycle (EUDC). But it is being criticized because the driving speed patterns are stylized with slow acceleration and constant speed. The ARTEMIS European driving cycle was developed based on a statistical analysis of a large database of European real-world driving patterns. The name of the driving profile is the abbreviation of the assessment and reliability of transport emission models and inventory systems. But it's the average velocity of the vehicle is too slow as compared to others. The worldwide harmonized light vehicles test cycle (WLTC) is developed to replace the NEDC cycle. It is divided into four parts; low, medium, high, and extra high-speed period. The WLTP cycle is a more complex profile, but it is much closer to real-world driving [61]. The urban dynamometer driving schedule (UDDS) is developed by US Environmental Protection Agency (EPA) to assess the fuel economy. It is used to estimate the driving mileage of an electric vehicle.

According to the velocity profile, the heating load is obtained as shown in **Figure 2.8**. The predefined parameters are the same as with the previous section such as the specification of the cabin and initial conditions.

As a result, the heating load is increased when the average velocity is faster. Because the convective heat transfer coefficient of the vehicle is enhanced when the vehicle driving fast as following **Eq. (2.14)**. Hence, the convective heat loss of the vehicle is enlarged. As a reference to the heating load at the stopped case, the heating load of the high-speed case (100 km/h) is about 29% large. However, the sensitivity of the driving profile seems not severe on the total heating load.

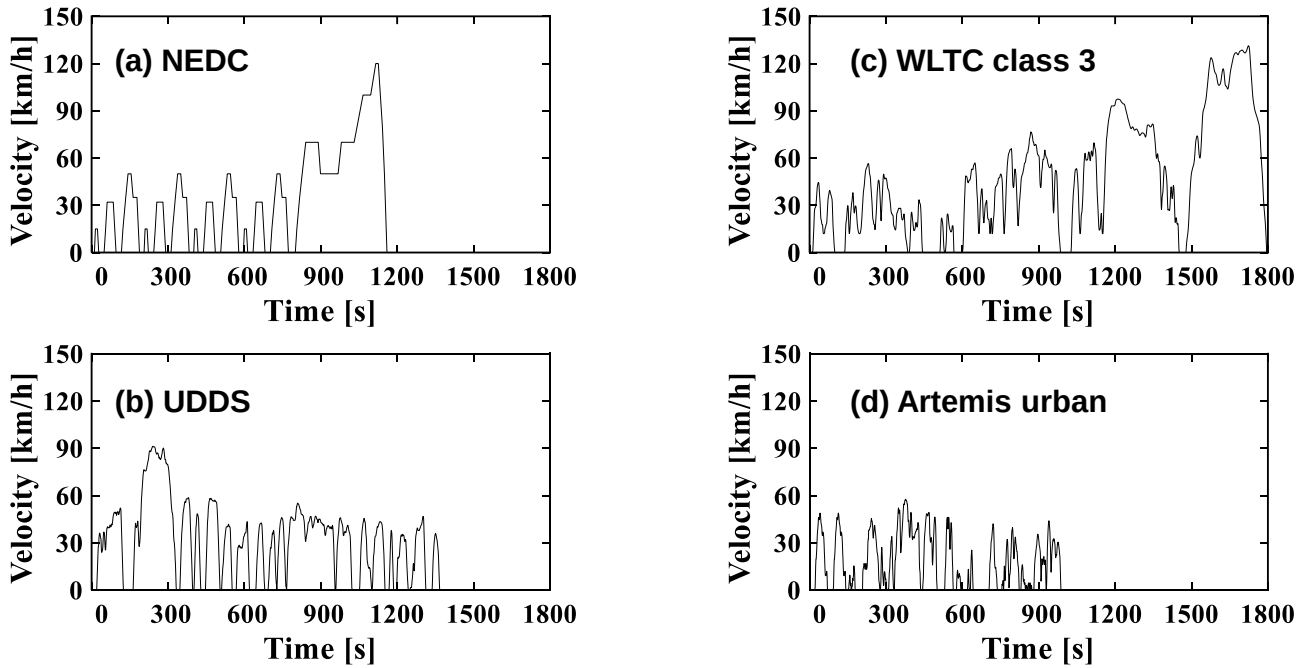

Figure 2.7 Vehicle driving profiles: (a) New European driving cycle (NEDC), (b) US EPA urban dynamometer driving schedule (UDDS), (c) The worldwide harmonized light vehicles test cycle (WLTC) class 3, (d) the European assessment and reliability of transport emission models and inventory systems (Artemis) urban cycle.

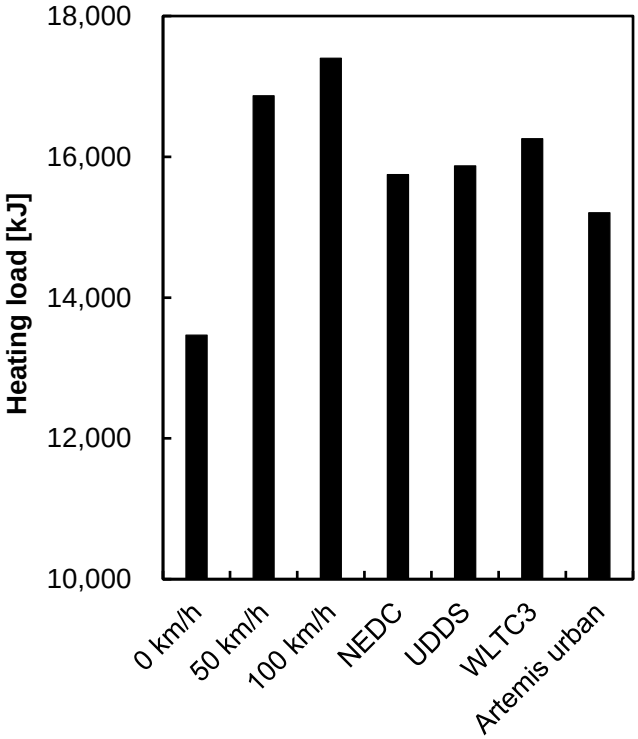

Figure 2.8 Heating load subject to the vehicle driving cycle.

2.6. Summary

In this Chapter, the thermal cabin model was developed to estimate the cabin thermal load using energy and mass balance equations. Because the evaluation of the cabin thermal load is crucial to obtain the energy consumption of the automobile heat pump system.

To achieve the purpose, four nonlinear ordinary differential equations were calculated to determine the heating load of the passenger compartment; two energy balance equations for cabin air and interior mass, and two mass balance equations for cabin dry air and moisture. The thermodynamic properties of moisture air are also evaluated. The developed cabin model was validated by comparing it with the experimental result of the other research group.

The cabin thermal load depends on convectional heat, solar radiation, and metabolic heat. Hence, the sensitivity analysis of the developed cabin model was conducted subject to the number of passengers, ambient air temperature, and velocity of the vehicle.

Chapter 3. Design and performance analysis of the desiccant coated heat exchanger

3.1. Introduction of the DCHE

In this study, the desiccant coated heat exchanger (DCHE) is introduced in an electric vehicle to handle the humidity by heat and mass transfer simultaneously. As the name suggests, the DCHE is a heat exchanger that has absorbents attached to the fins. The desiccant which is coated in the fin is able to capture moisture by adsorption. Adsorption means that the adhesion of molecules to a substrate surface. It is occurred by intermolecular forces between an adsorbent and an adsorbate on the surface layer of the adsorbent as shown in **Figure 3.1(a)**. During an adsorption process, the molecules (adsorbate) are enriching by sticking and accommodation on the substrate (adsorbent) of the surface. Reversely, the process that molecules removing from the substrate is called desorption. Usually, the adsorption process is exothermic and the increased temperature of the adsorbent decreased the adsorption performance. To enhance the adsorption characteristic, the inter-cooling during adsorption is considered by heat exchanging through the metal fin.

The a**d**sorption mechanism differs from a**b**sorption. While absorption is that the molecules penetrate into the structure of the substrate, adsorption is the

phenomenon that is occurred on the adsorbent surface. The detail of the adsorption principle is discussed in the next section.

3.1.1. Principle of the adsorption

As mentioned above, the adsorption phenomenon occurs on the interfacial layers. When hard to distinguish between adsorption and absorption because the interesting molecules are reacted to both the surface layer and body of a substrate, the phenomenon is called just 'sorption'.

The adsorption is divided into physisorption and chemisorption. The chemisorption is classified when adsorbate strongly binds with adsorbent by involving a chemical reaction and creation new types of electronic bonds. In contrast with the chemisorption, the physisorption is a weak bond between the adsorbate and adsorbent by Van der Waals forces. In this study, physisorption is mainly discussed because it commonly relative to the dehumidification process rather than chemisorption.

The driving force of the physisorption is known as van der Waals forces [62]. Van der Waals forces are a distance-dependent interaction between electrically neutral molecules. It is the sum of electrostatic forces that are able to mainly classified into three kinds of interaction; dipole-dipole interaction

(Keesom force), dipole-induced dipole interaction (Debye force), and dispersion forces that temporary fluctuating dipoles of non-polar molecules (London force). While the attraction force by the van der Waals force shows $1/r^6$ dependence, the repulsive force arises according to $1/r^{12}$ dependence due to the Born repulsion that is electrostatic force between molecules. And it is postulated that the molecules are not able to overlap because of the Pauli exclusion principle that is electron clouds of molecules cannot occupy the same quantum state. Thus, the resulting intermolecular interaction potential, named Lennard-Jones potential, is illustrated in **Figure 3.1(b)**.

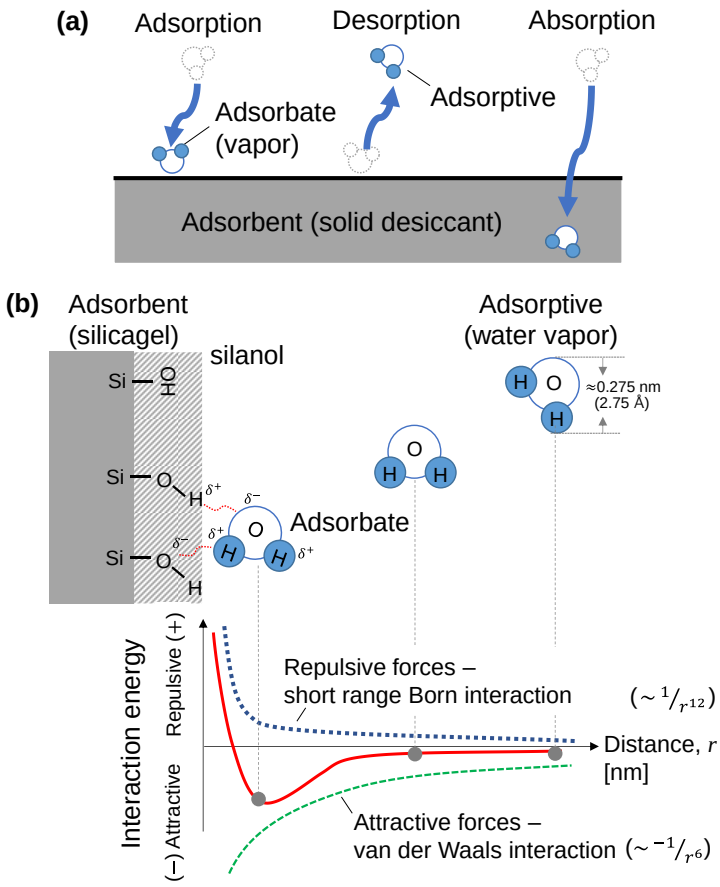

Figure 3.1 Conceptual diagrams; (a) the adsorption and desorption process (b) the interface with the adsorbent (silica-gel) and adsorbate (water vapor).

3.1.2. Selection of the solid desiccant and the binder

To select the proper adsorbent for fabricating the DCHE, the desiccant material should have a great affinity for water vapor and it can be generated at a low temperature, i.e., below 100°C. Also, the desiccant should be chemically stable, non-toxic, non-corrosive, non-hydrate, and unexpansive cost. The zeolite type materials including molecular sieves, FAPO (Ferro-aluminophosphate), and metal-organic frames (MOFs) have reported that the higher moisture adsorption capability, but it required the higher regenerated temperature due to it strongly bonded with water molecules or it may operate under a narrow range condition [29, 30, 63, 64]. While the silica-gel shows that the proportional relationship between the amount of water uptake and the relative humidity. Hence, silica-gel is not required for the significantly sensitive operation condition [65]. And the cost of the silica-gel is the most reasonable and affordable. For these reasons, silica-gel is chosen as an adsorbent in this study.

In the case of the silica-gel and water vapor interaction, the physisorption is able to occur on the interface with the silica-gel and water vapor because the silica-gel has silanol (Si-OH) groups which are attracted the dipole water molecules *via* the formation of hydrogen bonding as shown in **Figure 3.1**(b). Ideally, one silanol group is able to make hydrogen bonding with three water

molecules since the hydrogen atom of the silanol should be attracted oxygen atom of water and the lone pairs of electrons of silanol oxygen can be bonded with two hydrogen atoms of water [66]. Therefore, the number of silanol groups on the surface layer should be enlarged to enhance the sorption capacity. And the pore volume and the surface area would be a key role in improving water uptake performance [67, 68].

Because adsorption is a surface-based process, the surface area, size of pores, and pore size distribution affect the adsorption capacity. For instance, a large surface area is required to enhance the adsorption capacity because the sites of interaction between adsorbate and adsorbent should be enlarged. And the pore type also affects the performance of adsorption. The pores are classified subject to size as shown in **Figure 3.2**(a). According to the International Union of Pure and Applied Chemistry (IUPAC) recommendation [69], the pores which are its width is not exceeding about 2 nm are called micro-pore. The meso-pore means that the width of the pore is between 2 nm and 50 nm. When the pore width is exceeded 50 nm, it is called macro-pore. The micro-pores should be filled faster than meso- or macro-pore because their own volume is much smaller and the required amount of adsorbate is less than meso- or macro-pore. Thus, when the primary physisorption process, the micro-pore filling may occur as illustrated in **Figure 3.2(b)**. As the pore size approaches

the adsorbate molecular size, the van der Waals force will be amplified because the adsorbate is able to easily multiple interactions with the pore wall of the adsorbent. After then, the meso- and macro-pores might be filled by increasing the partial vapor pressure. The desorption curve might be not coinciding with the adsorption curve due to the capillary condensation or capillary evaporation. In the capillary tube, the surface tension of liquid water makes meniscus. The surface tension allows the vapor condensation or resists the vapor evaporation at the saturation vapor pressure. The difference between the saturation vapor pressure and the equilibrium vapor pressure is explained by the Kelvin equation which describes the vapor pressure at a convex or concave curved liquid surface. Using the equation, the pore size distribution of a meso-porous material is possible to determine. The capillary condensation/evaporation leads to the adsorption/desorption hysteresis correspond to the relative pressure. The characteristic of the adsorption and desorption is changed depends on the temperature.

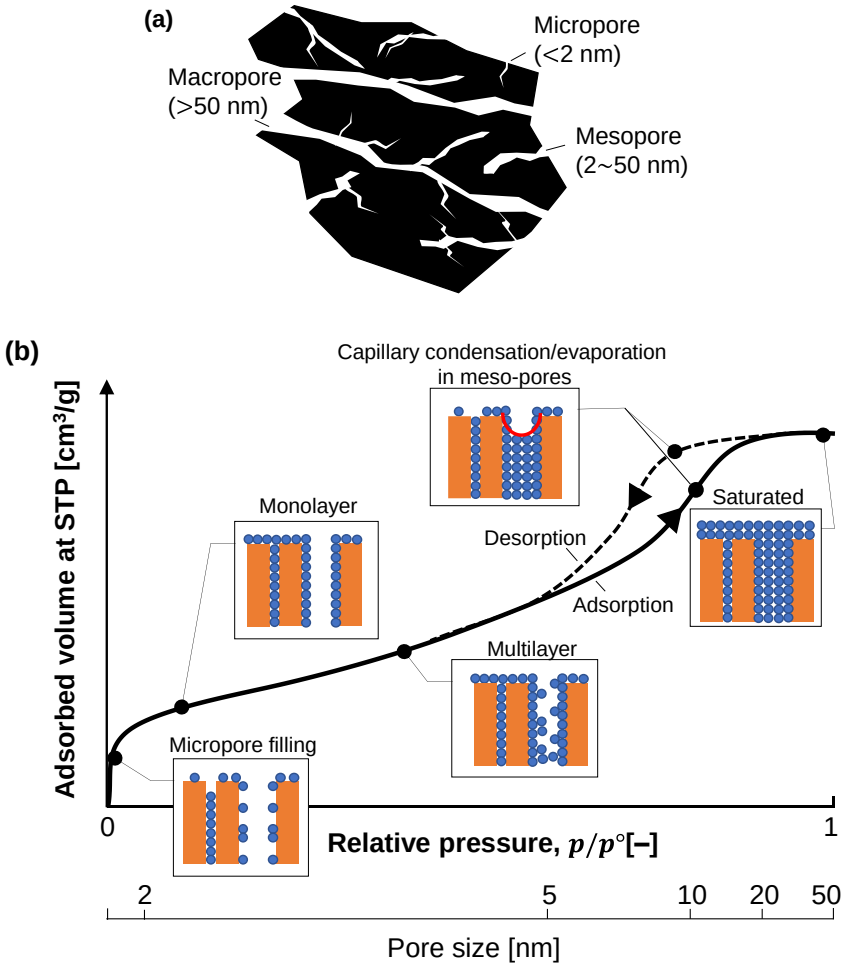

Figure 3.2 Conceptual diagrams; (a) classify pores subject to their size, (b) adsorption isotherm curve.

To attach the adsorbent to the metal fin of a heat exchanger, the binder is necessary. The binder material should have not only a good adhesive ability, but also high thermal conductivity, proper water adsorption capacity, and durability. According to the literature study [70-72], the hydroxyethyl cellulose (HEC) shows that the most suitable pair with the silica-gel on metal fins. The HEC is a water-soluble polymer that is widely used for making gelation, thickening, and stabilization.

In order to understand the adsorption performance subject to the composition of the silica-gel and the binder, it should be preceded by obtaining not only physical properties such as the surface area but also equilibrium isotherm adsorption/desorption curve. Therefore, the samples were prepared to investigate the optimum binder ratio according to the silica-gel and binder weight percentage as shown in **Figure 3.3**.

Figure 3.3 Adsorbent samples subject to the weight content of the binder.

3.2. Physical properties of the adsorbent

3.2.1. The surface area of the adsorbent

The surface area is one of the main parameters to affect the performance adsorption capacity of the adsorbent. To measure the surface area of the adsorbate, the Brünauer-Emmett-Teller (BET) method has been widely used [69, 73-75]. The BET equation is developed from the Langmuir isotherm model [76] that the adsorbate has no interaction between each molecule and deposit as mono molecule surface coverage, i.e., monolayer. The Langmuir model well explains chemisorption and monolayer physisorption. However, most gas molecules can be deposited on the surface as multilayer. Thus, they modified the isotherm model as considering multilayer adsorption with the different heat of adsorption between each layer as following **Eq. (3.1)**.

$$\frac{p}{n^a(p^\circ - p)} = \frac{1}{n_{\mathrm{m}}^a \cdot C_{\mathrm{BET}}} + \frac{(C_{\mathrm{BET}} - 1)}{n_{\mathrm{m}}^a \cdot C_{\mathrm{BET}}}\frac{p}{p^\circ} \qquad \text{Eq. (3.1)}$$

Where, C_{BET} is the BET constant which is related exponentially to the heat of adsorption in the first adsorbed layer, n^a is the adsorbed gas quantity at the equilibrium relative pressure (p/p°) in a specific volume unit, and n_{m}^a is the monolayer capacity which is the adsorbate volume to cover the surface completely as a monolayer. The p° denotes the saturation pressure of the pure

adsorptive at the temperature. The specific surface area of the BET method ($a_{s,\mathrm{BET}}$ [m^2/g]) is able to calculated using specific monolayer capacity (n_{m}^{a} [m^3/g]), the Avogadro number ($\mathrm{N_{av}}$ [1/mol]), the cross-sectional area of adsorptive molecule (a_m [m^2]), and the molar volume of the adsorbate ($\tilde{V}^a$ [m^3/mol]) at the standard temperature and pressure (STP) as following Eq. (3.2). The cross-sectional area of N_2 has used the customary value at 77.35 K, i.e., 0.162 nm^2.

$$a_{s,BET} = \mathrm{N_{av}} \cdot a_m \cdot n_m^a / \tilde{V}^a \qquad \text{Eq. (3.2)}$$

Thus, the BET constant (C_{BET}) and the monolayer capacity (n_{m}^{a}) should be obtained to determine the surface area. These values are able to calculate by a linear relation between $p/[n^a(p^\circ - p)]$ and relative pressure (i.e. the BET plot). Using gradient (α_{BET}) and intercept (β_{BET}) of the BET plot, the C_{BET} and n_{m}^{a} should be calculated Eq. (3.3) and Eq. (3.4).

$$C_{\mathrm{BET}} = 1 + \frac{\alpha_{\mathrm{BET}}}{\beta_{\mathrm{BET}}} \qquad \text{Eq. (3.3)}$$

$$n_m^a = \frac{1}{\alpha_{\mathrm{BET}} + \beta_{\mathrm{BET}}} \qquad \text{Eq. (3.4)}$$

Before the measurements, the samples were degassed and evacuated under over 120°C and high vacuum conditions for 12 hours. The manometric adsorption experiment is conducted using the Tristar® 3020 with the N_2 at 77 K. The results of the N_2 sorption isotherms test, the adsorption curves of the

samples correspond to the type IVa isotherm of the IUPAC classification [75]. At the relative pressure in the range of 0.05 to 0.30, the surface areas of samples were obtained using the BET plot as illustrated in **Figure 3.5**. As increasing the amount of HEC binder, the surface area and the monolayer capacity are reduced as shown in **Table 3.1**.

The BET constant is available to expressed like **Eq. (3.5)**, where E_1 is heat of adsorption for the first layer, E_L is heat of liquification or vaporization for the second and higher layer. The C_{BET} indicates the magnitude of the adsorbent-adsorbate interactional energy. And it is associated with the stage that completed coverage of the monolayer and beginning multilayer adsorption [77, 78]. As a result of the BET analysis, more energy might be needed for the desorption process as increasing HEC weight percent, as shown in **Table 3.1**.

$$C_{\mathrm{BET}} = \exp\left(\frac{E_1 - E_L}{R^* T}\right) \qquad \text{Eq. (3.5)}$$

Where, R^* is the gas constant. From the result, the high content of the binder should be avoided because it may lead to reduce the adsorption capacity by decreasing the surface area of the adsorbent.

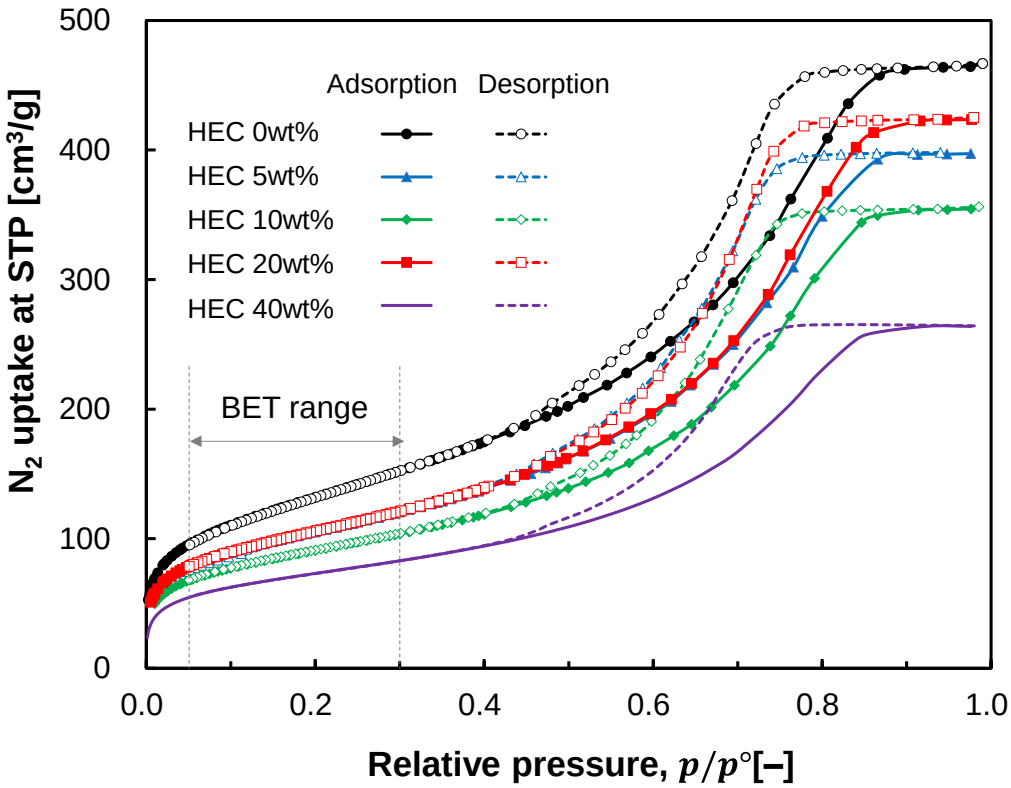

Figure 3.4 Nitrogen sorption isotherms of samples with various weight percentages at standard temperature and pressure conditions.

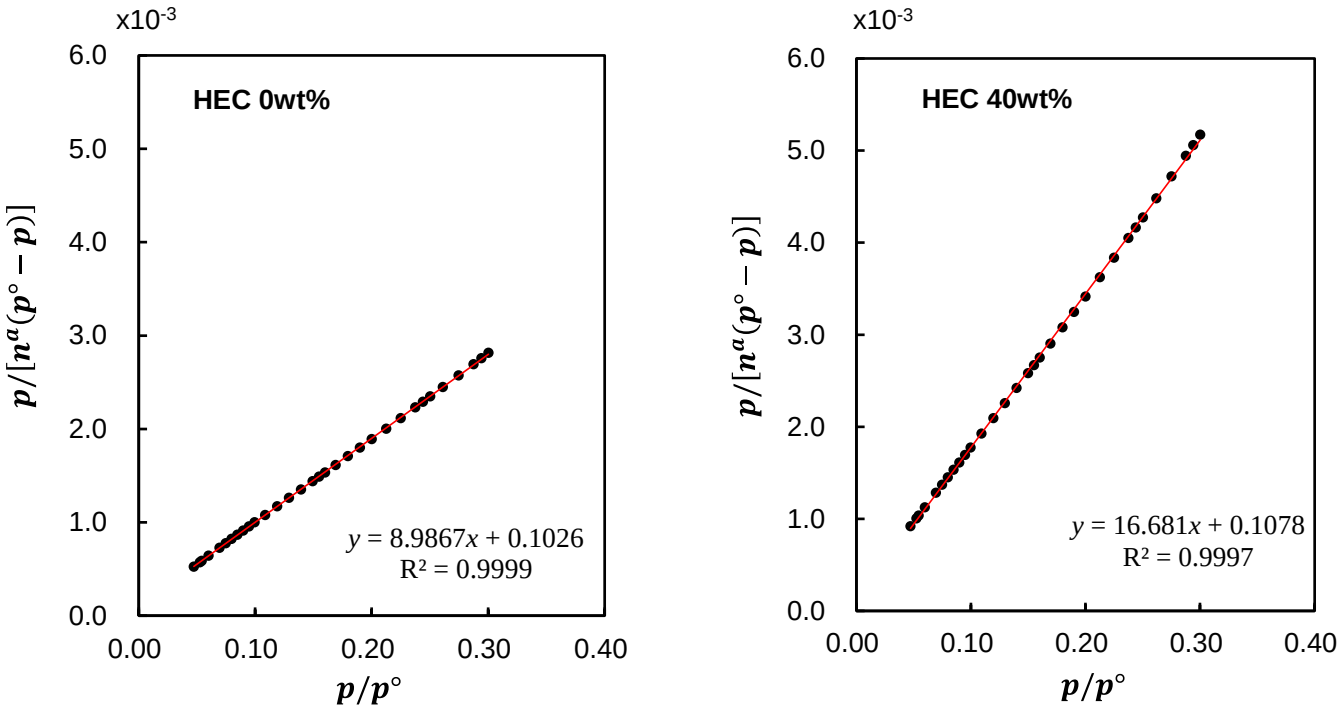

(a) (b)

Figure 3.5 The BET plot (a) in the case of HEC 0wt% (pure silica-gel) (b) in the case of HEC 40wt%.

Table 3.1 The BET surface and monolayer capacity of samples.

Binder content	BET surface, $a_{s,BET}$ [m²/g]	monolayer capacity, n_m^a [cm²/g]	BET constant, C_{BET} [–]
HEC 0wt% (pure silica-gel)	478.94	110.02	88.65
HEC 5wt%	378.51	86.95	125.37
HEC 10wt%	376.86	86.57	119.95
HEC 20wt%	324.22	74.48	130.28
HEC 40wt%	259.29	59.56	155.73

The pore size distribution is determined from experimental isotherms by applying the Barrett-Joyner-Halenda (BJH) method [79] using the modified Kelvin equation. The Kelvin equation provides a correlation between the pore diameters (r_p) and the capillary condensation/evaporation pressure ($p/p°$) for a cylindrical pore is given by **Eq. (3.6)**. The pore size distribution is calculated using data of the desorption process since the desorption branch of the hysteresis loop reflects the equilibrium phase transition than the adsorption branch [80].

$$\ln\frac{p}{p°} = \frac{-2\gamma\tilde{V}_L}{r_p R^* T} \qquad \text{Eq. (3.6)}$$

As a result, the pore size distribution is obtained as following **Table 3.2** and **Figure 3.6**. Regardless of the binder content ratio, the pore size of the adsorbents is around 5 nm. But the pore volumes are reduced as increasing the binder content ratio. It might be corresponding the adsorption performance. In **Section 3.2.3.**, the adsorption performance of the adsorbent is discussed.

Table 3.2 The calculated pore volumes and pore sizes of samples.

Binder content	Pore volume [m^3/g]			Pore size [nm]	
	BJH Adsorp.	**BJH Desorp.**	**BET**	**BJH Adsorp.**	**BJH Desorp.**
HEC 0wt% (pure silica-gel)	0.652	0.712	6.03	5.48	4.96
HEC 5wt%	0.700	0.662	7.81	6.77	5.42
HEC 20wt%	0.592	0.555	7.65	6.71	5.32
HEC 40wt%	0.380	0.412	6.59	6.09	5.13

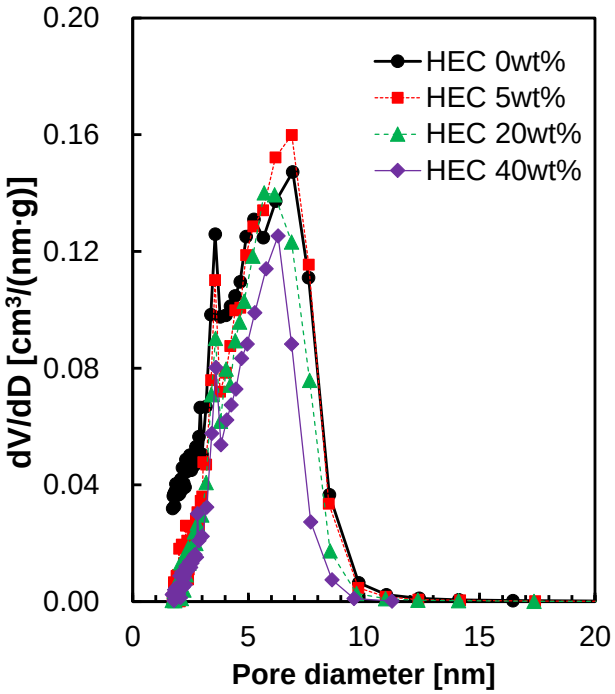

Figure 3.6 Pore size distribution with various HEC weight percentages by the BJH method under the desorption process.

3.2.2. The image analysis using the scanning electron microscope

In order to the observation of the adsorbent surface, the scanning electron microscope (SEM) is used. The SEM produces images by emitting a high-energy electron beam from an electron gun to the specimen surface. As the electrons interact with the specimen, various types of response signals are generated involving the secondary electrons, backscattered electrons, and characteristic X-rays. The detectors collect these signals and pro-processing to visualize as a digital image file. However, in the case of nonconductive material, the signals are not properly produced. The silica-gel and hydroxyethyl-cellulose which is used as adsorbent have very low electric conductivity. Therefore, it needs to be coated with a thin noble metal film on the surface before scanning the surface. Hence, the specimens were platinum (Pt) coated under vacuum conditions during 120 s using the Cressington® 108 auto sputter coater. The electron gun is charged as 10 kV, then the images were obtained at 1,000 times and 30,000 times magnification using HITACHI SU-70 as shown in **Figure 3.7**. As increasing the HEC contents, more particles of small size were attached to the surface of grains. However, it was not clear to distinguish whether the small particles were HEC or silica gel fragments through the image analysis even with the high magnification image.

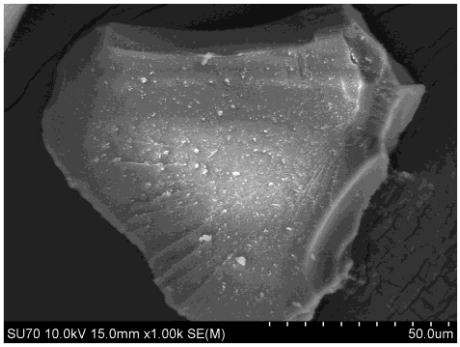

(a) HEC 0wt%, ×1,000

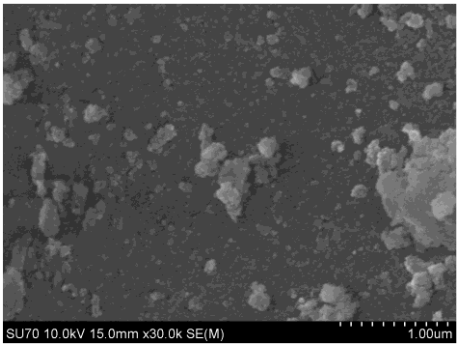

(b) HEC 0wt%, ×30,000

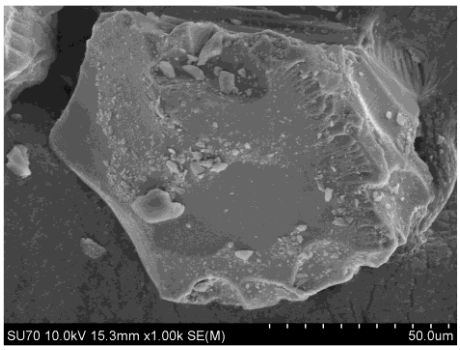

(c) HEC 5wt%, ×1,000

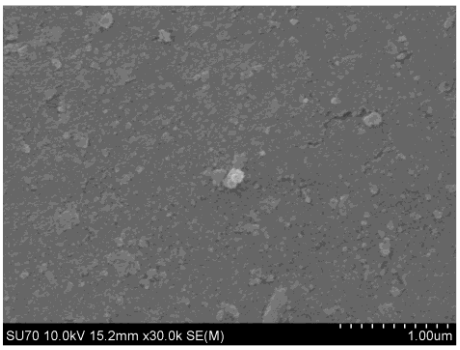

(d) HEC 5wt%, ×30,000

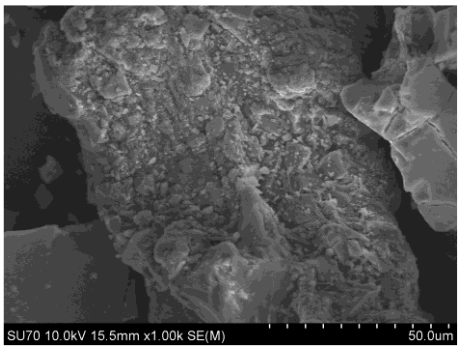

(e) HEC 40wt%, ×1,000

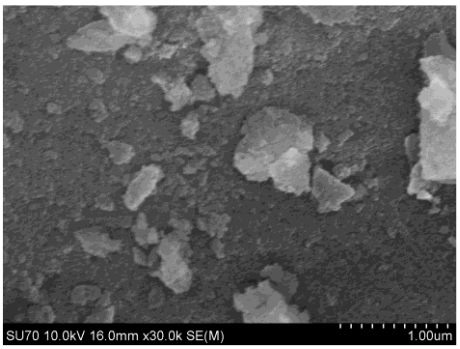

(f) HEC 40wt%, ×30,000

Figure 3.7 The scanning electron microscopic (SEM) images of the silica-gel according to the contents of HEC weight percentage at the magnifications.

Owing to distinguish the material of the particle, the energy dispersive spectroscopy (EDS) was conducted. The EDS technique identifies the elemental composition of the material in conjunction with SEM equipment. The HEC is the composition of carbon, hydrogen, and oxygen since its molecular formula is $C_{36}H_{70}O_{19}$ [81], while the pure silica-gel (SiO_2) is not contained carbon molecules. **Figure 3.8** shows the EDS results of the pure silica-gel. Since the back sheet is the carbon tape for adhesives, the EDS analysis might be distorted when including all ranges of the image. Thus, the EDS analysis range was set inside the square which is noted in the figures. Compared with the pure silica-gel case, the HEC 5wt% case —as shown in **Figure 3.9**— more contained carbon. In the case of the HEC 40wt% case, as presented in **Figure 3.10**, the composition ratio of the carbon is much higher than others. The results of the EDS spectrum process summarized in **Table 3.3**, which was normalized by summation of the weight percentage of the interested atomic, *e.g.*, carbon, oxygen, and silicon. From the results of this analysis, it is observed that the grain represents the pure silica-gel and the small particles should the binding material, i.e., HEC.

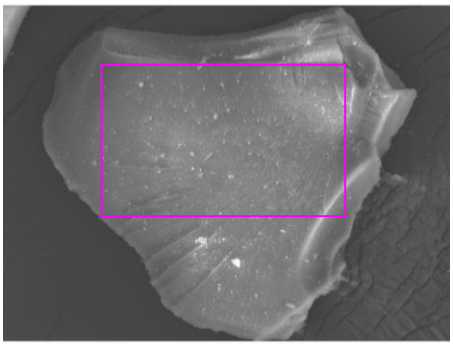

(a) Electron image

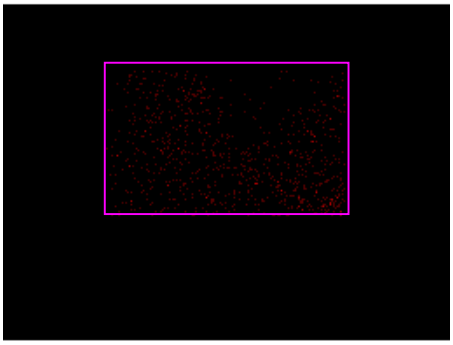

(b) Carbon, C

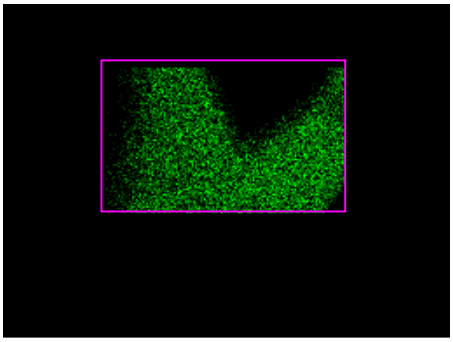

(c) Oxygen, O

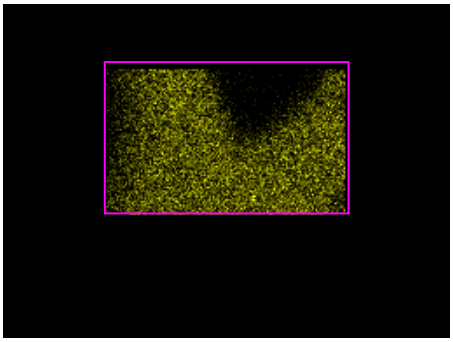

(d) Silicon, Si

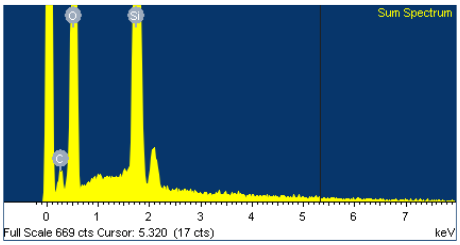

(e) Sum spectrum

Figure 3.8 The scanning electron microscopic (SEM) and energy dispersive spectroscopy (EDS) results of the pure silica-gel.

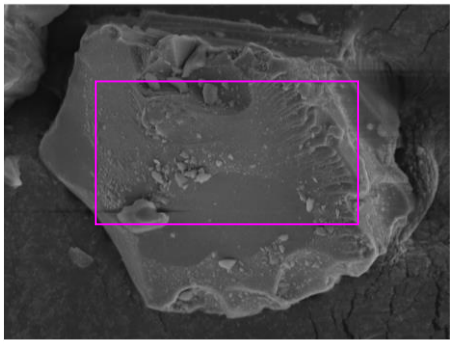

(a) Electron image

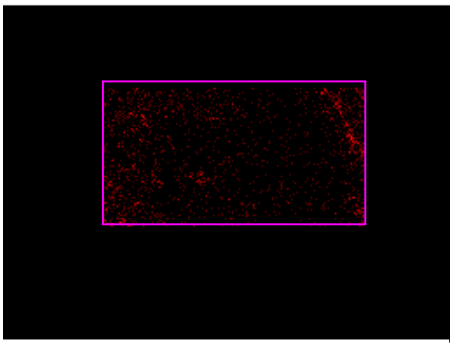

(b) Carbon, C

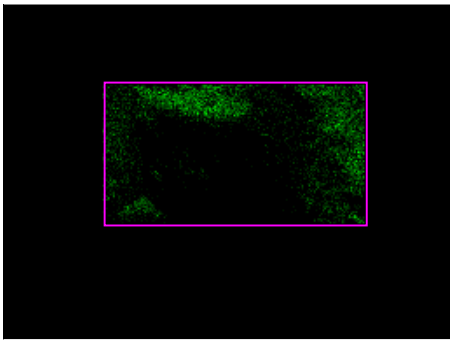

(c) Oxygen, O

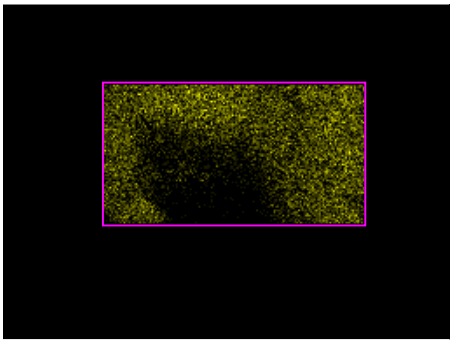

(d) Silicon, Si

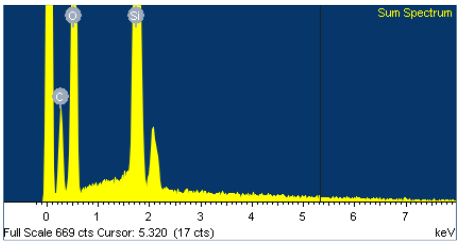

(e) Sum spectrum

Figure 3.9 The scanning electron microscopic (SEM) and energy dispersive spectroscopy (EDS) results of the 5% HEC weight percentage.

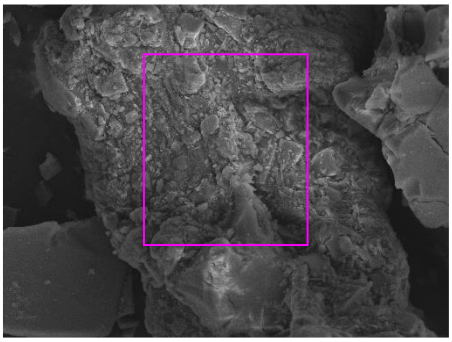

(a) Electron image

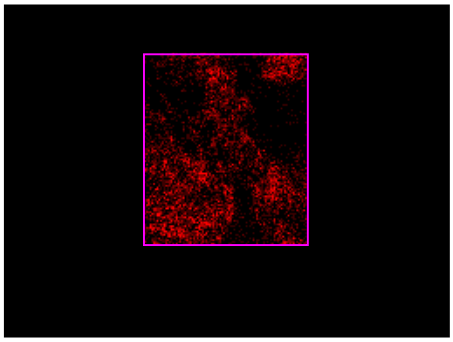

(b) Carbon, C

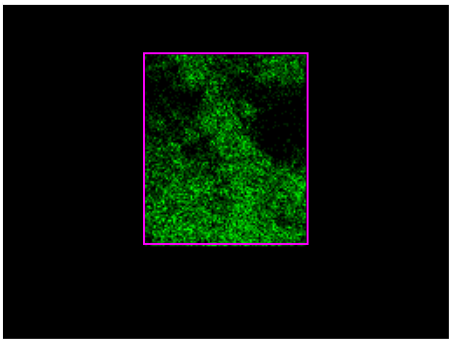

(c) Oxygen, O

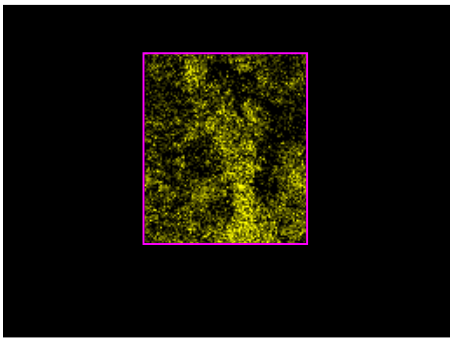

(d) Silicon, Si

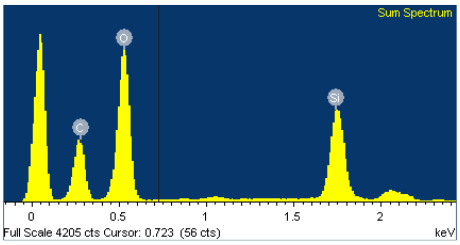

(e) Sum spectrum

Figure 3.10 The scanning electron microscopic (SEM) and energy dispersive spectroscopy (EDS) results of the 40% HEC weight percentage.

Table 3.3 The normalized weight percentage of selected elements in samples.

Binder content	Carbon, C [wt%]	Oxygen, O [wt%]	Silicon, Si [wt%]
HEC 0wt%	4.31	54.70	40.99
HEC 5wt%	15.26	43.29	41.45
HEC 40wt%	32.15	50.61	17.24

3.2.3. The vapor sorption capacity of the adsorbent

The dipole moment of water vapor differs from the nitrogen (N_2). Hence, the water vapor uptake amount might be not corresponding with the BET results since the BET result is obtained by using N_2. Owing to understand the material characterization of the vapor performance, thermogravimetric analysis (TGA) was conducted. The samples were fully saturated under high relative humidity conditions for 24 hours in a chamber. As increasing the temperature in the test cell, the weight loss of the samples was measured as shown in **Figure 3.11**. As a result, the mass change around 100°C is not significantly different from each sample regardless of the HEC content ratio.

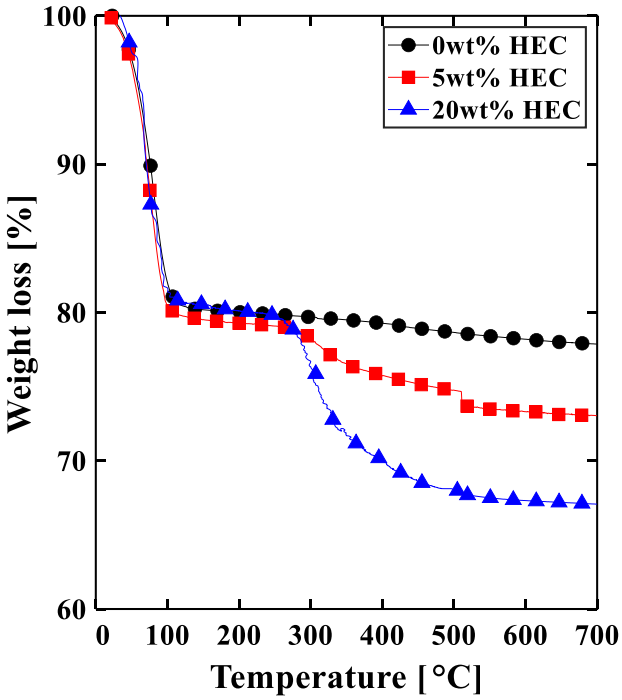

Figure 3.11 The thermogravimetric analysis curve.

Therefore, the vapor sorption analysis was conducted to obtain the accurate vapor adsorption performance using VSTAR®-2, the vapor sorption volumetric gas sorption analyzer. Generally, the adsorption analyzer is classified as a volumetric (manometric) method and gravimetric method. The gravimetric method is based on a weight change by using a sensitive microbalance and pressure gauges. The gravimetric technique is able to obtain the uptake amount directly, it has drawbacks that a pressure-dependent buoyancy correction is necessary. It is also difficult to control the exact adsorbent temperature [80]. It is a major negative effect on the determination of mesopore size distribution. Therefore, the volumetric method is recommended to obtain the adsorption performance especially in both high and cryogenic temperatures [69]. The volumetric method is admitted to a confined volume containing the adsorbent. The adsorption amount is calculated by obtaining the difference between the total amount of gas admitted to the sample cell and the amount of gas required to fill the dead space.

In the preprocessing, the adsorbent samples were degassing under 120℃ and high-vacuum conditions in the FLOVAC® degasser. To figure out the water vapor adsorption performance of adsorbent samples which is variable binder content, the analysis was conducted as shown in **Figure 3.12(a)**. As a result, the water uptake amount is reduced as increasing the binder content ratio, which is

similar patterns to the BET results. Therefore, the binder should be minimized to enhance the adsorption performance. In this study, the adsorbent sample of a 5% weight percentage of the HEC is selected to fabricate the DCHE.

The characteristic of vapor adsorption might be depended on not only physical properties but also operating conditions such as temperature and relative humidity. In order to determine the vapor sorption` capacity of the adsorbent, the equilibrium isotherm sorption analysis of the selected adsorbent is conducted under various temperatures and partial vapor pressures as presented in **Figure 3.12(b)**. At the highest temperature of the environment air temperature, the amount of the water vapor uptake is less than the low-temperature cases regardless of the relative vapor pressure.

The heat of adsorption is obtained from **Figure 3.12(b)** by using the Clausius-Clapeyron equation. The Clausius-Clapeyron method is widely applied to obtain the adsorption heat under two approximations: neglect the volume of the adsorbed phase and postulate the ideal gas behavior of the adsorbate [82, 83]. The adsorption heat is calculated based on the equilibrium vapor sorption isotherm curves at two different temperatures as shown in **Eq. (3.7)**. The isosteric enthalpy of adsorption depends on the water contents (C_w) in the desiccant material.

$$q_{st} = \frac{R}{M_v} \cdot \ln\left[\frac{p_{v@T_1,C_w}}{p_{v@T_2,C_w}}\right]\left(\frac{T_1 T_2}{T_1 + T_2}\right) \qquad \text{Eq. (3.7)}$$

where, the R is the gas constant (8.314 J·mol^{-1}·K^{-1}) and the M_v is the water molar mass (18.01528 g·mol^{-1}). And the p_v [Pa] means that a vapor pressure at a certain temperature and water contents in the desiccant material. The adsorption heat is able to calculate from the logarithm of vapor pressures and inverse temperature according to the water content as shown in **Figure 3.13(a)**. From the water vapor sorption experimental data, the adsorption heat is calculated by **Eq. (3.7)** as indicated in **Figure 3.13(b)**. The enthalpy of the adsorption (or desorption) going to saturation to the enthalpy of the condensing (or vaporization). Thus, the adsorption heat is able to estimate by fitting the data like **Eq. (3.8)**.

$$q_{st} = i_{fg}[1 + 0.002923 - 0.03770 \ln(C_w)] \qquad \text{Eq. (3.8)}$$

where, i_{fg} is the enthalpy of condensing (or vaporization).

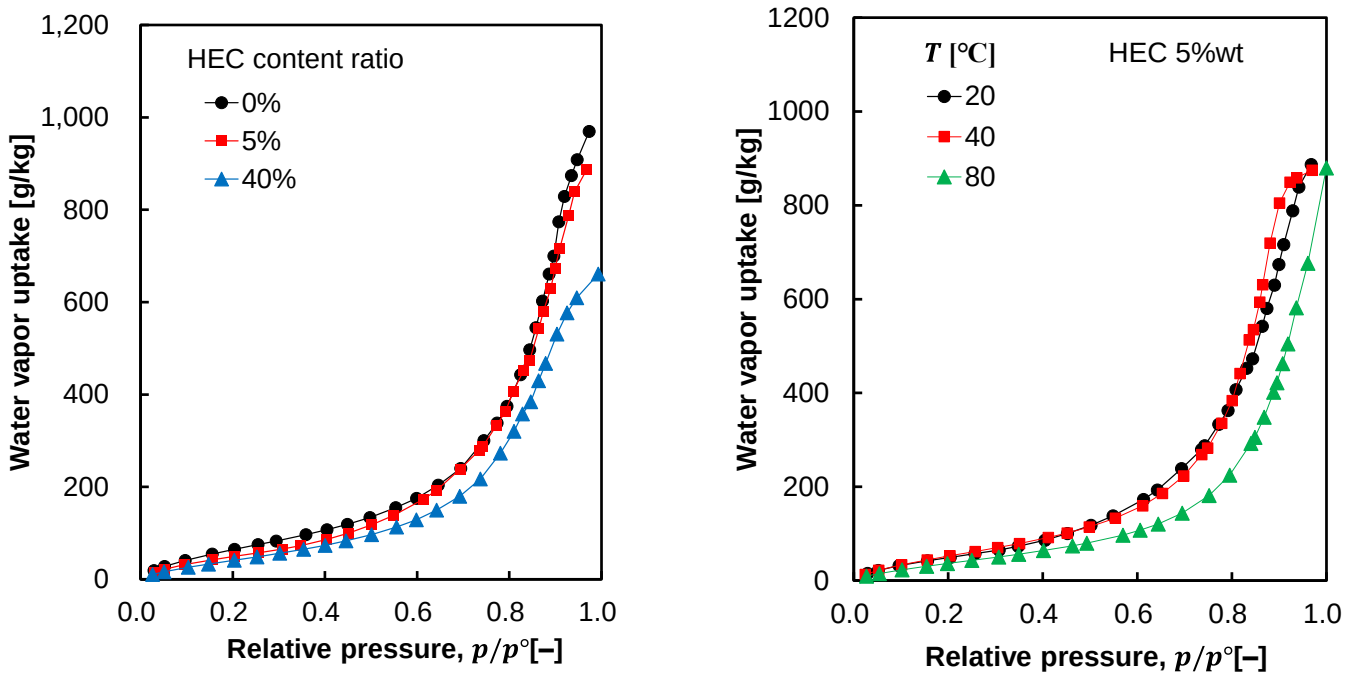

(a) (b)

Figure 3.12 Equilibrium adsorption isotherms of water vapor uptake: (a) according to the binder content ratio under the ambient temperature is 20ºC, (b) according to the ambient temperature of the binder content ratio is 5%.

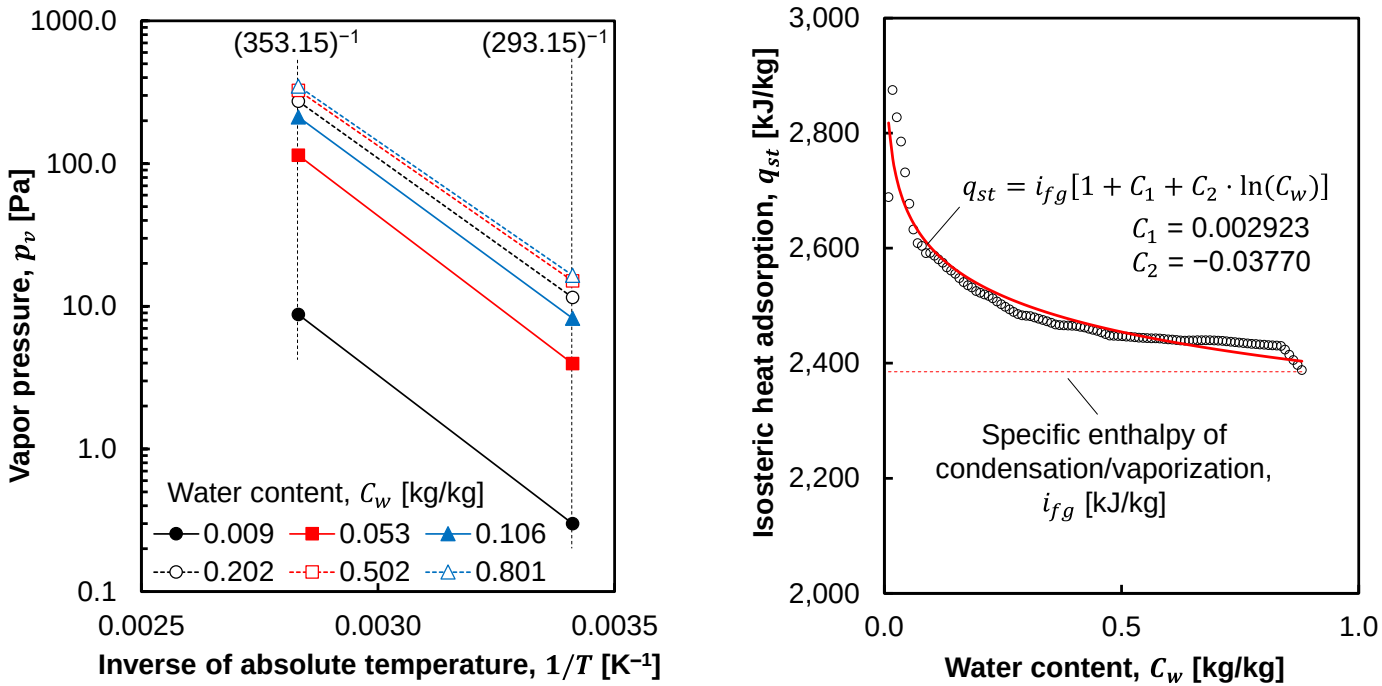

(a) (b)

Figure 3.13 Isosteric adsorption heat charts; (a) Vapor pressure versus inverse temperature corresponding to water contents according to the vapor sorption experimental data between 20 and 80 °C, (b) Isosteric heat of sorption as a function of the water content.

3.3. Numerical analysis of the DCHE

The DCHE is divided into small elements along tubes to calculate the heat and mass balance that the discrete control volume includes the tube segment with fins and adsorbent material as illustrated in **Figure 3.14**. A segment is assumed as lumped, and one-dimensional. The resistance network is applied to determine the heat transfer across the element. The overall heat resistance is expressed as the sum of all the heat resistances of each layer as in **Eq. (3.32)**, and by ignoring the heat losses and storage, it is assumed that the heat transfer amounts are equal ($\dot{Q} = \dot{Q}_{out} = \dot{Q}_d = \dot{Q}_f = \dot{Q}_t = \dot{Q}_{in}$).

$$R_{tot} = R_{in} + R_t + R_f + R_d + R_{out} \qquad \text{Eq. (3.9)}$$

The thermal resistance of inside (R_{in}) is defined as **Eq. (3.10)**. The Nusselt number of the coolant is determined by the Gnielinski semi-empirical correlation [84] using the Reynolds number (Re_w), the Prandtl number (Pr_w), and the Filonenko friction factor (f) as shown in **Eq. (3.12)** to **Eq. (3.15)**. The heat transfer coefficient of the coolant (h_w^H) is obtained by substituting the Nusselt number in **Eq. (3.11)**.

$$R_{in} = \frac{1}{h_w^H A} \qquad \text{Eq. (3.10)}$$

$$h_w^{\mathrm{H}} = \frac{\mathrm{Nu}_w \cdot k_w}{D_h} \qquad \text{Eq. (3.11)}$$

$$\mathrm{Re}_w = \frac{\rho u D_h}{\mu} \qquad \text{Eq. (3.12)}$$

$$\mathrm{Pr}_w = \frac{\mu c_p}{k} \qquad \text{Eq. (3.13)}$$

$$f = (1.58 \ln \mathrm{Re}_w - 3.28)^{-2} \qquad \text{Eq. (3.14)}$$

$$\mathrm{Nu}_w = \left(\frac{k}{D_h}\right) \frac{(\mathrm{Re}_w - 1000)\mathrm{Pr}_w \left(\frac{f}{2}\right)}{1 + 12.7\sqrt{\frac{f}{2}}\left(\mathrm{Pr}_w^{2/3} - 1\right)} \qquad \text{Eq. (3.15)}$$

The thermal resistance of the tube and the desiccant is calculated **Eq. (3.16)** and **Eq. (3.17)**.

$$R_t = \frac{\ln(r_o/r_i)}{2\pi k L} \qquad \text{Eq. (3.16)}$$

$$R_o = \frac{1}{\eta_{os} h_a^H A_{tot}} \qquad \text{Eq. (3.17)}$$

$$h_a^H = \frac{\rho_a c_{p,a} V_{\max}}{j \cdot \mathrm{Pr}^{1/3}} \qquad \text{Eq. (3.18)}$$

The convective heat transfer rate on the air-side (h_a^H) is obtained by **Eq. (3.18)** from the Colburn j factor [85] as following **Eq. (3.19)** to **Eq. (3.24)**.

$$j = 0.086 \mathrm{Re}_{D_c}^{P3} N_{row}^{P4} \left(\frac{F_p}{D_c}\right)^{P5} \left(\frac{F_p}{D_h}\right)^{P6} \left(\frac{F_p}{P_t}\right)^{-0.93} \qquad \text{Eq. (3.19)}$$

$$\mathrm{P3} = -0.361 - \frac{0.042 N_{row}}{\ln(\mathrm{Re}_{D_c})} + 0.158 \ln\left[N_{row}\left(\frac{F_p}{D_c}\right)^{0.41}\right] \qquad \text{Eq. (3.20)}$$

$$\mathrm{P4} = -1.224 - \frac{0.076\left(\frac{P_l}{D_h}\right)^{1.42}}{\ln\left(\mathrm{Re}_{D_c}\right)} \quad \text{Eq. (3.21)}$$

$$\mathrm{P5} = -0.083 + \frac{0.058N}{\ln\left(\mathrm{Re}_{D_c}\right)} \quad \text{Eq. (3.22)}$$

$$\mathrm{P6} = -5.735 + 1.21\ln\left(\frac{\mathrm{Re}_{D_c}}{N}\right) \quad \text{Eq. (3.23)}$$

$$D_h = \frac{4A_cL}{A_0} \quad \text{Eq. (3.24)}$$

Where the F_p is fin pitch. The P_l, P_t are longitudinal tube pitch and transverse tube pitch, respectively. D_h is hydraulic diameter, D_c is fin collar outside diameter. The overall surface efficiency (η_{os}) in **Eq. (3.17)** is computed using the Schmidt equation [86], **Eq. (3.25)**. The fin efficiency (η_{fin}) is determined by the **Eq. (3.26)** to **Eq. (3.28)**.

$$\eta_{os} = 1 - \frac{A_{fin}}{A_{tot}}\left(1 - \eta_{fin}\right) \quad \text{Eq. (3.25)}$$

$$\eta_{fin} = \frac{\tanh(\xi r_o Z)}{\xi r_o Z} \quad \text{Eq. (3.26)}$$

$$\xi = \sqrt{\frac{2h_a^H}{k_{fin}\delta_{fin}}} \quad \text{Eq. (3.27)}$$

$$Z = \left(\frac{R_{eq}}{r_o} - 1\right)\left[1 + 0.35\ln\left(\frac{R_{eq}}{r_o}\right)\right] \quad \text{Eq. (3.28)}$$

The geometric factors for staggered tubes are determined as **Eq. (3.29)** to **Eq. (3.31)**.

$$\frac{R_{eq}}{r_o} = 1.27\frac{X_M}{r_o}\sqrt{\frac{X_L}{X_M} - 0.3} \quad \text{Eq. (3.29)}$$

$$X_L = \sqrt{\left(\frac{L_t}{2}\right)^2 + L_l^2} \quad \text{Eq. (3.30)}$$

$$X_M = \frac{L_t}{2} \quad \text{Eq. (3.31)}$$

The heat transfer to air from the desiccant-coated fins is obtained by **Eq. (3.33)** and **Eq. (3.34)**. In general, the performance of the air-to-water heat exchanger strongly depends on the heat transfer coefficient of the air-side, because it is much smaller than the heat transfer coefficient of the water-side. Thus, the heat transfer correlations that are obtained from the DCHE experiment data [87] are adopted. The heat exchanger surface efficiency is determined according to the heat exchanger geometric information, such as staggered tubes, and straight-rectangular fins.

$$R_{tot} = R_{in} + R_t + R_f + R_d + R_{out} \quad \text{Eq. (3.32)}$$

$$\dot{Q}_{out} = h_{out}^H A_{tot}(T_a - T_1) + \dot{Q}_{ads} = \frac{(T_a - T_1) + \dot{m}_v^{ad} q_{st}}{R_{out}} \quad \text{Eq. (3.33)}$$

$$h_{out}^H = \mathrm{Nu}_a \cdot \frac{k_a}{d_h} = 0.113\mathrm{Re}_a^{0.147}\mathrm{Pr}_a^{0.4} \cdot \frac{k_a}{d_h} \quad \text{Eq. (3.34)}$$

$$\dot{Q}_{tot} = \frac{(T_a - T_b) + \dot{m}_v^{ad} q_{st} \cdot R_{out}}{R_{tot}} \quad \text{Eq. (3.35)}$$

Unlike an ordinary heat exchanger, the DCHE model needs to consider the heat generation ($\dot{Q}_{ads}$), because the water vapor changes its phase in a desiccant,

as in **Eq. (3.35)**. The uptake amount is dependent on the mass transfer between air and desiccant layer, as in the following **Eq. (3.36) to Eq. (3.38)**. Like the heat transfer assumption, the mass transfer has no losses at every layer ($\dot{m}_v^{ad} = \dot{m}_{v,a} = \dot{m}_{v,d}$), and the water molecule reaches an equilibrium state at every time-step. The overall mass transfer coefficient is determined as **Eq. (3.39)** using the mass transfer coefficient of the air-side and desiccant layer. From the experiment research [87], the coefficient of correlation for air-side mass transfer (h_a^M) is determined as shown in **Eq. (3.40)**. To calculate h_a^M, the Schmidt number (Sc_a) and the binary diffusivity of water vapor in the air (D_{va}) are derived as in **Eq. (3.41)** and **Eq. (3.42).** The D_{va} is determined using the Fuller, Schettler, and Giddings (FSG) equation.

$$\dot{m}_v^{ad} = h_{tot}^M A_{tot} \rho_a (w_a - w_d) \quad \text{Eq. (3.36)}$$

$$\dot{m}_{v,a} = h_a^M A_{tot} \rho_a (w_a - w_1) \quad \text{Eq. (3.37)}$$

$$\dot{m}_{v,d} = h_d^M A_{tot} \rho_a (w_1 - w_d) \quad \text{Eq. (3.38)}$$

$$h_{tot}^M = \left(\frac{1}{h_a^M} + \frac{1}{h_d^M} \right)^{-1} = \frac{h_a^M \cdot h_d^M}{h_a^M + h_d^M} \quad \text{Eq. (3.39)}$$

$$h_a^M = 0.079 \cdot \mathrm{Re}_a^{0.71} \cdot \mathrm{Sc}_a^{0.37} \cdot \frac{D_{va}}{d_h} \quad \text{Eq. (3.40)}$$

$$\mathrm{Sc}_a = \frac{\nu}{D_{va}} \quad \text{Eq. (3.41)}$$

$$D_{va} = \frac{10^{-3} T^{1.75} \left(\frac{1}{M_v} + \frac{1}{M_a}\right)^{1/2}}{\frac{P_a}{101.325}\left[\left(v_v^{diff}\right)^{1/3} + \left(v_a^{diff}\right)^{1/3}\right]^2} \qquad \text{Eq. (3.42)}$$

$$= 1.1915 \times 10^{-3} \frac{T^{1.75}}{P_a}$$

Where, the molar mass of dry air was postulated as the composition with 78% oxygen, 21% nitrogen, and 1% argon ($M_a = 0.78 \cdot 28 + 0.21 \cdot 32 + 0.01 \cdot 40 = 28.96$). And the diffusion volume of water vapor (v_v^{diff}) is 12.7 and diffusion volume of the air (v_a^{diff}) is 20.1 [88]. Therefore, the binary diffusivity of water vapor in the air (D_{va}) is simplified that only depends on the temperature and pressure. The humidity ratio of the air (w_a) is calculated by using relative humidity (ϕ_a), the total pressure of the humid air (P_a), and saturation pressure (P_{sat}) as shown in **Eq. (3.43)**.

$$w_a = \frac{M_v}{M_a} \frac{\phi_a}{\frac{P_a}{P_{sat@T_a}} - \phi_a} \qquad \text{Eq. (3.43)}$$

The diffusion mechanism of water molecules in the desiccant layer follows the first Fick's law, as shown in **Eq. (3.44)**. The overall diffusion coefficient in the desiccant (D_{vd}) is obtained by summation of the effective surface diffusion coefficient (D_{vs}^*) and the effective pore diffusion coefficient (D_{vp}^*) as represented **Eq. (3.45)**. The surface diffusion is the migration of adsorbed molecules on the pore surface. The effective surface diffusion considers the tortuosity that is indicated by the increased diffusional length compared with

the straight path in the adsorbent, as in **Eq. (3.46)**. The pore diffusion coefficient (D_{vp}) is able to express as resistance in series with the molecular diffusivity (D_{vm}) and Knudsen diffusivity (D_{vK}) that are obtained by **Eq. (3.47)** to **Eq. (3.49)**. Because the molecular diffusion and Knudsen diffusion compete with one another [89]. Generally, the Knudsen diffusion process is predominated under the small pore diameter in which molecule-pore wall collisions dominate over molecule-molecule collisions. On the contrary, molecular diffusion is significant when the molecule-pore wall collisions can be ignored [90].

$$h_d^M = \frac{D_{vd} \cdot \rho_a}{0.5\delta_d} \qquad \text{Eq. (3.44)}$$

$$D_{vd} = D_{vs}^* + D_{vp}^* \qquad \text{Eq. (3.45)}$$

$$D_{vs}^* = \frac{1}{\tau_d} \cdot D_0 \cdot \exp\left(\frac{-0.974 \times 10^{-3} \cdot q_{st}}{T_d}\right) \qquad \text{Eq. (3.46)}$$

$$D_{vp}^* = \frac{\varepsilon_d}{\tau_d}\left(\frac{1}{D_{vm}} + \frac{1}{D_{vK}}\right)^{-1} \qquad \text{Eq. (3.47)}$$

$$D_{vm} = 1.758 \times 10^{-4} \cdot \frac{T_d^{1.685}}{P_a} \qquad \text{Eq. (3.48)}$$

$$D_{vK} = \frac{d_{pore}}{3}\left(\frac{8\kappa \mathrm{N_{av}} T_d}{\pi M_v}\right)^{1/2} = 11.43 d_{pore} T_d^{1/2} \qquad \text{Eq. (3.49)}$$

where, ε_d is the porosity of the desiccant, and d_{pore} is the pore diameter. The Knudsen diffusion for diffusing water molecule is able to simplify since Boltzmann constant $\left(\kappa = 1.38 \cdot 10^{-16}\ \frac{\mathrm{g \cdot cm}}{\mathrm{s^2 K}}\right)$, Avogadro number $\left(\mathrm{N_{av}} = 6.022 \cdot\right.$

$10^{23}\ \frac{molecules}{mol}$), and molar mass of vapor ($M_v = 18$) are physical constant. Thus, the Knudsen diffusivity (D_{vK}) is dependent on the pore diameter, and vapor molecular weight, and temperature as shown in **Eq. (3.49)**.

The desiccant temperature, T_d, is affected by two phenomena. The first one is the generated heat according to the amount of adsorbed water vapor. The other is heat transfer by temperature differences between the brine and air. Thus, the desiccant temperature is obtained by iterating the calculation, until the difference between an initial guess value and a newly calculated temperature is within tolerance.

From **Eq. (3.50) and Eq. (3.51)**, the humidity ratio in the desiccant is obtained by the empirical correlation of the silica-gel, which is used in the DCHE as absorbent.

$$w_d = \frac{M_v}{M_a}\frac{\phi_d}{\frac{P_a}{P_{sat@T_d}} - \phi_d} \qquad \text{Eq. (3.50)}$$

$$\begin{aligned}\phi_d = &-1.41969225 \cdot 10^1 + 1.4420264 \cdot 10^{-1} \cdot T_d \\ &-4.87240277 \cdot 10^{-4} \cdot T_d^2 + 5.474215 \cdot 10^{-7} \cdot T_d^3 \\ &+4.91709025 \cdot C_w - 9.11355854 \cdot C_w^2 + 5.46807956 \cdot C_w^3\end{aligned} \qquad \text{Eq. (3.51)}$$

where, the C_w is the water contents in the silica-gel [91, 92]. The equilibrium relative humidity of the desiccant with water content (ϕ_d) is obtained by regression the **Figure 3.12(b)** which is the water vapor sorption isotherm curve.

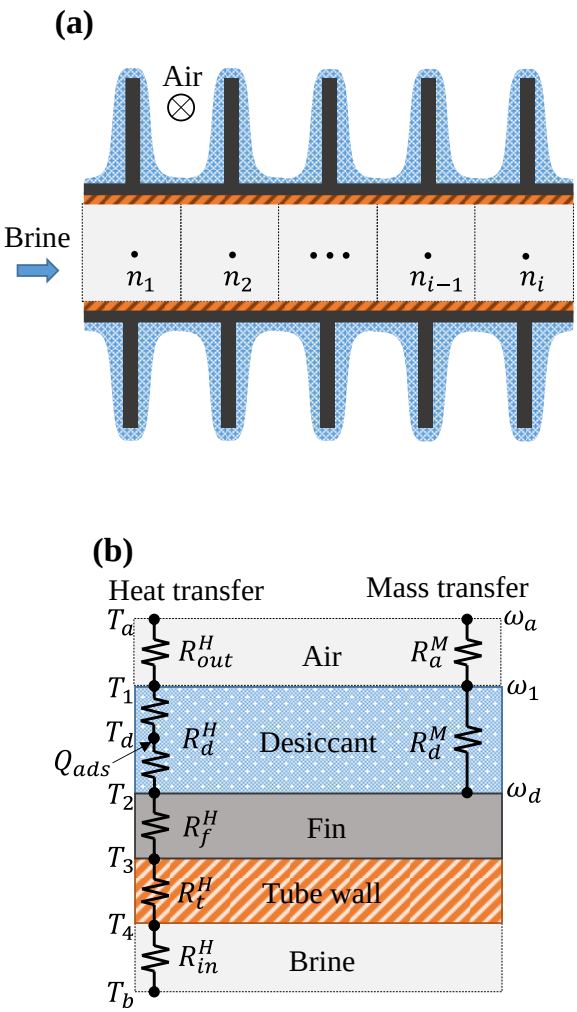

Figure 3.14 Discrete segment of the numerical model: (a) Schematic of the discretized DCHE, and (b) 1D diagram of the heat and mass transfer resistances.

3.4. Experimental of the DCHE

3.4.1. Experiment set-up of the desiccant coated heat exchanger

To investigate the performance of the desiccant coated heat exchanger (DCHE), the experimental apparatus is fabricated as shown in **Figure 3.15** and **Figure 3.16**. In the conventional automobile heat pump (MHP) system, a micro-channel heat exchanger is usually utilized to enhance the transfer performance. However, its fin pitch is too narrow for coating the additional material. Thus, the fin-tube-type heat exchanger is applied as summarized in **Table 3.4**. To analyze the performance of the DCHE, the test facility which is composited with two water bath and one air chamber. The air chamber maintains the air temperature and humidity conditions. When dehumidification mode, the cool water bath supplies the coolant to the DCHE. Meanwhile, when in regeneration mode, the hot water bath injects the waste heat source by switching solenoid valves. The dry bulb and web bulb are measured at the inlet- and outlet of the DCHE. The coolant mass flow rate is obtained by the Coriolis flowmeter. The air mass flow rate is calculated by using a pressure drop when air passes through the nozzle flow meter [93].

Table 3.4 Specification of the DCHE for the experiment.

	Parameter	Value	Unit
Heat exchanger	Width / length / height	40 / 200 / 200	[mm]
	Number of Rows / Tubes per row	2 / 8	[–]
	Diameter of tube inner / outer	7.75/ 9.53	[mm]
	Fin pitch / Thickness	2.5 / 0.25	[mm]
Desiccant layer	Thermal conductivity	0.198	[W m^{-1} K^{-1}]
	Density	500	[kg m^{-3}]
	Coated thickness	0.3	[mm]
	Porosity / Tortuosity	0.7 / 2.8	[–]

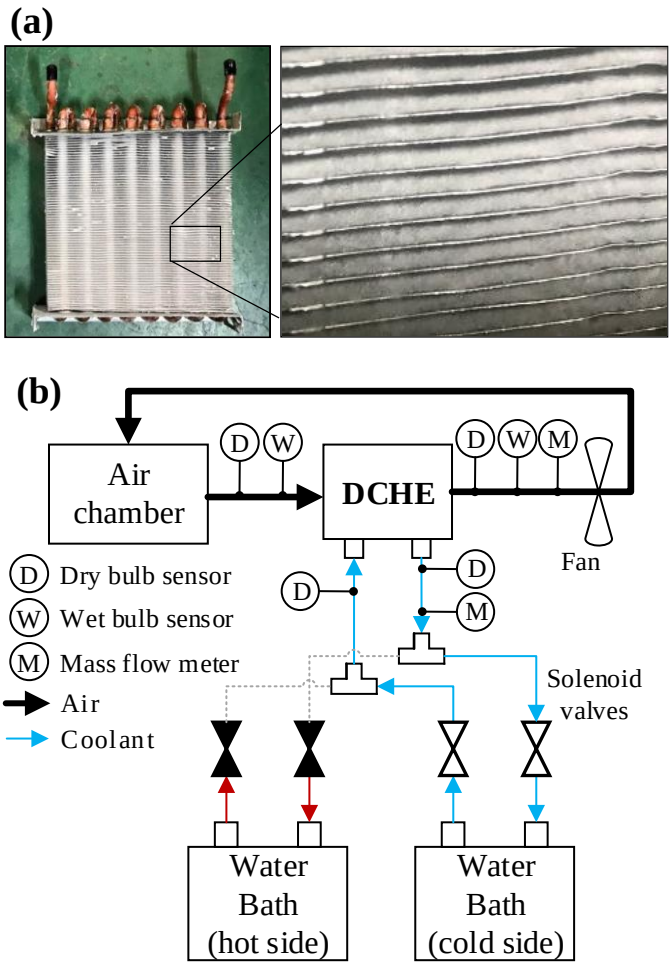

Figure 3.15 Experiment apparatus: (a) Front and detail view of the DCHE, and (b) Schematic of the experiment apparatus.

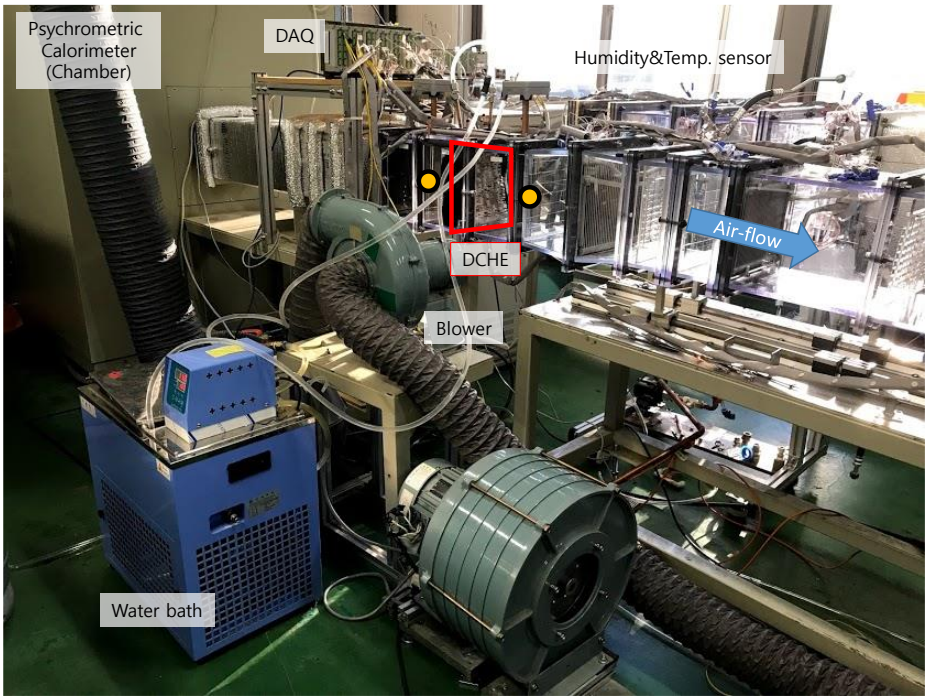

Figure 3.16 Experiment apparatus for evaluating the DCHE performance.

The experiment was conducted on various operation conditions by changing air temperature and relative humidity. In the case of the summer season, **Figure 3.17** shows the experimental results. When the coolant inlet temperature at the dehumidification process ($T_{w,DCHE,in,D}$) is lower than air temperature ($T_{a,DCHE,in}$), the adsorption performance is enhanced. To estimate the adsorption/desorption performance in the winter season, the experiment is conducted as depicted in **Figure 3.18**. The difference in the humidity ratio between the dehumidification process and regeneration mode is small because the desiccant temperature leads to decreasing the overall mass transfer coefficient as following the **Eq. (3.44)** to **Eq. (3.49)**.

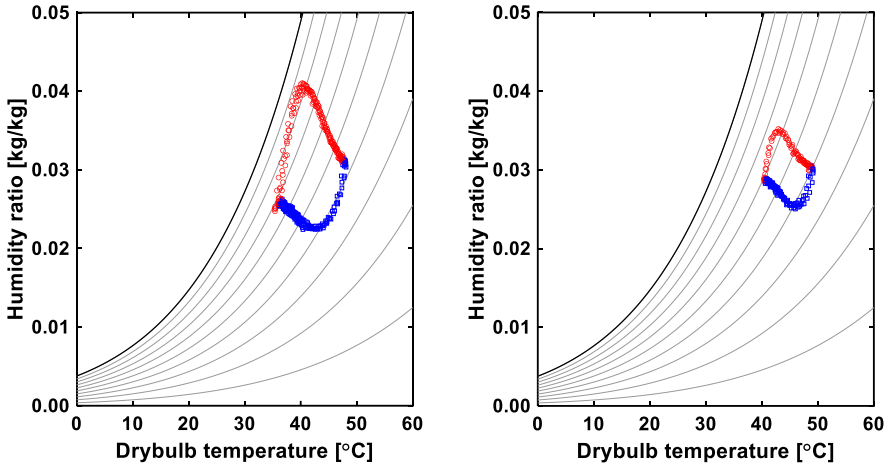

(a) (b)

Figure 3.17 The DCHE outlet air experimental data on the psychrometric chart under the various conditions for the summer season; (a) inlet air temperature ($T_{a,DCHE,in}$) is 39.9°C, inlet air relative humidity ($\phi_{a,DCHE,in}$) is 62.0%, inlet coolant temperature at dehumidification mode ($T_{w,DCHE,in,D}$) is 31.8°C, and inlet coolant temperature at regeneration mode ($T_{w,DCHE,in,R}$) is 53.0°C, and (b) $T_{a,DCHE,in}$= 40.2°C, $\phi_{a,DCHE,in}$= 61.3%, $T_{w,DCHE,in,D}$= 40.6°C, $T_{w,DCHE,in,R}$= 53.6°C: the blue squared denotes the dehumidification process, and the red circle represented the regeneration process.

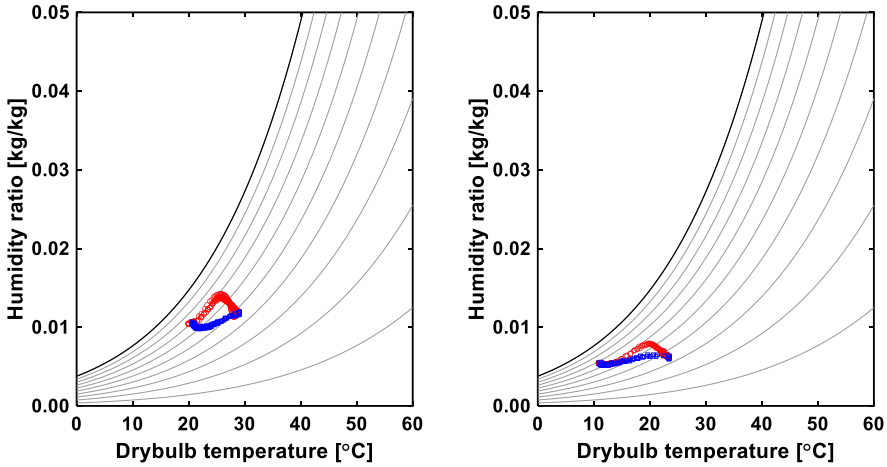

(a) (b)

Figure 3.18 The DCHE outlet air experimental data on the psychrometric chart under the various conditions for the spring and winter season; (a) inlet air temperature ($T_{a,DCHE,in}$) is 19.5°C, inlet air relative humidity ($\phi_{a,DCHE,in}$) is 81.9%, inlet coolant temperature at dehumidification mode ($T_{w,DCHE,in,D}$) is 21.3°C, and inlet coolant temperature at regeneration mode ($T_{w,DCHE,in,R}$) is 38.4°C, and (b) $T_{a,DCHE,in}$= 10.3°C, $\phi_{a,DCHE,in}$= 80.4%, $T_{w,DCHE,in,D}$= 12.2°C, $T_{w,DCHE,in,R}$= 37.0°C: the blue squared denotes the dehumidification process, and the red circle represented the regeneration process.

3.4.2. Uncertainty analysis

The uncertainty analysis is conducted to estimate the error of the experimental data. The overall uncertainty of a single variable (δ_x^U) is combined with the fixed error (δ^F) and the random error (δ^R) as shown in **Eq. (3.52)** [94]. In the equation, the t^f is the Student's *t*-distribution value from statistics reference at the specified confidence level for the appropriated degrees of freedom. The fixed error estimates are based upon instrumentation calibration results [95]. The random error is obtained by the population standard deviation as described in **Eq. (3.53)** using mean values ($\bar{x}$) which is calculated by **Eq. (3.54)**.

$$\delta_x^U = \sqrt{(\delta_x^F)^2 + (t^f \cdot \delta_x^R)^2} \qquad \text{Eq. (3.52)}$$

$$\delta_x^R = \sqrt{\frac{1}{n}\sum_{i=1}^{n}(x_i - \bar{x})^2} \qquad \text{Eq. (3.53)}$$

$$\bar{x} = \frac{1}{n}\sum_{i=1}^{n} x_i \qquad \text{Eq. (3.54)}$$

As a result, the uncertainty of temperature sensors is calculated as 0.21%. The value of the relative humidity is estimated as about 1.5% uncertainty.

Table 3.5 Specifications and uncertainties of the DCHE experimental apparatus.

Device / Sensor	Accuracy	Specification	Fixed error	Random error	Total error
Data acquisition	DC voltage: ±0.05% of rdg+5 digits Thermocouple: ±0.05% of rdg+0.5℃	-	-	-	-
Thermocouples	±0.7℃	−250~350℃	0.12%	0.09%	0.21%
Differential pressure transmitter	±1.0% F.S.	0~689.5 kPa	1.00%	0.11%	1.02%
Relative humidity transmitter	±2.5% F.S.	0~100% RH	2.50%	0.76%	1.51%
Mass flow meter	±0.1% F.S.	0~100 g/s	0.10%	0.24%	0.48%

3.4.3. Experimental validation of the DCHE model

To validate the numerical model of the DCHE, **Figure 3.19** compares the experimental data and simulation results in typical conditions. When switching over from regeneration to dehumidification mode, and *vice versa*, a certain period of time is required. Because the water that is contained in the tube from the hot bath and cold bath should be physically replaced. This means that the dead time depends on the coolant velocity and length of the water tubes. In this study, it was postulated that the dead time is 40 s, and the change of coolant temperature is linear. The simulation result in terms of a difference in the humidity ratio of the DCHE inlet and outlet shows good agreement with the experiment data, as depicted in **Figure 3.19**.

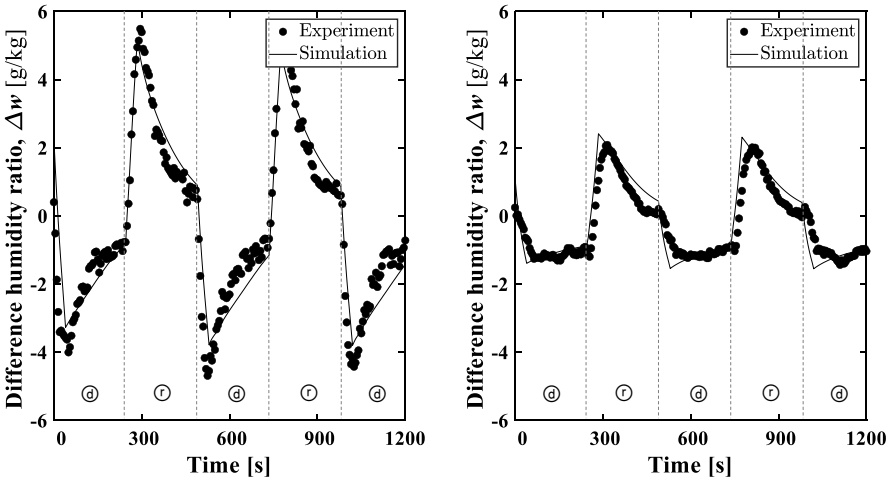

(a) (b)

Figure 3.19 Comparison between the experimental data and the numerical results of the difference in humidity ratio of the DCHE inlet and outlet ($\Delta w \equiv w_{a,DCHE,out} - w_{a,DCHE,in}$) under conditions: (a) inlet air temperature is 40.2°C, inlet air relative humidity is 60%, inlet coolant temperature at dehumidification mode is 40.6°C, and inlet coolant temperature at regeneration mode is 61.3°C, and (b) inlet air temperature is 10.3°C, inlet air relative humidity is 90%, inlet coolant temperature at dehumidification mode is 12.2°C, and inlet coolant temperature at regeneration mode is 37.1°C. The notations of circled letters are: ⓓ, the dehumidification process; ⓡ, the regeneration process.

3.5. Alternate control methods for DCHE

In the previous study, the DCHE operation modes for both adsorption and desorption are depended on the arbitrary time of about 240 s. The switching time was determined empirically through experiments. To enhance the adsorption performance of the DCHE, the dehumidification/regeneration operation mode should be controlled and optimized by an alternate control method. In this chapter, 4 types of the control method are introduced and evaluated.

3.5.1. Absolute humidity gap method

According to the mass balance, the number of the water molecule is decreased when the desiccant material adsorbs and keeps water vapor in the passing air. When the adsorption performance of the DCHE going to saturation, the difference in absolute humidity between the inlet and outlet of the DCHE ($\Delta w \equiv \left(w_{a,DCHE,out} - w_{a,DCHE,in}\right)$ will gradually decrease as shown in **Figure 3.20**. Thus, it is dedicated to switching when the Δw is below certain criteria ($\beta_{\Delta w}$). This method is simple and intuitive, but the control results will be strongly dependent on the set arbitrary value. And it is difficult to generalize the control variable. Since the decision is based on instantaneous measured data, there is a disadvantage that a wrong decision may be made if inaccurate data is gathered due to sensor error or network losses.

3.5.2. Absolute humidity slope method

To overcome the weakness of the absolute humidity gap method abovementioned, several time-series data points are used to decide the switch time in the absolute humidity slope method. This method determines the switching time using the multiple data about the absolute humidity difference between the inlet and outlet of the DCHE (Δw). In other words, the slope of Δw within the time window is calculated as depicted in **Figure 3.21**. As the slope value decrease, it is estimated that the adsorption or desorption performance is saturated.

However, this method has drawbacks. For instance, the setting slope value which is the control reference value should be set arbitrarily. Thereby, it is difficult to generalize because the slope value may vary according to change in operating conditions such as temperature, humidity, and air volumetric rate.

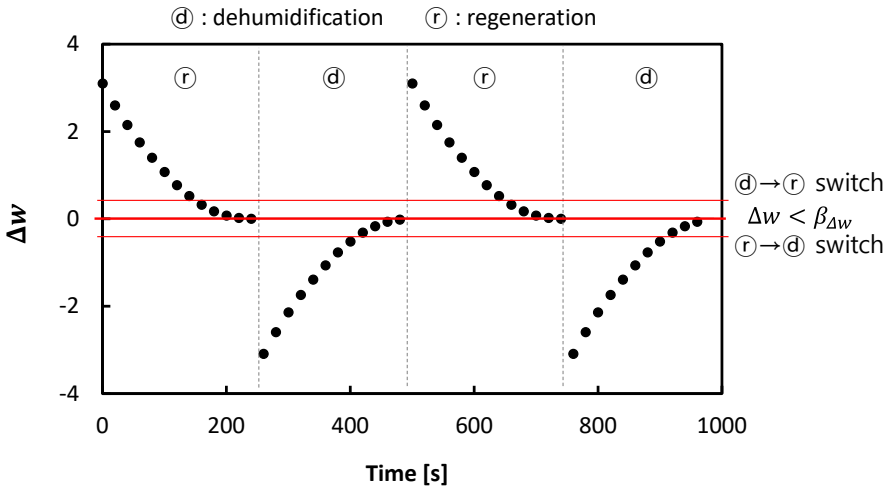

Figure 3.20 The alternate control method using an absolute humidity difference gap.

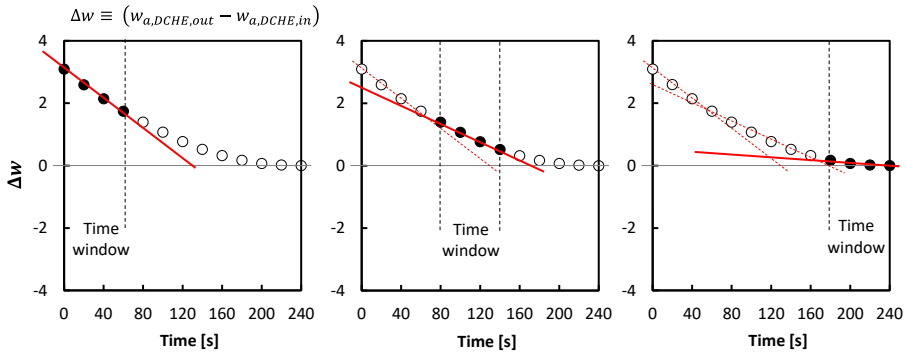

Figure 3.21 The alternate control method using absolute humidity slopes.

3.5.3. Water contents ratio method

This is a method of estimation by using the difference between maximum water content in the desiccant material and the current water content of it. If mass transfer during an infinite time, the absolute humidity difference between the air side and desiccant side will converge to 0 ($w_a - w_d \rightarrow 0$) while achieving equilibrium. Thus, the maximum water content ($C_{w,TV}$) is calculated at the humidity difference is 0. The dimensionless value (α_{C_w}) is defined as **Eq. (3.55)** to evaluate the water content state over the maximum water content capacity of the desiccant.

$$\alpha_{C_w} \equiv \frac{\left|C_{w,TV} - C_{w,PV}\right|}{C_{w,TV}} \qquad \text{Eq. (3.55)}$$

$$\lambda \equiv \left.\frac{[\int \Delta w\, dt]_{Proposed} - [\int \Delta w\, dt]_{Base}}{[\int \Delta w\, dt]_{Base}}\right|_{@\,Dehum.} \qquad \text{Eq. (3.56)}$$

According to the switching criteria, the dehumidification and regeneration processes are changed as shown in **Figure 3.22**. By comparing with the water adsorption amount of the base case which is switching every 240 s, the water adsorption amount is changed as shown in **Figure 3.23**. The DCHE is operated under the same condition as **Figure 3.19**(b). As a result, the maximum water adsorption state exists at the switching criteria, α_{C_w}, is about 0.4.

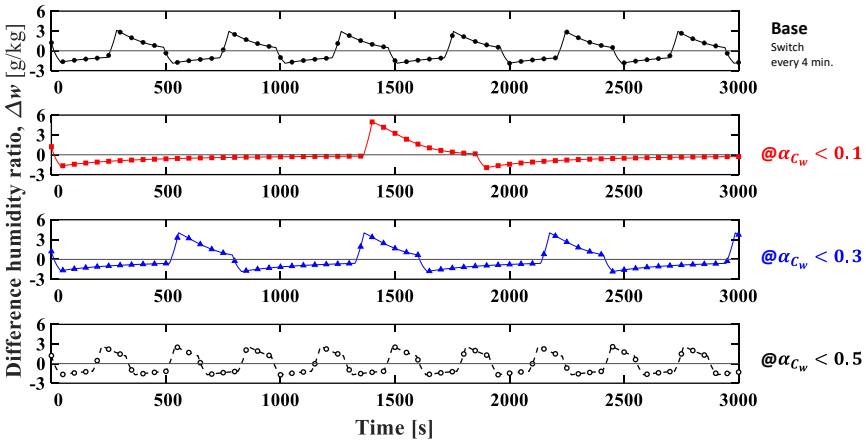

Figure 3.22 The difference humidity ratio on time series based on the switching criteria.

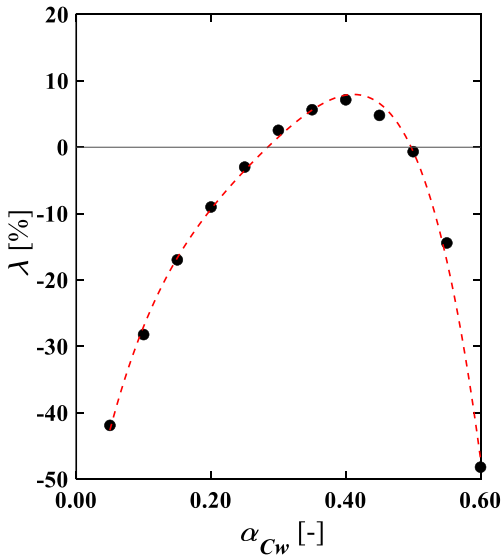

Figure 3.23 Variation of the water adsorption amount according to the switching criteria using the water contents ratio method.

Thereby, this control method might lead the better performance. However, it is more required the computing resource than the base control case. Because the water contents in the desiccant should be calculated by iterating the function of the relative humidity and temperature of the desiccant layer.

3.5.4. Integrated area ratio method

To reduce the computing resource, the integrated area ratio method is introduced. The trend of the difference humidity ratio between inlet and outlet of the DCHE (Δw) was postulated as an exponential function since the Δw is gradually decreased over time of mass transfer. As shown in **Figure 3.24**, a fitting curve is calculated based on the Δw data set during process times which reset when switching to dehumidification from regeneration mode, vise versa. Thereafter, the maximum area value (A_{max}) is obtained as the integral value from 0 to infinity time of the exponential fitting curve. And the ratio is defined like Eq. (3.57) as the present integrated area (A_{PV}) over the maximum area.

$$\alpha_A \equiv \frac{A_{PV}}{A_{max}} \qquad \text{Eq. (3.57)}$$

When the α_A is greater than the setting value, it is decided as saturated the adsorption amount of the DCHE, and the dehumidification/regeneration process is switched.

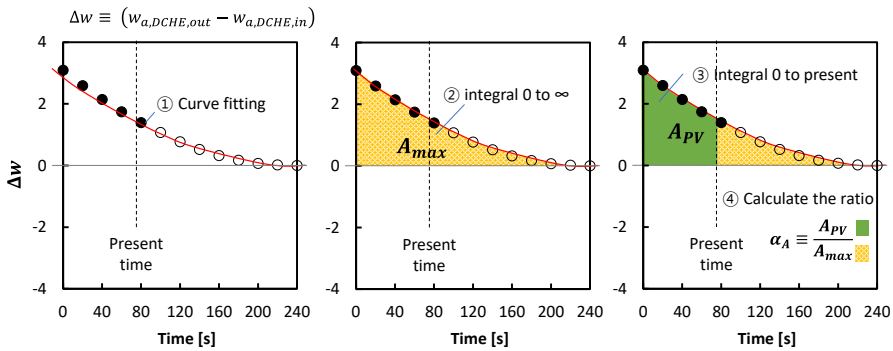

Figure 3.24 The alternate control method using the integrated area ratio.

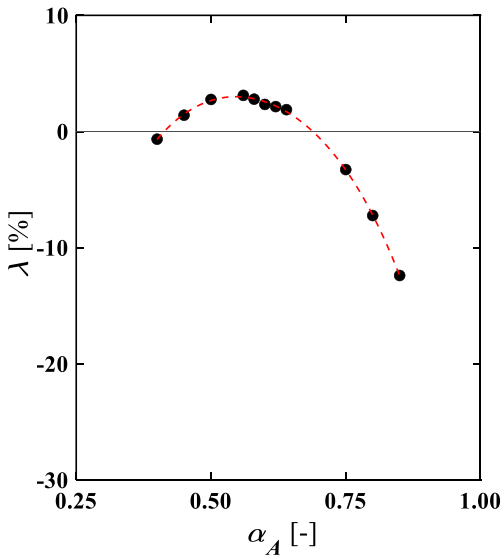

Figure 3.25 Variation of the water adsorption amount according to the switching criteria using the integrated area ratio method.

To compare the adsorption amount according to the switching criteria (α_A), the numerical analysis was conducted under the operation condition: The air flow rate is constantly supplied into the DCHE at a dry-bulb temperature of 24℃, and relative humidity of 90% regardless of dehumidification or regeneration mode. The coolant is constantly supplied as 24℃ for adsorption, 60℃ for desorption. As a result, the water adsorption amount at the α_A is 0.6 is greater than the base case which is a constant time alternative mode as revealed in **Figure 3.25**. In other operating conditions, the largest adsorption amount of the moisture exists near 0.6 of α_A.

This integrated area ratio method has a strength as compared with the water contents ratio method that it is able to configure with a small capacity microprocessor and a few sensors such as dry-bulb and wet-bulb. And it is required fewer computing resources and it is able to generalize the criteria.

3.6. Summary

In Chapter 3, the desiccant coated heat exchanger (DCHE) model was developed to predict the adsorption performance of the DCHE using the thermal resistance method. In the first section of the chapter, the principle of adsorption is discussed before evaluating the model of the DCHE. And then,

the pair of the desiccant and binder is selected. The performance of the adsorbent is strongly dependent on the physical properties of it such as the surface area, pore volume, and pore size. To measure the physical properties of the adsorbent, various tests were conducted in the second section. For instance, the surface area is determined by the BET method, and the water vapor uptake is obtained subject to the relative vapor pressure by a volumetric gas sorption analyzer. Through the experimental data, the proper binder ratio is chosen to obtain the maximum performance. In the third section, the numerical model is constructed by discrete the heat exchanger as small segments of the control volume. To validate the developed DCHE model, the test apparatus was fabricated and the experiment was conducted. As a result, the predicted performance of the DCHE shows good agreement with the experimental data. Plus, alternate control methods were considered to maximize the adsorption performance.

Chapter 4. Design and performance analysis of the heat pump

4.1. Introduction of the automobile heat pump

The conventional heat pump system is mainly composited with the compressor, outdoor heat exchanger (ODHX), indoor condenser (IDCOND), indoor evaporator (IDEVAP), and expansion valves, as presented in **Figure 1.4**. In addition, the accumulator and liquid receive might be installed to phase separate and store the excess refrigerant. Some solenoid valve is applied to control the direction of refrigerant flow.

4.1.1. Selection of the refrigerant

In a close loop cycle like the reversed Carnot cycle, the characteristic of the heat media, i.e., refrigerant, have a great effect on the performance of the system. In the conventional automobile heat pump (MHP), the R-134a is widely used. However, it will phase out because of its high global warming potential (GWP) value by environmental regulations; Kigali amendment of Montreal protocol [96] and the F-gas regulation of EU [97] require phase out the fluorinated greenhouse gases, and European Directive on a mobile air-conditioning system [98] prohibits refrigerants which have above GWP 150

value. The GWP values are referred from the fifth assessment report of the Intergovernmental Panel on Climate Change (IPCC AR5) that is calculated in terms of the 100-year warming potential of one kilogram of a gas relative to one kilogram of carbon dioxide (CO_2).

To screening the potential refrigerant for replacing the R-134a, the properties of investigated refrigerants are summarized in **Table 4.1** and the thermodynamic analysis is conducted. The degree of superheating (DSH) and degree of subcooling (DSC) are 5 K and 3 K, respectively. The isentropic efficiency of the compression process is presumed 0.85. The mass flow rate of a refrigerant is calculated by matching the given heating capacity, 5 kW. The volumetric heating capacity (VHC) and heating coefficient of performance (COP_H) are defined as following **Eq. (4.1)** and **Eq. (4.2)**.

$$VHC \equiv \frac{\dot{Q}_{COND}}{\dot{m}_r \rho_{r,COMP,in}} \qquad \text{Eq. (4.1)}$$

$$COP_H \equiv \frac{\dot{Q}_{COND}}{\dot{W}_{COMP}} \qquad \text{Eq. (4.2)}$$

Figure 4.1 reveals that phase change pressures of the closed refrigerant cycle at the condensing temperature is 45℃, and evaporating temperatures are −20℃ or 10℃, and discharge compressor discharge temperature according to the type of refrigerant for understanding the operating temperature and pressure region. Too high pressure has required the change of the pipe and valves to

withstand it. And excess discharge temperature might be led that losses the lubricant film on the compressor inside walls, oil breakdown (chemical decomposition), acceleration metal fatigue, and melt down the electrical insulation, *i.e.*, enamel, of the motor wire [99-101].

In 2019, the project using R-161 was granted the annual international award of the American Society of Heating, Refrigerating and Air-Conditioning Engineers (ASHRAE) and United Nations Environment Programme (UNEP) for residential applications [102]. Because a system using R-161 shows good performance with a GWP value of 4 and an ODP value of 0. However, R-161 is not an alternative refrigerant yet since its toxicity testing is incomplete and high flammability [103]. Natural hydrocarbons such as R-290 (propane) and R-600a (iso-butane) also have been considered as a refrigerant for applicating a secondary loop [104-106]. Even though hydrocarbons have lower GWP values, but the hydrocarbon natural refrigerants are classified as A3 of the ASHRAE safety classification due to the higher flammability [107]. Usually, there are trade-offs between GWP and flammability. To decrease the GWP of refrigerant, halogens —fluorine (F), chlorine (Cl), or bromine (Br) — are replaced with hydrogen (H), thus it decreases the atmospheric life by reacting with atmospheric hydroxyl radicals(·OH) [108]. But it leads to unstable and increasing flammability [109]. In the case of R-32, it has been widely used as a

base refrigerant of mixtures since it not only is able to manufacture freely without royalty payment but also has a lower GWP value than second-generation refrigerants that have high GWP such as R-12 or R-22. However, R-32 is also needed to phase out because of medium GWP, i.e. 677. The blend refrigerant is considered possibly based on low-GWP refrigerant, R-1234yf with conventional refrigerant, R-134a [110]. For instance, the zeotropic mixture R-451A, which is composited with R-1234yf (89.8%) and R-134a (10.2%), and the azeotropic mixture R-513A, which is composited with R-1234yf (56%) and R-134a (44%). But the GWP value of R-513A is over the GWP 150 because of the high composition of the R-134a.

Table 4.1 Selected properties of the investigated refrigerants.

Property	R-134a	R-152a	R-1234yf	R-161	R-290	R-600a	R-32	R-451A	R-513A
Molar mass [kg/kmol]	102.03	66.05	114.04	48.06	44.10	58.12	52.02	112.69	108.43
Normal boiling point [°C]	−26.07	−24.02	−29.49	−37.54	−42.11	−11.75	−51.65	−29.76± 0.0065	−29.53± 0.0515
Critical temperature [°C]	101.06	113.26	94.70	102.10	96.74	134.66	78.11	94.36	94.91
Critical pressure [kPa]	4059	4517	3382	5046	4251	3629	5782	3443	3648
Heat of vaporization @ 45°C [kJ/kg]	157.6	252.9	127.4	299.8	296.3	305.3	224.0	129.1	136.9
ASHREA safety rating	A1	A2	A2L	A3*	A3	A3	A2	A2L	A1
Occupational exposure limit (OEL) [g/m^3]	1000	1000	500	1800**	1000	1000	1000	530	65
Refrigerant concentration limit (RCL) [g/m^3]	210	32	75	not yet	9.5	9.5	77	81	320
Lower flammability limit (LFL) [g/m^3]	-	130	289	15	38	38	306	326.6	-
Ozone depletion potential (ODP) [−]	0	0	0	0	0	0	0	0	0
Global warming potential over 100-year (GWP_{100}) [−]	1300	138	4	12	3.3	3	677	136.2	574.2

* anticipated classification / ** the toxicity test shows that OEL of R-161 is 1822 ppm when mouse suck the refrigerant for 28 days [111].

The thermodynamic analysis results are present in **Figure 4.2**. As a result, the volumetric heating capacity and theoretical heating COP is are increased as low evaporating temperature regardless of the refrigerant type. The R-32 shows the best volumetric heating capacity. But it required that the compressor re-designs to adjust displacement. The heating COP of R-152a is calculated as the better merit than others. Therefore, in this study, three types of refrigerant were considered; the R-134a for the base case, R-1234yf, which has the lowest GWP, and R-152a, which has the best COP.

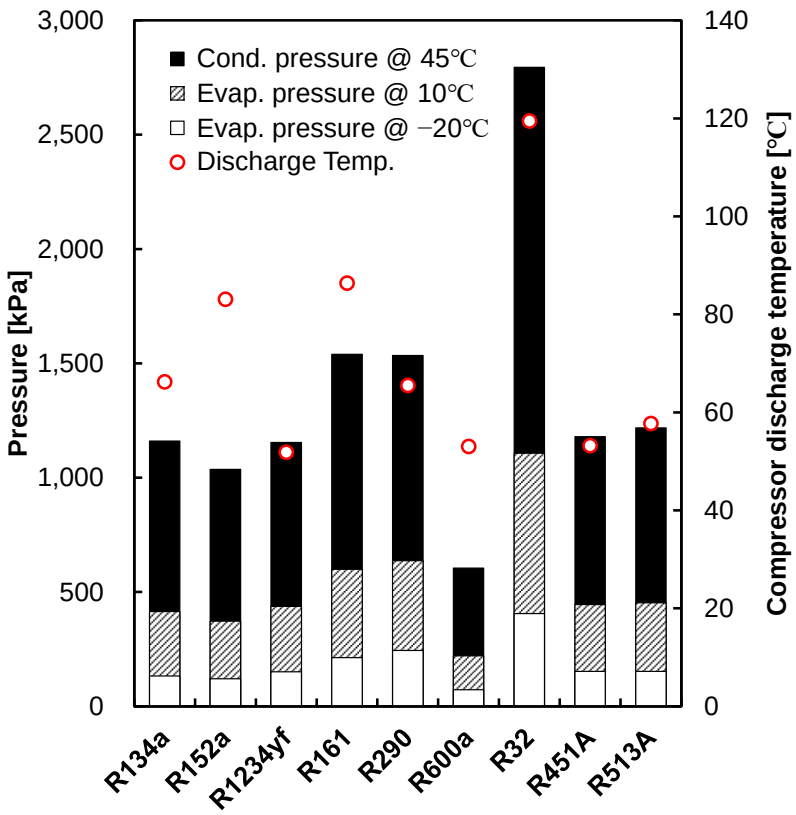

Figure 4.1 Pressure and compressor discharge temperature on various refrigerants.

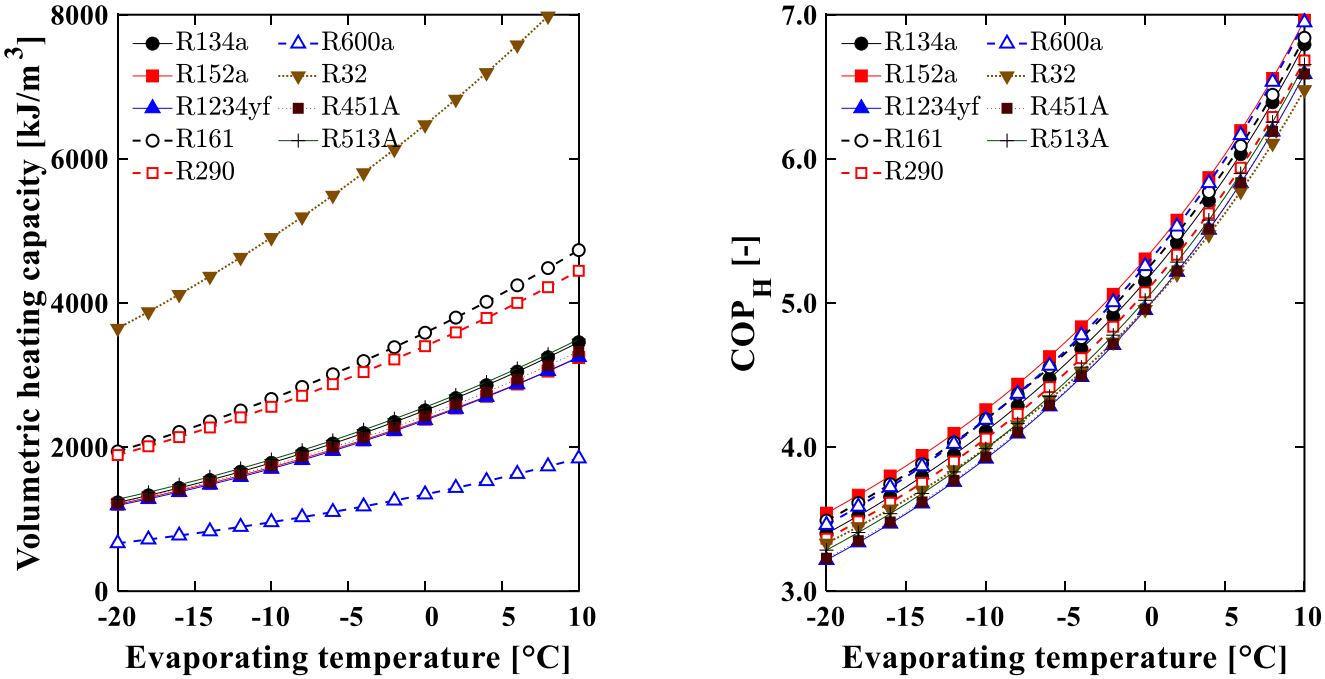

(a) (b)

Figure 4.2 The effect of evaporator temperature on (a) volumetric heating capacity (VHC) and (b) the heating coefficient of performance (COP_H) at condensing temperature of 45ºC.

4.1.2. Selection of the lubricant

The refrigerant lubricant is essential in the vapor compression cycle for reducing friction, preventing wear, and sealing. When selecting the suitable lubricant with the refrigerant, the solubility, miscibility, and viscosity. Most of all, the compatibility of compressor oil with refrigerant is crucial because the mismatching might lead to decreasing the compressor lifetime and performance, reduce heat transfer, deteriorate pressure drop, and clogging the expansion device [112-114].

The suitability of a typical refrigerant is summarized in **Table 4.2** [115]. In this study, the 100 viscosity-grade polyol-ester oil (POE VG 100) was selected to utilize both the HFC refrigerant (R-134a, R-152a) and HFO refrigerant (R-1234yf).

Table 4.2 Compressor lubricant and suitability with refrigerant type.

	Hydrocarbon (HC)	**CFC, HCFC**	**HFC + blends**	**HFO+ HFC blends**	**R-717 (NH_3), R-723**	**R-744 (CO_2)**
Mineral-oil (MO)	○,HV	○	×	×	○	×
Alkyl-benzene (AB)	△,HV	○	△	×	△	×
MO + AB	△,HV	○	×	×	△	×
Poly-alpha-olefin (PAO)	○,HV	△	×	×	○	△
Polyol-ester (POE)	○,CW,HV	△,CW,HV	○	○	×	○
Poly-vinyl-ether (PVE)	×	×	○	×	×	×
Poly- glycols (PAG)	△	×	△,CW	△,CW	△,CW	○
Petroleum hydrocarbons (PHC)	×	×	×	×	○	×

* ○: good suitability, △: Suitability with limitations, ×: Not good, CW: critical for moisture, HV: Possibly higher base viscosity

4.2. Numerical analysis of the automobile heat pump

4.2.1. Calculation method and assumption

The automotive heat pump system (MHP) consists of a compressor, heat exchangers, and expansion device. To investigate the performance of the MHP, a numerical model is built. The potential and kinetic energy changes were neglected in the vapor compression cycle. To simplify the model, the pressure drops and heat losses were postulated as being negligible. Also, the refrigerant lubricant effects and the influence of the frost growth on the outdoor heat exchanger on the performance were not considered in this numerical study. The model is converged in order to calculate thermodynamic properties at steady-state using two parameters; the degree of superheat (DSH) and the refrigerant charge amount. Because the performance of refrigeration or heat pump systems depends on the refrigerant charge amounts [116, 117]. On the other hand, the DSH is postulated as 5 K to protect the compressor from wet compression. The simulation model had been iterated until it is less than convergence tolerance that differential errors of the refrigerant amount and DSH between the given values and the calculated values as presented in **Figure 4.3**.

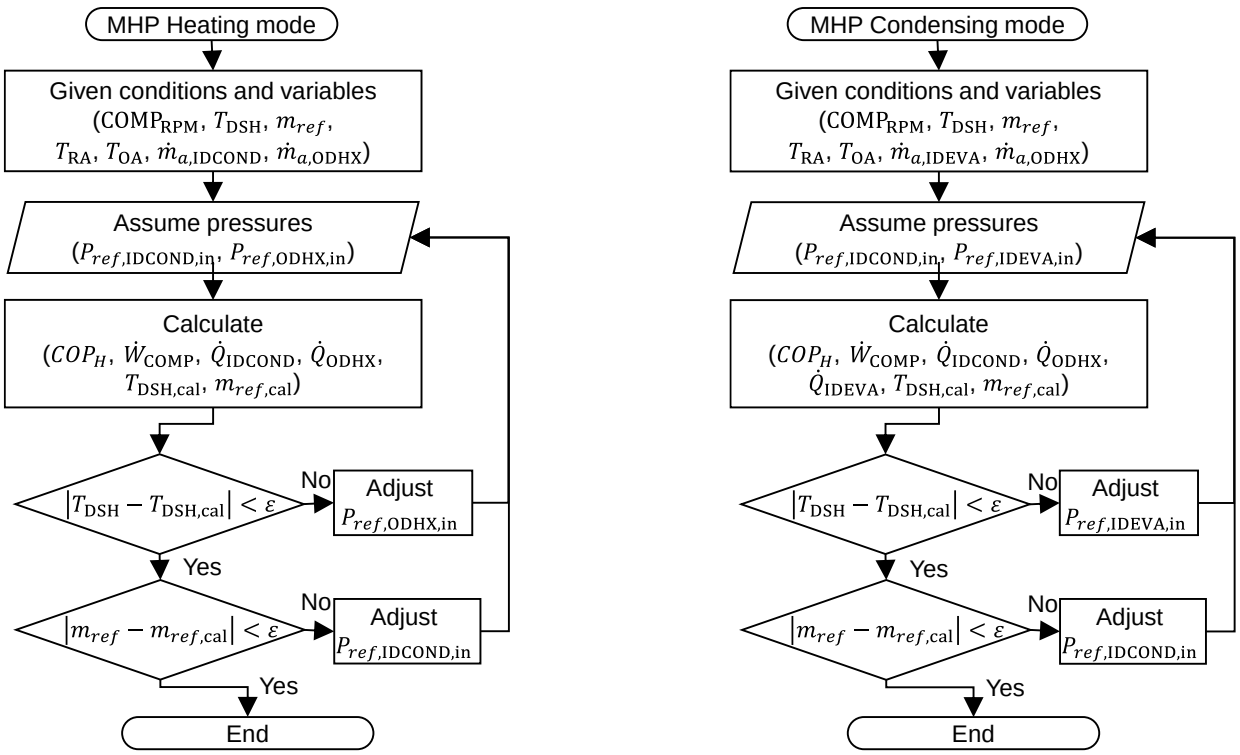

Figure 4.3 Flow chart of the MHP simulation; (a) the heating mode, and (b) the condensing mode.

4.2.2. Compressor

The compressor is the crucial equipment to determine the performance of the system due to the most energy-consuming device in the heat pump system. Thus, the model of a scroll-type compressor, usually employed in a vehicle, was developed by using experimental data to improve reliability. The compressor performance is affected by isentropic efficiency, volumetric efficiency, and mechanical efficiency. Actual discharge enthalpy is determined by isentropic efficiency (η_{isen}) as shown in **Eq. (4.3)**. The mass flow rate of the refrigerant and the power consumption are obtained by **Eq. (4.4)** and **Eq. (4.5)** using the volumetric efficiency (η_{vol}) and mechanical efficiency (η_{mech}), respectively.

$$i_{r,COMP,out} = i_{r,COMP,in} + \frac{\left(i_{r,COMP,out,ideal} - i_{r,COMP,in}\right)}{\eta_{isen}} \qquad \text{Eq. (4.3)}$$

$$\dot{m}_r = \eta_{vol} \cdot \rho_{r,COMP,in} \cdot (Vol)_{COMP} \cdot (Hz)_{COMP} \qquad \text{Eq. (4.4)}$$

$$\dot{W}_{COMP} = \dot{m}_r\left(i_{r,COMP,out} - i_{r,COMP,in}\right)/\eta_{mech} \qquad \text{Eq. (4.5)}$$

where, $(Hz)_{COMP}$ is the revolution speed of the compressor and $(Vol)_{COMP}$ is represented displacement volume. The displacement volume of the scroll compressor is 33 cc in this study. Thus, the mass flow rate of the refrigerants has a proportional relationship with the revolution speed of the compressor.

4.2.3. Heat exchangers

The heat exchangers discrete small elements and the amount of the heat transfer is calculated using the effectiveness-NTU method.

$$Q_{HX} = \sum \varepsilon\, C_{min}\left(T_{r,i} - T_{a,i}\right)\Big|_{i=element} \qquad \text{Eq. (4.6)}$$

Where, the effectiveness (ε) is determined as following the phase of the refrigerant. When the refrigerant is a single-phase, the effectiveness (ε) is calculated by **Eq. (4.7)**. On the other hand, the ε of the two-phase is obtained by **Eq. (4.8)**. The ratio of heat capacity rate (C_r) and the number of transfer unit (NTU) are defined as **Eq. (4.9)** and **Eq. (4.10)**, respectively.

$$\varepsilon = (1 - \exp(C_r^{-1}) \cdot NTU^{0.22}) \cdot (\exp(-C_r NTU^{0.78}) - 1) \qquad \text{Eq. (4.7)}$$

$$\varepsilon = 1 - \exp(-NTU) \qquad \text{Eq. (4.8)}$$

$$C_r \equiv C_{min}/C_{max} \qquad \text{Eq. (4.9)}$$

$$NTU \equiv UA/C_{min} \qquad \text{Eq. (4.10)}$$

Where, the UA is the overall heat transfer coefficient consist of thermal resistances of the refrigerant-side, heat exchanger wall side, and air-side. The Nusselt number of the refrigerant is obtained depends on the refrigerant phase (single-phase or two-phase) and type of heat transfer (condensation or evaporation).

4.2.3.1. Condensation

For the condensation, the heat exchanger model is obtained by the following equations. In the case of the single-phase, the Nusselt number of the refrigerant is determined using Dittus-Boelter correlation [118] at low Reynolds number condition ($\mathrm{Re} < 3 \cdot 10^3$) by **Eq. (4.11)** and Gnielinski correlation [84] at the other Reynolds number by **Eq. (4.12)**.

$$\mathrm{Nu}_r = 0.023 \cdot \mathrm{Re}_r^{0.8} \cdot \mathrm{Pr}_r^{0.3} \qquad \text{Eq. (4.11)}$$

$$\mathrm{Nu}_r = \left[\frac{f}{8} \cdot (\mathrm{Re}_r - 1000)\mathrm{Pr}_r\right] / \left[1 + 12.7(f/8)^{0.5}\left(\mathrm{Pr}_r{}^{2/3} - 1\right)\right] \qquad \text{Eq. (4.12)}$$

Where, f is friction factor. In contrast, the Nusselt number of the two-phase refrigerant is obtained using Koyama correlation [119], **Eq. (4.13)**, which is consisted of the forced convection condensation term (Nu_F) and gravity controlled convection condensation term (Nu_B).

$$\mathrm{Nu}_r = \sqrt{(\mathrm{Nu}_F)^2 + (\mathrm{Nu}_B)^2} \qquad \text{Eq. (4.13)}$$

$$\mathrm{Nu}_{r,F} = 0.0112\mathrm{Pr}_{r,L}^{1.37}(\Phi_V/X_{tt})\mathrm{Re}_{r,L}^{0.7} \qquad \text{Eq. (4.14)}$$

$$\mathrm{Nu}_{r,B} = 0.725(1 - \exp(-0.85\mathrm{Bn}^{0.5}))H(\xi)\left(\mathrm{Ga}_{r,L}\mathrm{Pr}_{r,L}\mathrm{Ph}_{r,L}^{-1}\right)^{0.25} \qquad \text{Eq. (4.15)}$$

$$H(\xi) = \xi + [10(1-\xi)^{0.1} - 8.9] \cdot \sqrt{\xi} \cdot \left(1 - \sqrt{\xi}\right) \qquad \text{Eq. (4.16)}$$

$$\xi = \left[1 + \frac{\rho_V}{\rho_L}\left(\frac{1-x}{x}\right)\left(0.4 + 0.6\sqrt{\frac{\frac{\rho_V}{\rho_L} + 0.4\frac{1-x}{x}}{1 + 0.4\frac{1-x}{x}}}\right)\right]^{-1} \qquad \text{Eq. (4.17)}$$

Where, the subscript 'L' and 'V' mean that the liquid phase and vapor phase, respectively. In **Eq. (4.16)** and **Eq. (4.17)**, the function of void fraction ($H(\xi)$) and the void fraction (ξ) are determined by the Smith correlation [120]. To obtain the Nu_F, the turbulent-turbulent Lockhart-Martinelli parameter (X_{tt}) and the two-phase multiplier (Φ) are introduced as presented **Eq. (4.18)** and **Eq. (4.27)**. The Galileo number (Ga), Bond number (Bn), and Phase change number (Ph) are defined **Eq. (4.20)** to **Eq. (4.22)**.

$$X_{tt} = \left(\frac{1-x}{x}\right)^{0.9}\left(\frac{\rho_V}{\rho_L}\right)^{0.5}\left(\frac{\mu_L}{\mu_V}\right)^{0.1} \qquad \text{Eq. (4.18)}$$

$$\Phi_V^2 = 1 + 13.17(\nu_L/\nu_V)^{0.17}(1-\exp(-0.6\mathrm{Bn}^{0.5}))X_{tt} + X_{tt}^2 \qquad \text{Eq. (4.19)}$$

$$\mathrm{Ga}_L = \frac{g\rho_L^3 d^3}{\mu_L^2} \qquad \text{Eq. (4.20)}$$

$$\mathrm{Bn} = \frac{g(\rho_L - \rho_V)d^2}{\sigma} \qquad \text{Eq. (4.21)}$$

$$\mathrm{Ph}_L = \frac{c_{p_L}(T_r - T_{wall})}{\Delta h_{VL}} \qquad \text{Eq. (4.22)}$$

The heat transfer coefficient of the air-side is calculated by the Colburn j factor for a micro-louvered fin heat exchanger which is suggested by Kim and Bullard [121] as shown in **Eq. (4.23)** and **Eq. (4.24)**.

$$h_a^H = j_a \rho_a V_{a,max} c_{p,a} \mathrm{Pr}_\mathrm{a}^{-2/3} \qquad \text{Eq. (4.23)}$$

$$j_a = \mathrm{Re}_a^{-0.487} \cdot \left(\frac{\theta_l}{90}\right)^{0.257} \cdot \left(\frac{L_{f,p}}{L_{l,p}}\right)^{-0.13} \cdot \left(\frac{L_{f,h}}{L_{l,p}}\right)^{-0.29} \cdot \left(\frac{L_{t,d}}{L_{l,p}}\right)^{-0.235} \cdot \left(\frac{L_{l,l}}{L_{l,p}}\right)^{0.68} \cdot \left(\frac{L_{t,p}}{L_{l,p}}\right)^{-0.279} \cdot \left(\frac{\delta_f}{L_{l,p}}\right)^{-0.05} \quad \text{Eq. (4.24)}$$

4.2.3.2. Evaporation

For the evaporation, the heat exchanger model is able to determine using similar with the model of condensation except for the heat transfer coefficient. In the case of the heat transfer coefficient of the single-phase, the heat transfer coefficient used the Dittus-Boelter correlation [118] and Gnielinski correlation [84] according to the Reynolds number. To calculate the heat transfer coefficient of the two-phase, the Sun and Mishima correlation [122] is applied in the heat exchanger model like **Eq. (4.25)**.

$$h_r^H = \frac{6\mathrm{Re}_{Lo}^{1.05}\mathrm{Bg}^{0.54}}{\mathrm{We}_L^{0.191}(\rho_L/\rho_V)^{0.142}} \frac{k_L}{d_h} \quad \text{Eq. (4.25)}$$

$$\mathrm{Bg} \equiv \frac{q}{G\Delta h_{LV}} \quad \text{Eq. (4.26)}$$

$$\mathrm{We}_L \equiv \frac{G^2 d_h}{\sigma \rho_L} \quad \text{Eq. (4.27)}$$

where, the boiling number (Bg) and Weber number (We) are defined by **Eq. (4.26)** and **Eq. (4.27)**, respectively.

4.2.3.3. Investigation of the segment sensitivity

As aforementioned, the thermodynamics properties of heat exchangers are calculated by divided discrete small elements. To verify the model of heat exchangers according to the size of the discrete elements, the sensitivity to the number of segments is investigated by changing the number of segments from 10 to 100,000 under a typical condition. Owing to comparison investigation, the reference point is obtained at the segments as 100,000 per tube in a heat exchanger. Based on the reference point, the relative error is calculated as shown in **Figure 4.4**. As a result, the number of the segments per tube is selected as the 100 that it is calculated below 0.1% error of the IDCOND and 0.001% of the ODHX, respectively.

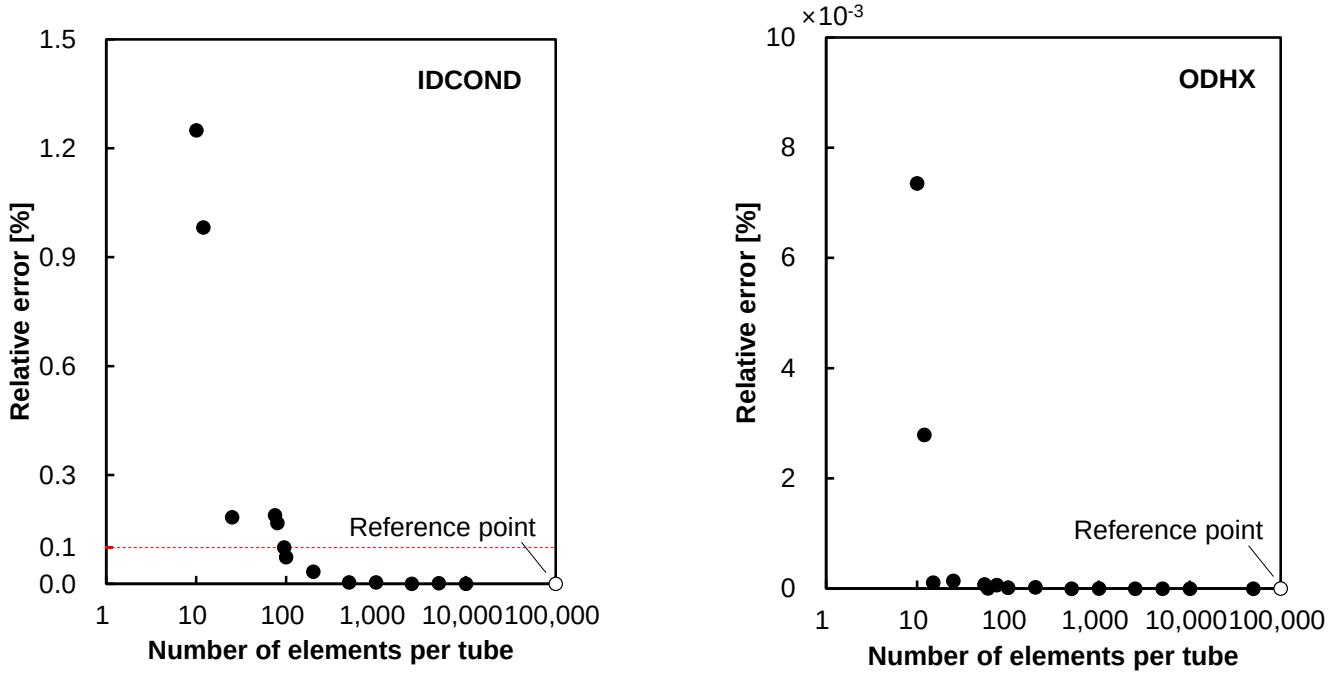

(a) (b)

Figure 4.4 The relative error is calculated based on the reference value at the 100,000 segments per tube by varying the number of segments; (a) IDCOND, (b) ODHX.

4.2.4. Expansion device

With regard to a heat pump system, the expansion device performs the function [123]; separate the two different pressure regions by blocking the refrigerant flow, control the mass flow rate of refrigerant, protect the compressor from wet compression by securing the proper degree of superheat (DSH).

Since the Joule-Thomson coefficient (μ_{JT}) — is defined as **Eq. (4.28)** — of the considered refrigerants are negative at the system operating temperature and pressure region, the refrigerant temperature going down when the pressure of the liquid phase refrigerant rapidly drops through the small diameter orifice of an expansion device by the Joule-Thomson effect.

$$\mu_{JT} \equiv \left(\frac{dT}{dP}\right)_{i=const.} \qquad \text{Eq. (4.28)}$$

The throttling process is usually postulated as isenthalpic on the well-insulated application because no mechanical work and no heat exchanged with the environment. Thus, the enthalpy change of a refrigerant during expansion is negligible in this study.

4.3. Experiment of the automobile heat pump

4.3.1. Experimental apparatus

The numerical model of the heat pump system should be validated with the experimental data. As shown in **Figure 4.5**, an apparatus sat up that composited with two air chambers to maintain the air conditions. Between two chambers, the heat pump apparatus is located as illustrated in **Figure 4.6**. The heat pump system should be released heat to the cabin indoor and absorbed heat from the outdoor. Thus, there are two chambers to make indoor and outdoor conditions.

The information on the air mass flow is necessary for energy analysis in this study. To obtain the air mass flow rate, the two methods were applied in the experiment facility. In the indoor unit, the nozzle flow meter was utilized in the duct. The pressure drop has occurred when the air is passing through the nozzle [93]. Using the measured difference of air pressure between the inlet- and outlet of the nozzle, the air mass flow rate was calculated using the Bernoulli equation. In the outdoor unit, the multiple pitot traverse was used. From the pitot tube, the air velocity and mass flux are able to obtain by measuring the differential pressure of the air. To make uniform the air velocity profile and temperature glide, the flow straighteners were applied in the air duct [124]. The air mass flow rates were controlled by changing the electric current frequency which impressed into the suction type of air fans.

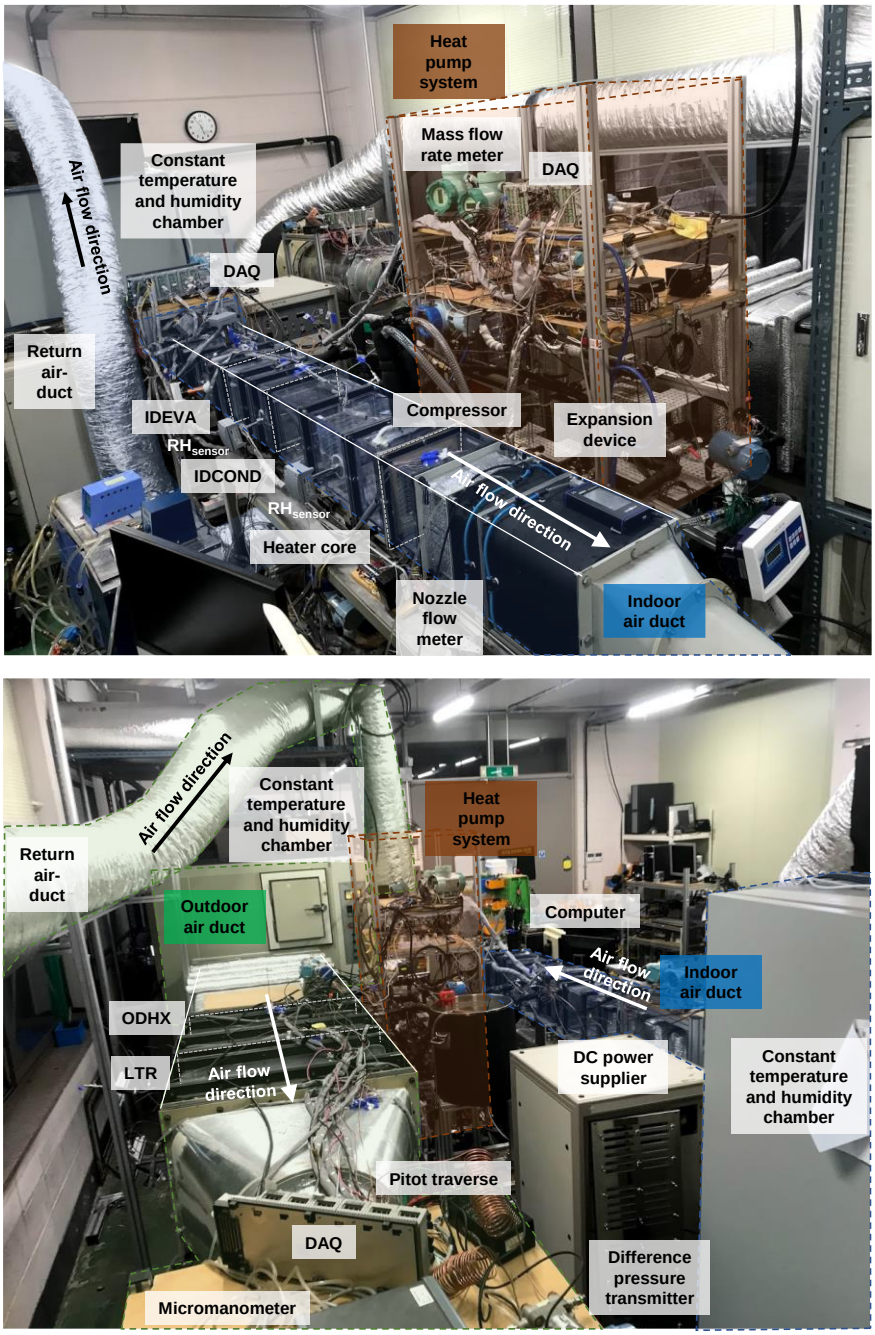

Figure 4.5 Experimental apparatus; (a) indoor side, (b) outdoor side.

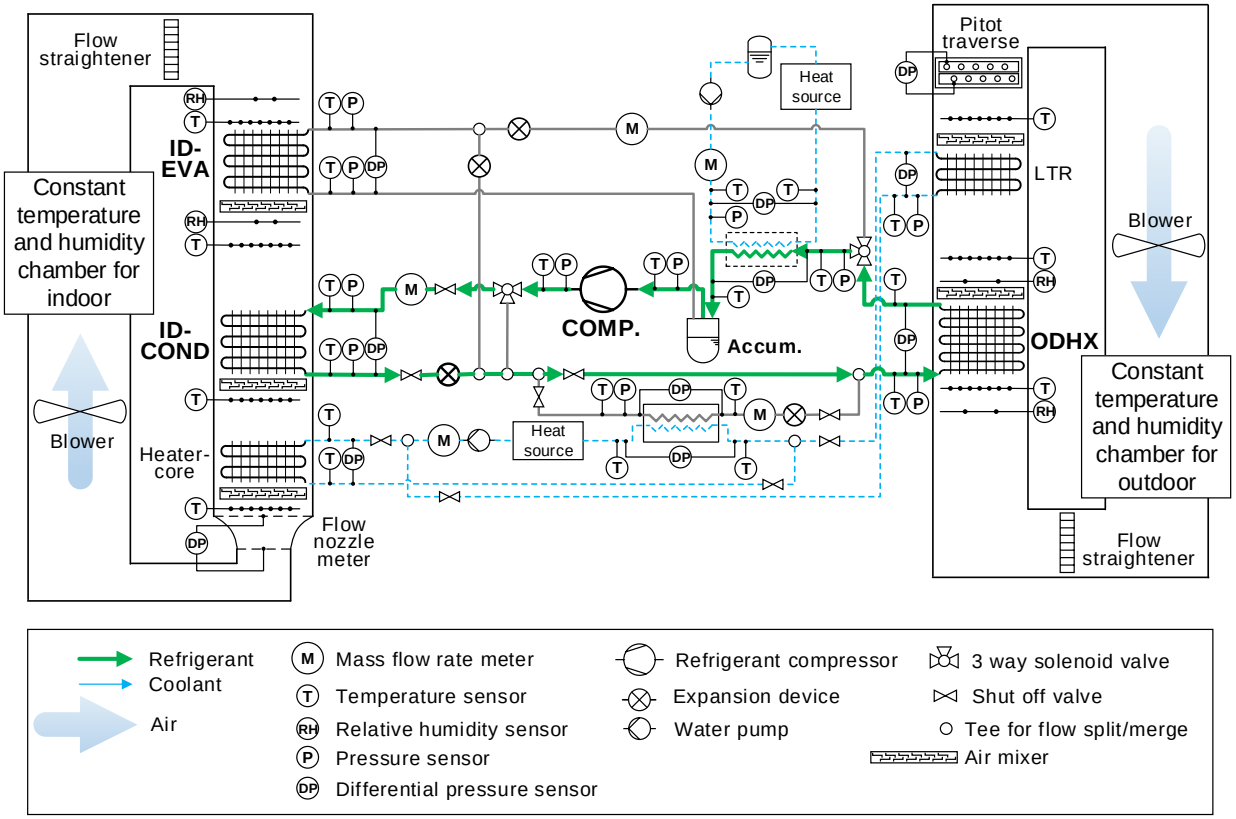

Figure 4.6 Schematic diagram of the experimental facility.

Table 4.3 Specification of the MHP experimental apparatus.

Device / Sensor	Accuracy	Specification	Manufacturer / Model
Data acquisition	DC voltage: ±0.05% of rdg+5 digits Thermocouple: ±0.05% of rdg+0.5℃	-	Yokogawa / DA100
Thermocouples	±0.7℃	−250~350℃	Omega / T-type
Pressure transmitter	±0.5% F.S.	0.1~4.0 MPa	TIVAL / TST-10
Differential pressure transmitter (refrigerant)	±0.04%	0~400 kPa	Druck / STX2100
Differential pressure transmitter (indoor air duct)	±1.0% F.S.	0~689.5 kPa	SETRA / model 264
Micromanometer (outdoor air duct)	±0.25% F.S.	0.01~9999.99 Pa	FURNESS controls / FCO510
Relative humidity transmitter	±0.1℃ ±2.5% RH	−20~80℃, 0~100% RH	VAISALA / HMD60Y
Mass flow meter	±0.1% F.S.	0~100 g/s	OVAL / CX006
Power meter	±0.1% F.S.	0~600 V, 0~20 A	Yokogawa / WT230

Table 4.4 Specification of the heat pump system.

Component	Type	Specification
Compressor	Scroll-type	Discharge: 33 cm^3/rev Revolution Speed: 1000~8000 rpm Power source: DC 380 V
ODHX	Aluminum, Louvered fin, Compact heat exchanger with multiport mini-channel tubes	573 (W) x 345 (H) x 20 (D) mm^3
IDCOND		216 (W) x 160 (H) x 20 (D) mm^3
IDEVAP		256 (W) x 215 (H) x 45 (D) mm^3
Expansion valve	Needle type	Max. revolution: 20 turns Max. flow area: 1.95 mm^2

The heat pump is composited with components such as a compressor, heat exchanger, and expansion valves. The detailed information of the components is summarized in **Table 4.4**. The scroll compressor has a 33 cc displacement volume [cm^3/rev] and the revolution speed was controlled by the controller area network (CAN) communication device. For lubricating and protecting the compressor, the 150g of the polyol ester oil which has a viscosity grade is 100 (POE VG 100) was additionally charged by considering the longer the pipeline of the experimental apparatus than the commercial mobile heat pump system. When insufficient oil charge amount, the scroll may be worn and damaged by friction like **Figure 4.7**. The direct current (DC) power supplier has converted the alternative current (AC) to DC for supplying the 380 V DC to the compressor.

In the traditional internal combustion vehicles, heat exchangers are divided into 2 groups: (1) those which heat transfer with the refrigerant, (2) those which involve the coolant. The latter heat exchanger has a role to release the waste heat of the engine. For instance, the heater-core in the indoor unit and the radiator in the outside unit are classified. But it is out of the research scope of this study. Thus, only the heat exchanger which is related to a refrigerant was considered in this study such as the indoor condenser (IDCOND), the indoor evaporator (IDEVA), and the outdoor heat exchanger (ODHX).

(a) (b)

Figure 4.7 The parts of the scroll compressor; (a) the damaged orbiting scroll (left) and the static scroll (right), (b) the detailed view of failure static scroll.

The expansion valve is replaced by a needle valve to determine the opening area by controlling. To determine the open area of the expansion valve, a needle valve is applied in the system instead of a thermostatic expansion valve (TEV) or an electric expansion valve (EEV). A common TEV has an oscillatory behavior, also known as the hunting, when adjusting the valve because it is caused by hysteresis in the valve due to friction or stiction which is overwhelmed by the evaporating pressure and the spring force [125]. Since the TEV is passively operated by pressure balance between the evaporating pressure of the refrigerant, the pressure of the sensor bulb, and spring force, the non-linear behavior of it might unavoidable. In the case of an EEV, it provides automatic control by utilizing its own controller with the stepping motor and digital linear actuators. However, an EEV also exhibits a hysteresis after using a long time period or oversized design [126]. Meanwhile, the metering valve is able to fine control since the number of handwheel turns is directly correlated to the valve flow coefficient (Cv) without a hysteresis unless the operating pressure, as shown in **Figure 4.8**.

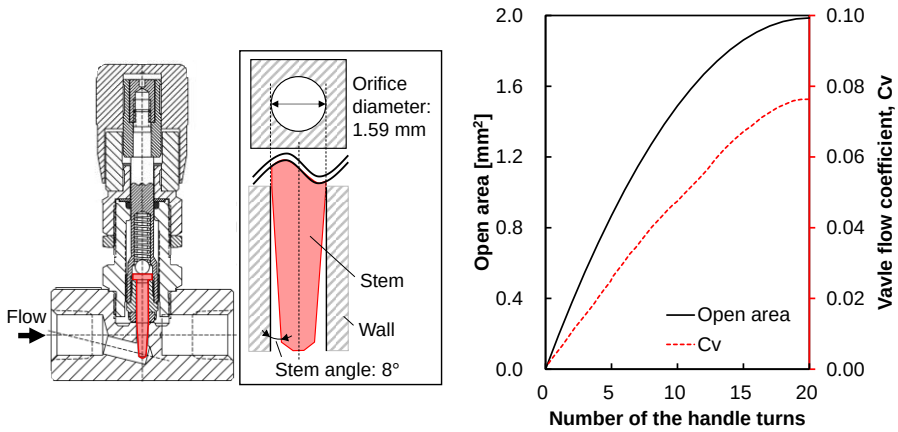

(a) (b)

Figure 4.8 The expansion device; (a) schematic diagram, (b) open area and valve flow coefficient (Cv) according to the number of the handle turns.

4.3.2. Data reduction and uncertainty analysis

The figures of merit in the heat pump system are heating capacity and coefficient of performance (COP). The heating capacity is obtained by enthalpy difference of the air-side as shown in **Eq. (4.29)**. The heating COP is given by **Eq. (4.30)**, which is the ratio of the heating capacity and power consumption of the compressor.

$$\dot{Q}_{air,\mathrm{IDCOND}} = \dot{m}_{air}\rho_{air}c_{p,air}\left(T_{air,out} - T_{air,in}\right)\Big|_{\mathrm{IDCOND}} \qquad \text{Eq. (4.29)}$$

$$COP_H \equiv \dot{Q}_{air,IDCOND}/\dot{W}_{COMP} \qquad \text{Eq. (4.30)}$$

The system was stabilized for at least 10 min and the data of it is acquired by around 6 s interval. The data reduction is conducted using obtained data during a steady state. The steady-state is considered empirically that the COP standard deviation of 100 time-series data (~10 min) is smaller than 0.015.

According to the ASHRAE guideline [95], the uncertainty of the COP should not be greater than 10%. The power consumption of the compressor is measured by the power meter directly. Thus, the uncertainty of the compressor work is simply obtained by **Eq. (3.53)**. Meanwhile, the heating capacity is a function of the temperature, mass flow rate, heat capacity, and density. Thus, the amount of heating has to be considered the error propagation. The overall uncertainty of the COP is obtained by **Eq. (4.31)**. The fixed error and random

error of the COP are calculated by the first-order expansion of the Taylor series as shown in **Eq. (4.32)** and **Eq. (4.33)**.

$$\delta_{COP}^{U} = \sqrt{(\delta_{COP}^{F})^2 + (t^f \cdot \delta_{COP}^{R})^2} \qquad \text{Eq. (4.31)}$$

$$\delta_{COP}^{F} = \sqrt{\sum_{i=1}^{n} \left(\frac{\partial COP}{\partial x_i} \, \delta_{x_i}^{F} \right)^2} \qquad \text{Eq. (4.32)}$$

$$\delta_{COP}^{R} = \sqrt{\sum_{i=1}^{n} \left(\frac{\partial COP}{\partial x_i} \, \delta_{x_i}^{R} \right)^2} \qquad \text{Eq. (4.33)}$$

Owing to simplicity, the density and the heat capacity of the air are neglected since its standard variation is too small to affect the overall uncertainty of the COP. Thus, the fractional uncertainty of the COP is derived as shown in **Eq. (4.34)**. The error propagation equation of the temperature difference is given in **Eq. (4.35)**.

$$\frac{\delta_{COP}^{U}}{COP} \cong \sqrt{\left(\frac{\delta_{\dot{m}_{air}}^{U}}{\dot{m}_{air}}\right)^2 + \left(\frac{\delta_{\Delta T}^{U}}{\Delta T}\right)^2 + \left(\frac{\delta_{\dot{W}_{COMP}}^{U}}{\dot{W}_{COMP}}\right)^2} \qquad \text{Eq. (4.34)}$$

$$\delta_{\Delta T}^{U} = \sqrt{\left(\delta_{T_{air,out}}^{U}\right)^2 + \left(\delta_{T_{air,in}}^{U}\right)^2} \qquad \text{Eq. (4.35)}$$

As a result of the uncertainty analysis, the error of COP is calculated as 5.6%. This value is about half of the ASHRAE recommended error limit.

Table 4.5 Uncertainty analysis of the heat pump system.

Variables	Fixed error	Random error	Total error
Pressure transducers (at high-pressure line)	0.50%	0.28%	0.74%
Pressure transducers (at low-pressure line)	0.50%	0.14%	0.57%
Differential pressure transducer (outdoor air duct side)	0.25%	0.63%	1.27%
Differential pressure transducer (indoor air duct side)	1.00%	0.11%	1.02%
Thermocouples	0.12%	0.09%	0.21%
Mass flow meters	0.10%	1.56%	3.09%
Power meters	0.20%	0.23%	0.49%
Heating capacity	-	-	5.61%
COP_H	-	-	5.63%

4.3.3. The optimum charge amounts

The performance of refrigeration or heat pump systems strongly depends on the refrigerant charge amounts [116]. To achieve the good performance of the system, it is essential to charge the optimum refrigerant amount and maintain it properly without leakage [117]. To determine the optimum charge amount, the experiment is conducted under the condition that the indoor temperature is 20°C and the outdoor temperature is 7°C. The expansion valve is controlled to achieve the minimum degree of superheating (DSH) is 5°C to prevent the compressor from wet compression. Since the liquid phase of refrigerant during compression, the droplet might damage the compressor [127]. Since the droplet may cause the abrupt pressure rising by evaporating at the cylinder head [128]. And the lubricant effect may decrease, thus the compressor wear may accelerate since the liquid refrigerant washes away the lubricant oil on the wall of the cylinder [129].

The compressor and air blowers were maintained the revolution speed, for instance, the compressor operated at 3,500 rpm. The refrigerant was gradually injected into the service port on the compressor suction pipe. According to the SAE J2765 standard [130], the added refrigerant in increments of no more than 50 g. As a result, the optimum charge amount of the R-134a is

determined around 700 g as shown in **Figure 4.9**. In the case of the R-1234yf, the trend of COP is similar with the R-134a whereas the optimum charge amount of the R-1234yf is around 740 g, as represented in **Figure 4.10**.

The COP stays lower when less charge amount conditions because the heat capacity is insufficient due to the lack of refrigerant mass flow rate. When the excess charge amount condition, the power consumption of the compressor is sharply increased since the condensing pressure and pressure ratio of the compressor are raising. Because the volume of high-pressure pipes is filled by the liquid phase of refrigerant to contain the exceed charged refrigerant. In other words, the remained volume of the vapor phase is reduced. Therefore, the pressure should be increased by Boyle's law.

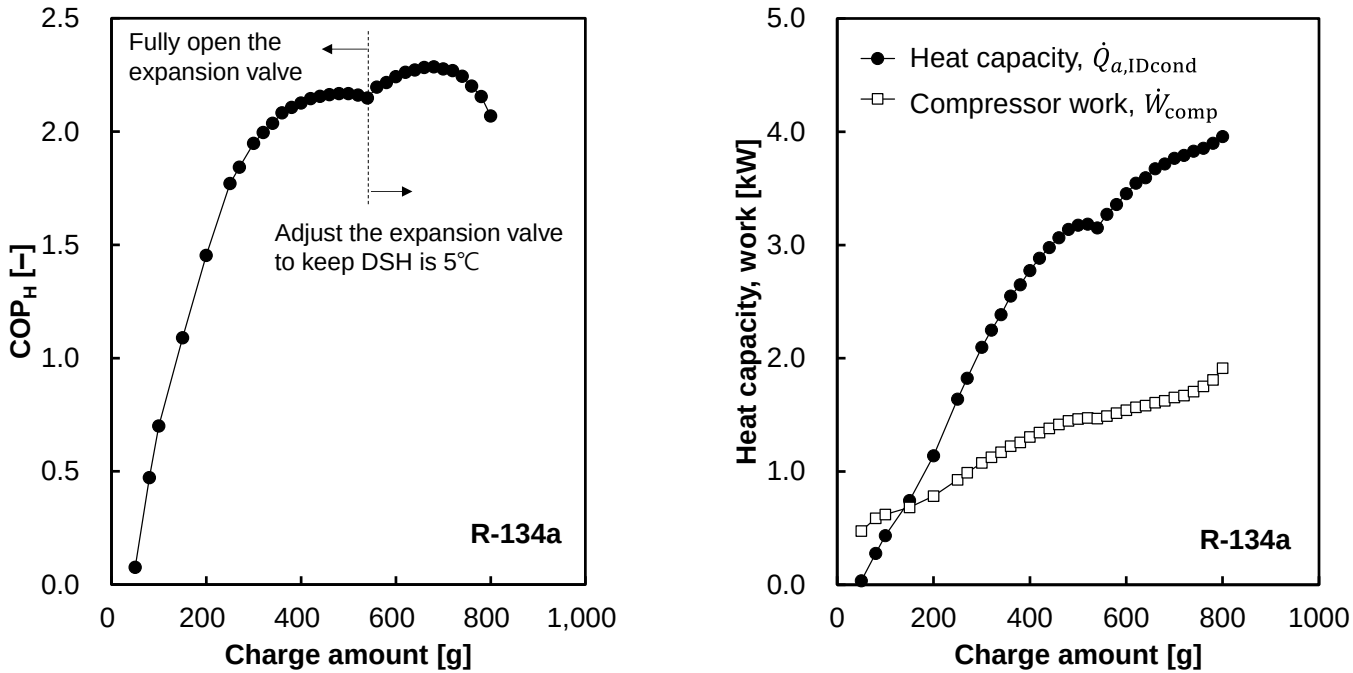

(a) (b)

Figure 4.9 The experimental data to find the optimum charge amount of the R-134a under operation condition that the compressor revolution speed is 3500 rpm and the heat source/sink temperature are 20/7°C; (a) the heating COP, (b) the heat capacity and the work according to the refrigerant charge amount.

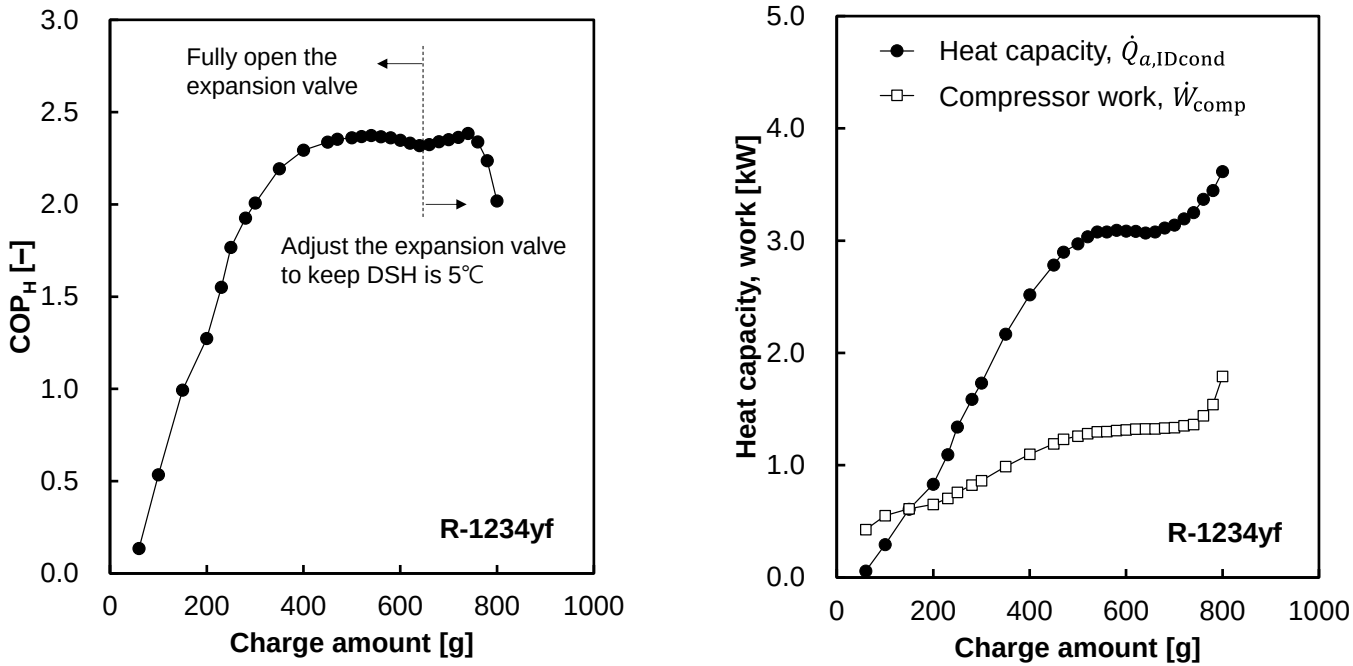

(a) (b)

Figure 4.10 The experimental data according to the charge R-1234yf amount; (a) heating COP, (b) the heat capacity and the work.

4.3.4. Performance of the heat pump system

In order to obtain the performance of the automobile heat pump (MHP) system, the system was charged the optimum amount of refrigerant as described in the previous section. Then, the experiment was conducted on various compressor revolution speeds under the testing conditions which are summarized in **Table 4.6**. The revolution speed of the compressor is able to control by using the inverter controller named CANDy. In this study, the experiment carried out gradually increasing from the minimum revolution speed of the scroll compressor, 1,500 rpm. **Figure 4.11** reveals that the MHP which is charged the R-134a refrigerant performs the better COP at the lowest revolution speed of the compressor. However, the heating capacity is insufficient to raise the cabin air temperature and the interior mass temperature within driving time. Because the mass flow rate of the refrigerant is small when operating low revolution speed according to **Eq. (4.4)**. In contrast, the COP is lowest at the faster revolution speed condition. The energy consumption of the compressor is corresponding the mass flow rate of refrigerant and the revolution speed as following **Eq. (4.4)** and **Eq. (4.5)**. Thus, the energy consumption is linearly increasing as fast as the compressor rotation. But, the heating capacity seems saturated even though the mass flow rate is enlarged.

Because the temperature difference between the refrigerant and the auxiliary fluid going smaller as increasing the mass flow rate of the refrigerant. Since the temperature difference is the driving parameter to heat exchange, the heat capacity might be not infinitely increased. Thereby, the trend of the COP subjected to the compressor revolution speed is displayed as saturation. The trend also appears in the results of the experiments using R-1234yf, instead of R-134a, as shown in **Figure 4.12**.

Table 4.6 Heating capacity rating conditions.

	Indoor side (in the cabin)		**Outdoor side**	
	Dry-bulb / Wet bulb [131] [°C]	**Volume flow rate [m^3/min]**	**Dry-bulb / Wet bulb [132] [°C]**	**Air velocity [m/s]**
Standard heating capacity (SH)	20 / 15	7	7 / 6	4
Low temperature heating capacity (LH)	20 / 15	7	2 / 1	4
Extra low temperature heating capacity (eLH)	20 / 15	7	−7 / −8	4

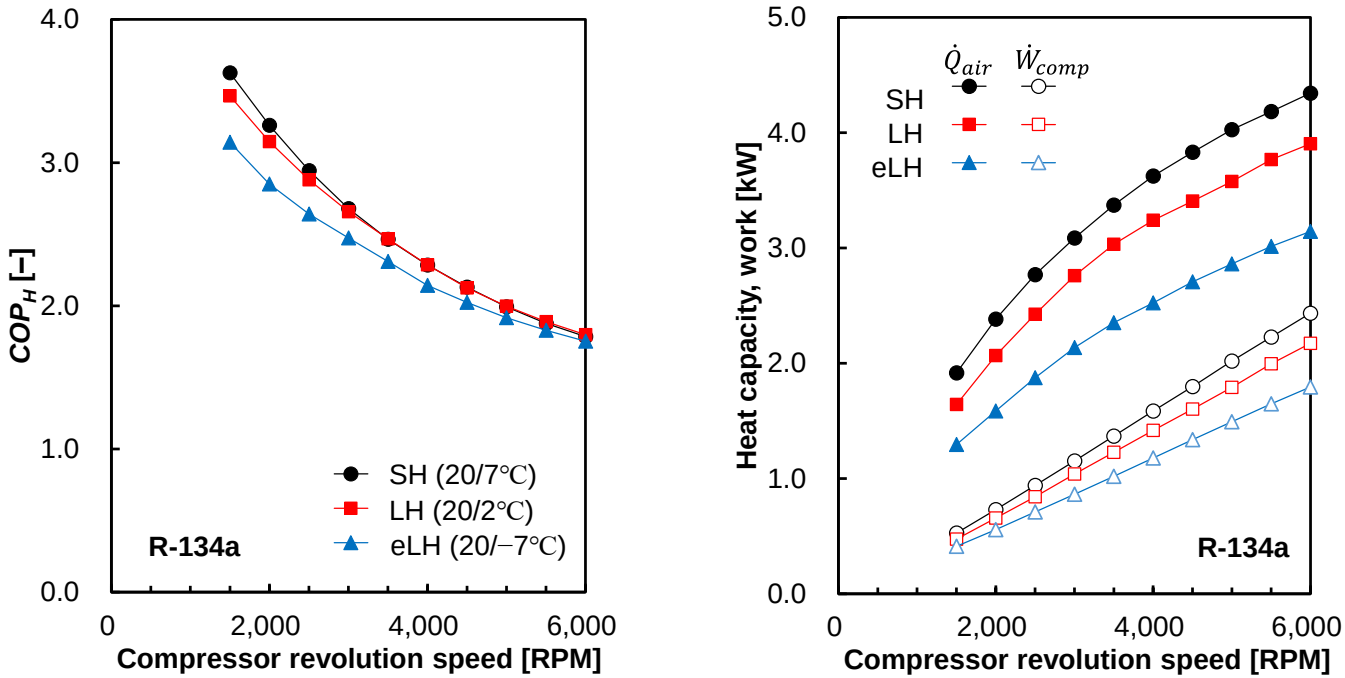

(a) (b)

Figure 4.11 The system performance using R-134a according to the compressor revolution speed and operation temperature; (a) the heating COP, (b) the heating capacity and the compressor work.

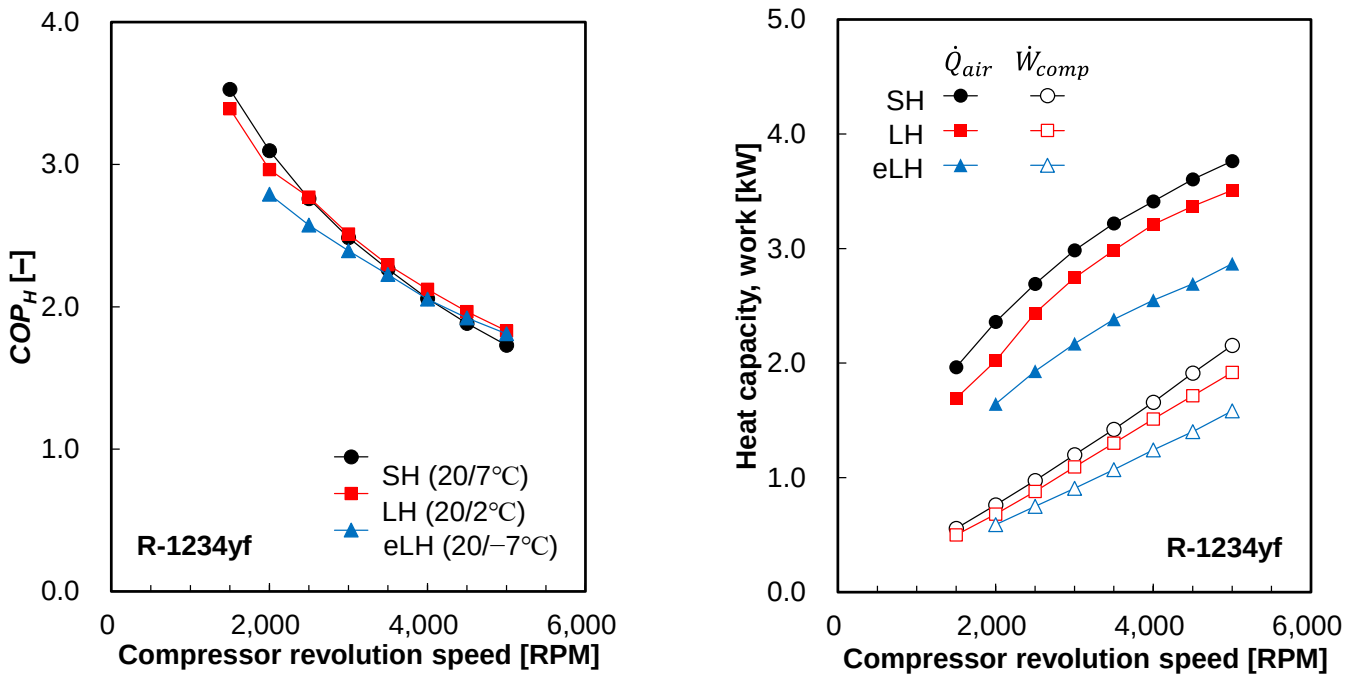

(a) (b)

Figure 4.12 The system performance using R-1234yf according to the compressor revolution speed and operation temperatures; (a) the heating COP, (b) the heating capacity and the compressor work.

4.3.5. Validation of the heat pump model

To validate the developed numerical model of the automobile heat pump (MHP), the comparison is conducted as shown in **Figure 4.13**. At the low charge amount region, it is large that the difference between experimental data and simulation results. Because the simulation result is obtained by constraining the degree of superheating (DSH) as 5°C. Meanwhile, the experiment is not maintained even though the expansion valve was fully opened. Practically, the installed expansion valves are not able to expand the orifice area infinitely. The limitation might lead to the difference between experimental data and simulation results in the low charge amount region.

As mentioned in **Section 4.3.3.**, the optimum charge amounts exist in a closed-loop cycle. At the low charge amount region, the heating capacity is not sufficient due to the small refrigerant mass flow rate. At this condition, some of the refrigerants remain vapor phase. It leads to decreasing sharply the mass flux at the expansion valve because the density of the vapor phase is much larger than its liquid phase. Meanwhile, the condensing pressure increase when the refrigerant charge is exceeded. Since the volume of the high-pressure is filled by liquid refrigerant and the remaining volume for the vapor phase is reduced. Thereby, the pressure of the vapor phase should be increased. It leads to elevates

the pressure ratio and degrades the efficiency of the system as shown in **Figure 4.14**. In practice, a liquid receive-tank is usually utilized in a system for solving the COP degradation problem when inject the exceed charge amount. Even though, the receive-tank is not considered in this study to observe the effect of the charge amount clearly.

At the system that shows the maximum coefficient of performance (COP), the optimum charge amount is obtained. Using the optimum charge amount, the charge amount is normalized regardless of the volume of the system to figure out the maximum COP. When charging the optimum charge amount in a system, the degree of the subcooling (DSC) is nearly 0.

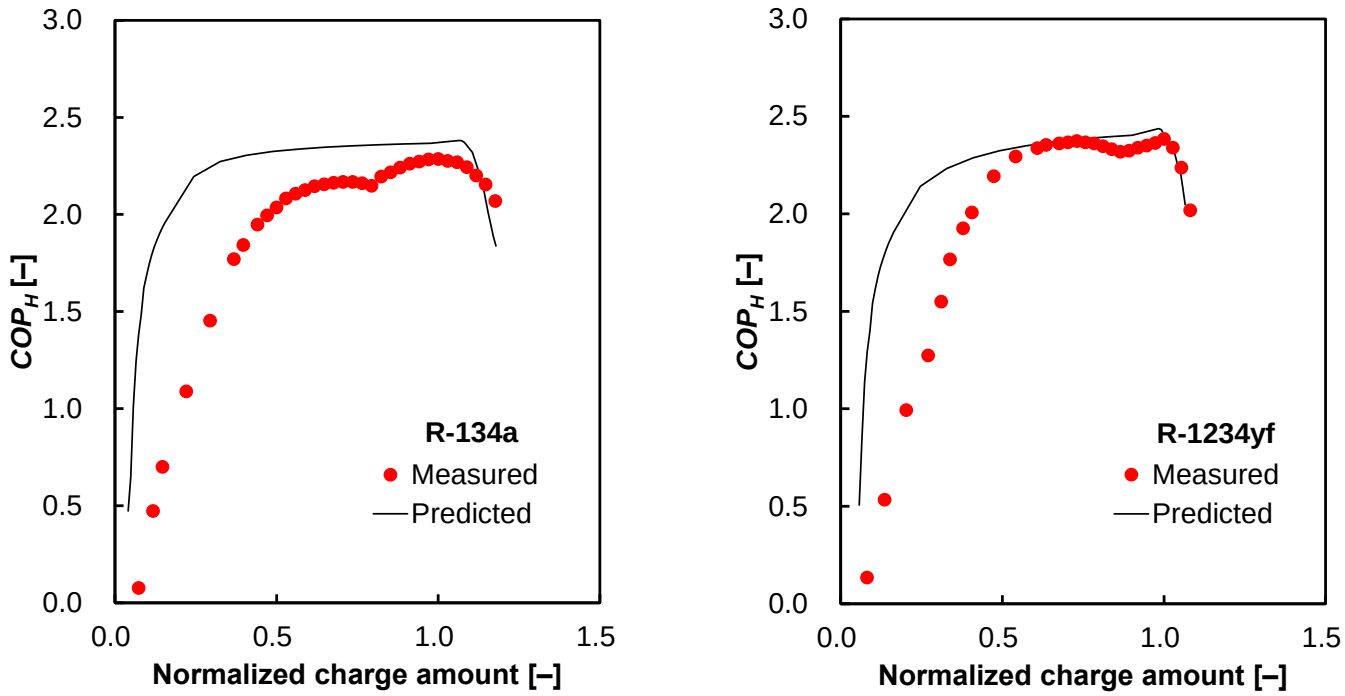

(a) (b)

Figure 4.13 Comparison between experimental data and simulation result according to the charge amount; (a) R-134a, and (b) R-1234yf.

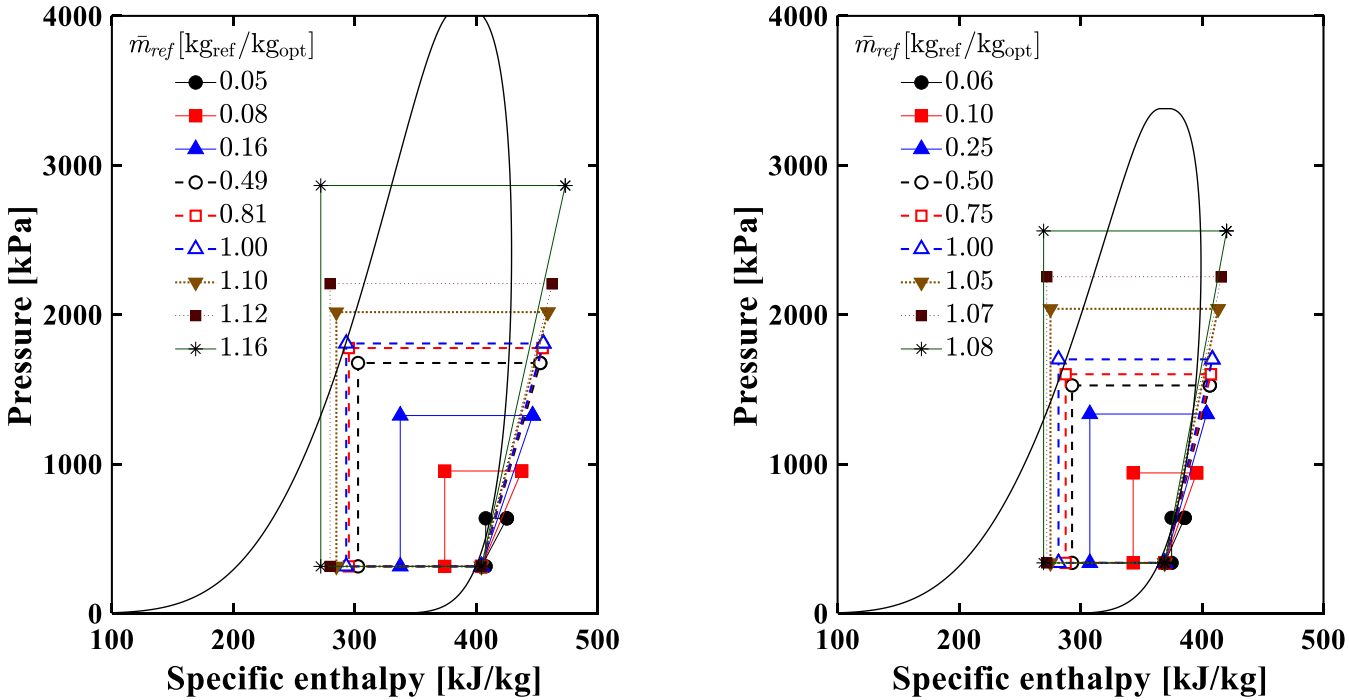

(a) (b)

Figure 4.14 The simulation results are plotted on the *P-h* diagram according to the normalized charge amount ($\bar{m}_{ref}$); (a) R-134a, and (b) R-1234yf.

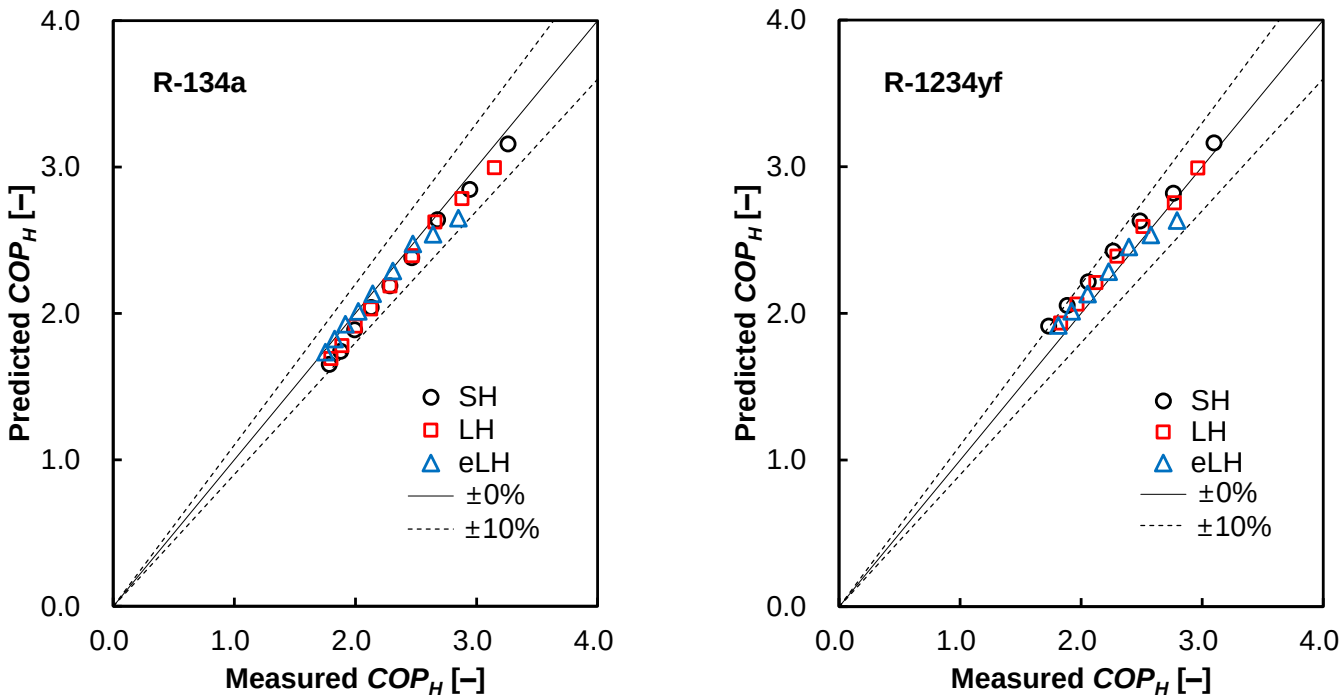

(a) (b)

Figure 4.15 Comparison between experimental data and simulation result; (a) R-134a, (b) R-1234yf.

The root mean squared error ($RMSE_{COP}$) and the root mean squared relative error ($RMSRE_{COP}$) of the COP are calculated in each case as following the Eq. (4.36) and Eq. (4.37), respectively.

$$RMSE_{COP} = \sqrt{\frac{1}{n}\sum_{i=1}^{n}\left(COP_{H,exp} - COP_{H,sim}\right)^2} \quad \text{Eq. (4.36)}$$

$$RMSRE_{COP} = \sqrt{\frac{1}{n}\sum_{i=1}^{n}\left(\frac{COP_{H,exp} - COP_{H,sim}}{COP_{H,exp}}\right)^2} \times 100\% \quad \text{Eq. (4.37)}$$

In the case of R-134a, $RMSE_{COP}$ and $RMSRE_{COP}$ are 0.092 and 4.02%, respectively. Meanwhile, $RMSE_{COP}$ and $RMSRE_{COP}$ of the R-1234yf are 0.109 and 4.86%.

4.4. Summary

In Chapter 4, the automobile heat pump (MHP) model was constructed to estimate the coefficient of performance and the energy consumption of the MHP. The performance of the closed-loop cycle strongly corresponds to the thermodynamic and physical properties of a refrigerant. The conventional refrigerant, R-134a, must phase out due to its high global warming potential (GWP). Thus, alternative refrigerants were considered by thermodynamic analysis. And the proper lubricant was also discussed to match up with the low

GWP refrigerant in the first section. In the second section, the numerical model of the MHP was developed. The MHP is composited with a compressor, an expansion device, and heat exchangers. Since the compressor is a crucial component, critical characteristics such as isentropic efficiency, volumetric efficiency, and mechanical efficiency are obtained by preliminary research. Heat exchangers discrete small elements and amounts of the heat transfer are calculated using the effectiveness(ε)-NTU method. The experimental facility was built to measure the performance of the MHP. To figure out the optimum charge amount of the system, the preceding research was progressed. After that, the performance of the MHP was determined according to various operation conditions by changing the refrigerant type. Using the experimental data, the developed MHP model was validated by comparing it with the simulation result. As a result, the predicted performance of the MHP reveals a small error as compared with the experimental data.

Chapter 5. Integrated System Simulation

5.1. Introduction

The conventional EV system has two thermal cycles: a refrigerant cycle for maintaining the air condition of the cabin, and a coolant cycle for releasing heat from the power electronics and electric machinery (PEEM), as shown in **Figure 1.4**. To recover the waste heat of the PEEM, the additional heat exchanger is integrated with the coolant cycle, as illustrated in **Figure 5.1(a)**. Plus, the DCHE is able to replace the plain heat exchanger to simultaneously remove the moisture in the air and perform heat exchange. When dehumidification is needed, the DCHE outlet air is blown into the IDEVA of the MHP. However, as the water vapor is captured into the pores of the desiccant, the adsorption performance of the DCHE decreases. Hence, after a certain period of time passes, a regeneration process is necessary. **Figure 5.1(b)** illustrates that the DCHE recovers the adsorption capacity by heating up using the waste heat of the PEEM. To simplified the simulation, the alternative method is chosen as constant time step, 240 s in this Chapter. In some commercial EVs, a PTC heater is installed to deal with the heating load, but in this study, that is not considered. The developed numerical models were integrated into the Simulink platform as indicated in **Figure 5.2**.

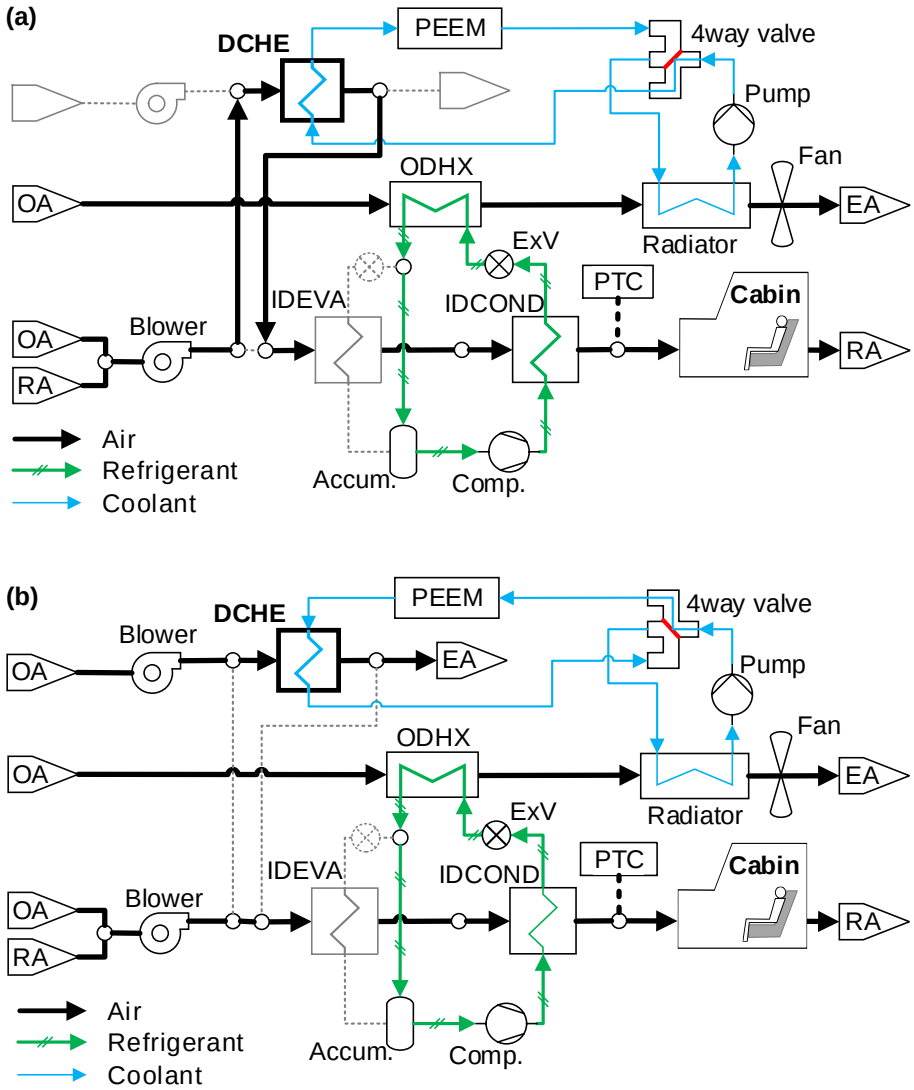

Figure 5.1 Schematic of the automotive heat pump system (MHP) with the desiccant coated heat exchanger (DCHE): (a) Dehumidification mode, and (b) Regeneration mode.

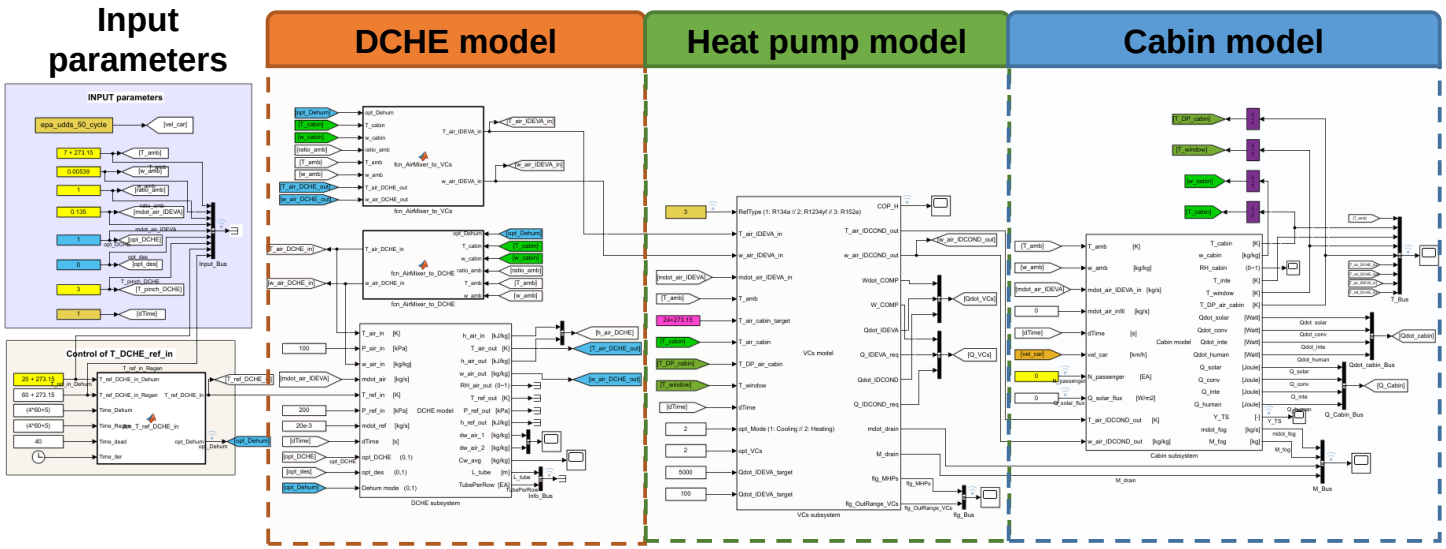

Figure 5.2 Simulink block diagrams of the automotive heat pump system with the desiccant coated heat exchanger to calculate the energy consumption of the electric vehicle.

Before starting the simulation, input parameters were set in the Simulink. According to the given parameters, the calculation is following the procedure as illustrated in **Figure 5.3**. The DCHE model is calculated at first, and then the heat pump model and cabin are calculated as shown in **Figure 5.4(a)** and **(b)**. In the dehumidification mode, the process air through the DCHE and IDCOND. But, in the regeneration mode, the ambient air injects into the DCHE and then exhausts. The heat pump system will be operated for two purposes; heating the space and defogging when the window temperature is lower than the dew point. If the cabin air higher than the target temperature, the heat pump system should be stopped. Otherwise, the heating mode is operated to heating the cabin air. In the heating mode, the indoor evaporator doesn't heat transfer with the process air. The outdoor heat exchanger (ODHX) performs as an evaporator by heat exchanging with the ambient air. Therefore, the temperature of the supplied air going to increase as shown in **Figure 5.5(a)**. On the other hand, when the window temperature is lower than the dew point, the condensing mode should be operated to remove the moisture in the cabin air. In the condensing mode, the refrigerant of the IDCOND outlet injects into the ODHX in a high-pressure region. It means that the ODHX acts like a condenser by heat exchanging with the ambient air. The indoor evaporator (IDEVA) operates as the evaporator to condensing the water moisture in the cabin air. The process air cooldown

through the IDEVA and then heat up by heat transfer in the IDCOND. Because of this process, the temperature of the supply air is not higher than the heating mode. Thus, the increment of the return air to supply air is not so big as indicated in **Figure 5.5(b)**.

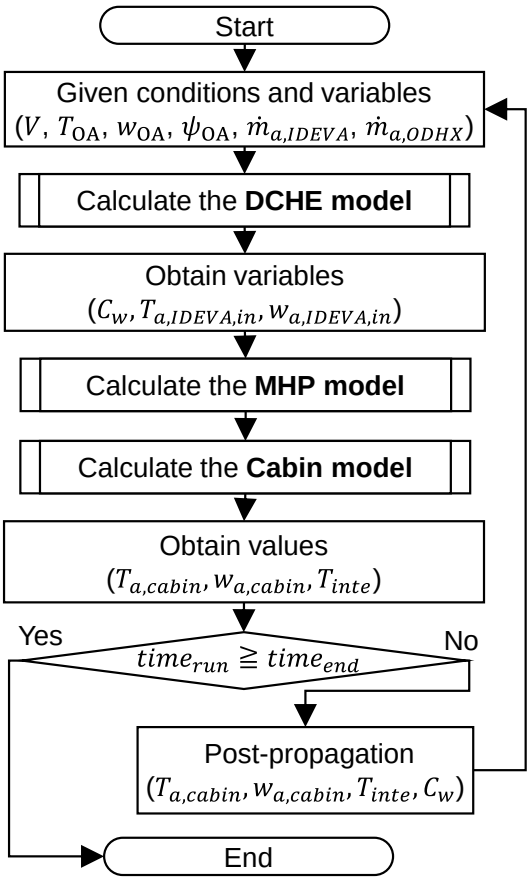

Figure 5.3 Flow chart of the simulation of the procedures of the integration system with the DCHE model, MHP model, and Cabin model.

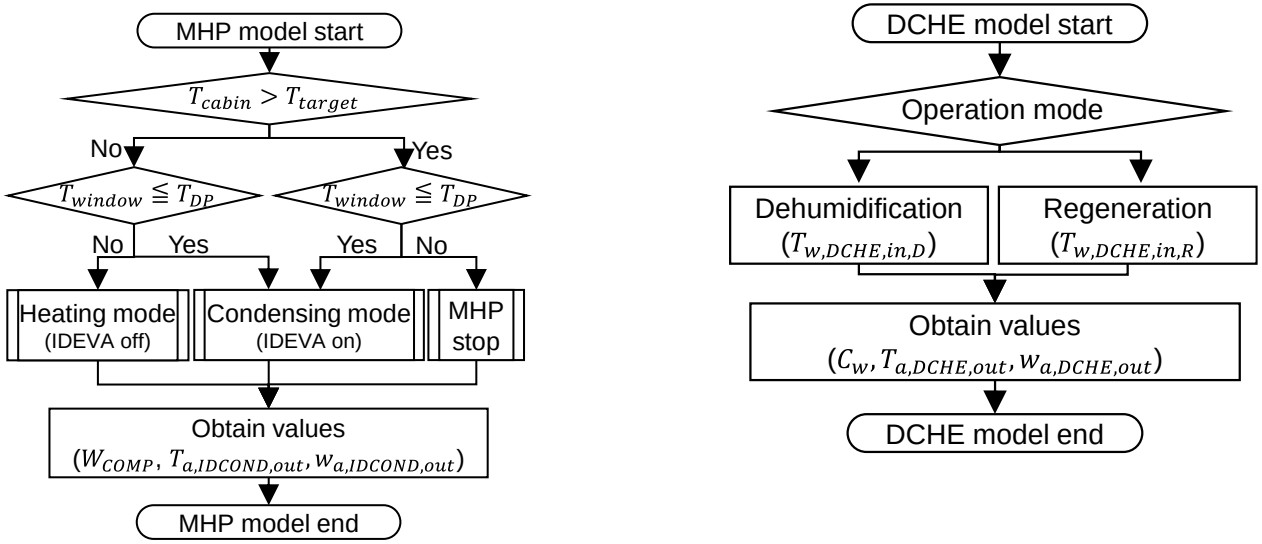

(a) (b)

Figure 5.4 Flow chart of the simulation; (a) the subroutine for the MHP, and (b) the subroutine for the DCHE.

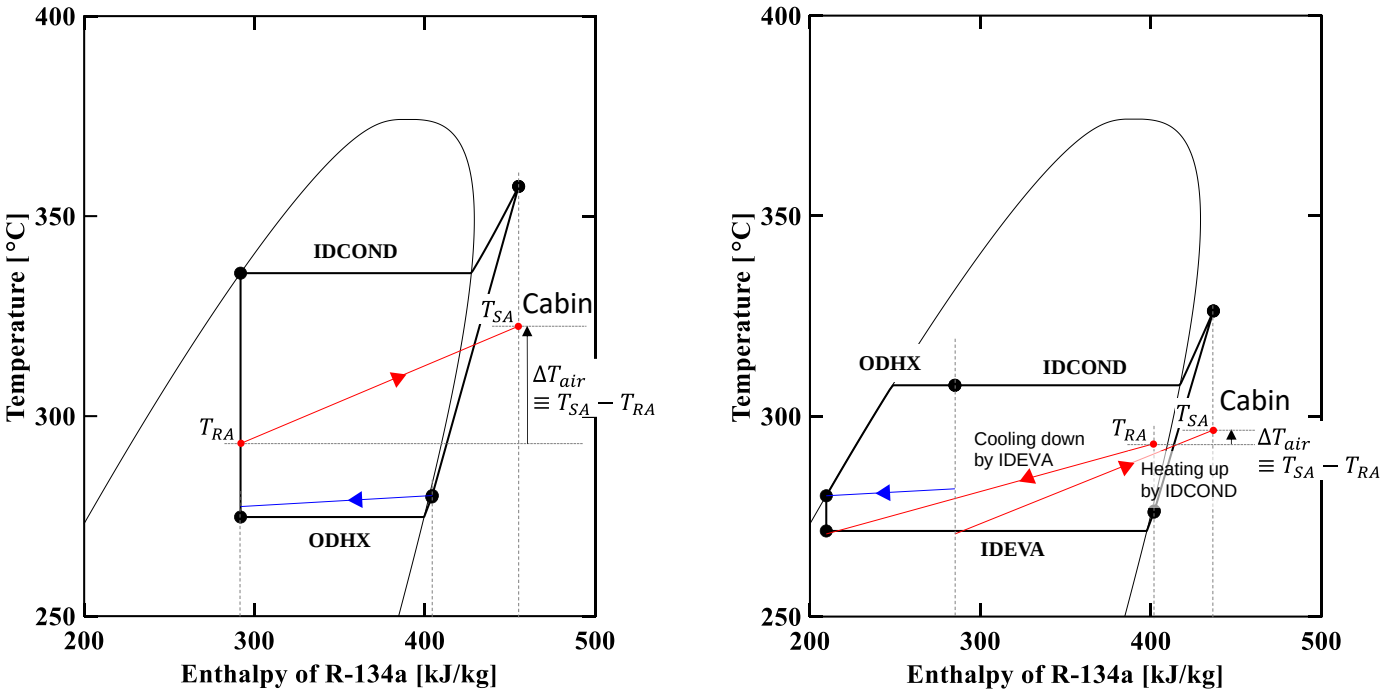

(a) (b)

Figure 5.5 The pressure-enthalpy (*P-h*) diagram; (a) at the heating mode, (b) at the condensing mode.

5.2. Simulation conditions

The window temperature depends on the velocity of the electric vehicle according to **Eq. (2.13)** and **Eq. (2.14)**. The simulation was performed using the urban dynamometer driving schedule (UDDS) driving velocity profile as shown in **Figure 2.7 (c)**, which is the fuel economy testing standard of the US Environmental Protection Agency (EPA). The total operation time was 13,700 s by running 10 cycles of the UDDS velocity profile.

The MHP operates the heating mode to heat up the air through IDCOND, and the system turns off when the cabin air temperature is higher than the target temperature of 24°C. Because the human being feels comfortable at that condition according to the thermal sensation (Y) is around 0 value as defined **Eq. (2.24)**.

When the window temperature is lower than the dew point, the MHP runs the condensing mode to prevent fogging up of the window. The numerical models were assumed to be operated in quasi-steady states. The initial temperature of the cabin air and interior furniture were set at 5°C. The air infiltration rate was neglected under the assumption that the vehicle was adequately sealed. In order to conservatively set for heating, the solar radiation was set to 0 W/m^2, i.e., night-time. The waste heat from PEEM was generated

according to the driving conditions, such as motor torque and rotating speed. But in this study, the PEEM thermal state was simplified, so that the discharge coolant temperatures of the PEEM and the radiator were constant. For instance, the coolant temperature of the outlet PEEM is 60°C. The coolant mass flow rate of the DCHE is maintained as 0.02 kg/s. The air mass flow of the indoor- and outdoor were kept constant at 0.135 kg/s, and 1.0 kg/s, respectively.

5.3. Simulation results

5.3.1. Effect of the additional heat exchanger

To compare the simulation results of the energy consumptions, the result of a configuration without the additional heat exchanger is selected as the baseline [133]. Owing to examine the effect of adding a heat exchanger for heat recovery, a plain heat exchanger is utilized. The plain heat exchanger means that is not coated with desiccant. In the case of the desiccant coated heat exchanger (DCHE), the dehumidification mode and regeneration mode by switching every 4 min. The simulation conditions and results are summarized in **Table 5.1**.

As a result, the absolute humidity in the cabin maintains low states in the case of the DCHE utilized as shown in **Figure 5.6**. It means that the DCHE

removes the moisture properly during the driving time. Thereby, the case of the DCHE obtained an energy saving of about 9%, compared with the baseline. However, the plain heat exchanger seems not effectively reduce the energy usage under the condition. Although the heating mode has the advantage of improving the efficiency by raising the IDEVA inlet temperature through waste heat recovery, the condensing mode has the disadvantage of increasing the energy consumption by making a large enthalpy difference to reach a saturated state, i.e., Δh_{C1} in **Figure 1.5**. Since it cancels out the pros and cons under the conditions that the fresh-recirculation air ratio (ψ_{OA}) is 0, the waste heat recovery would not help to reduce energy consumption. The performance change according to the ψ_{OA} is described later in **Section 5.3.3**. In case of the DCHE, the cabin air temperature quickly reaches the target temperature with dehumidification, while the MHP operating time (t_{tot}) is shortened, thus energy consumption is reduced.

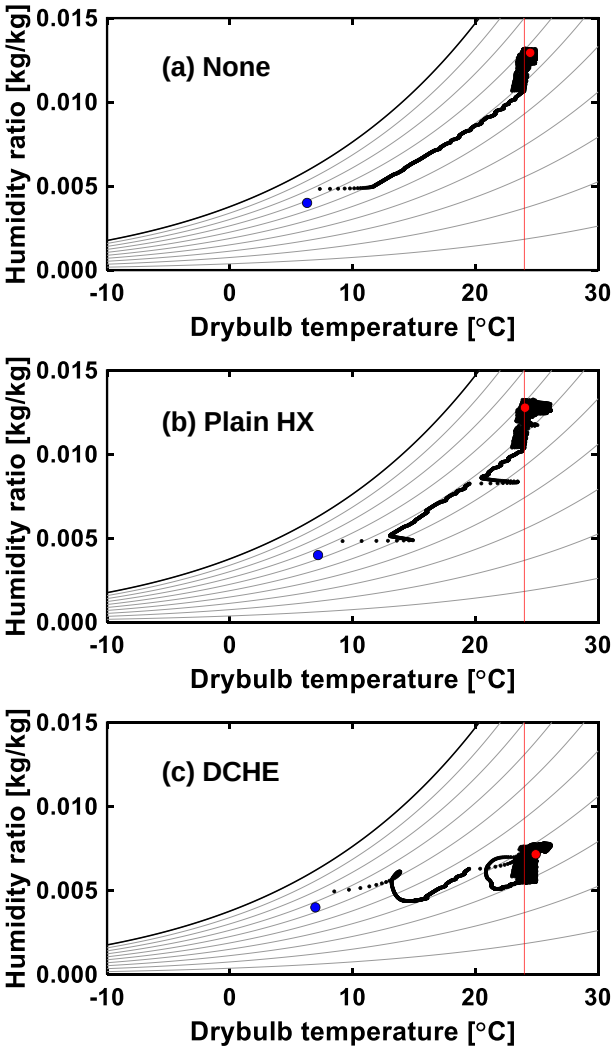

Figure 5.6 Psychrometric charts of the cabin air according to the application of the additional heat exchanger: (a) none, (b), plain heat exchanger, (c) DCHE.

Table 5.1 Simulation conditions and results to examine the effect of the heat exchanger.

Additional HX	T_{OA} [°C]	$T_{OA,WB}$[°C] / w_{OA}[g/kg]	ψ_{OA} [−]	$T_{w,HE,in}$ [°C]	t_{tot} (t_H/t_C) [s]	W_{COMP} [kJ]	Saving ratio [%]
None	7	6 / 5.39	0	20	3700 (3328/372)	6,453	-
Plain HX	7	6 / 5.39	0	20	3767 (3397/370)	6,556	−1.59
DCHE	7	6 / 5.39	0	20	3228 (3228/ 0)	5,851	9.33

5.3.2. Effect of the DCHE frontal area

To investigate the effect of the DCHE frontal area, the simulation was conducted by changing the length and width of the heat exchanger. As shown in **Figure 5.7** and **Table 5.2**, the larger frontal area of DCHE shows better performance as the log regression correlation. To set the proper size of the DCHE, the differential value of the regression equation is considered. In the case of the larger than the 0.3 m^2 of the DCHE, the reduction of the energy consumption tends to saturate. Therefore, the size of the selected DCHE is 0.26 m^2, i.e., the length is 0.50 m and the height is 0.52 m, which is similar to a traditional radiator.

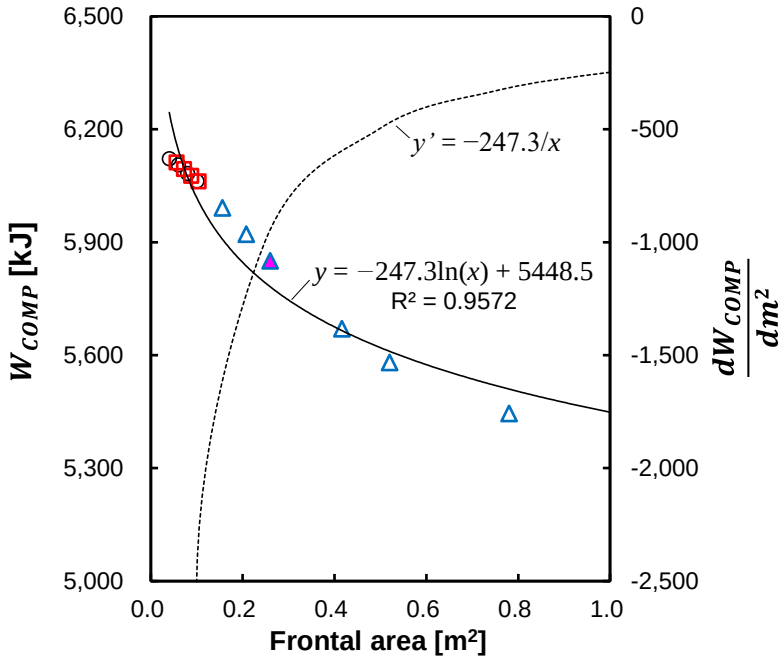

Figure 5.7 Energy consumption according to the size of the desiccant coated heat exchanger.

Table 5.2 Simulation conditions and results according to the size of DCHE.

Additional HX	A_{HX} [m^2]	L_{HX} [m]	Tube per row [EA]	$t_{tot}(t_H/t_C)$ [s]	W_{COMP} [kJ]	Saving ratio [%]
None	-	-	-	3,700 (3,328/372)	6,453	-
DCHE	**0.040**	**0.2**	8	3,384(3,384/ 0)	6,122	5.13
DCHE	**0.060**	**0.3**	8	3,375(3,375/ 0)	6,105	5.39
DCHE	**0.080**	**0.4**	8	3,363(3,363/ 0)	6,083	5.74
DCHE	**0.100**	**0.5**	8	3,351(3,351/ 0)	6,062	6.06
DCHE	**0.056**	0.2	**12**	3,378(3,378/ 0)	6,112	5.29
DCHE	**0.072**	0.2	**16**	3,369(3,369/ 0)	6,094	5.56
DCHE	**0.088**	0.2	**20**	3,359(3,359/ 0)	6,076	5.84
DCHE	**0.104**	0.2	**24**	3,350(3,350/ 0)	6,061	6.07
DCHE	**0.156**	**0.3**	**24**	3,310(3,310/ 0)	5,991	7.16
DCHE	**0.208**	**0.4**	24	3,269(3,269/ 0)	5,921	8.24
DCHE	**0.260**	**0.5**	24	3,228(3,228/ 0)	5,851	9.33
DCHE	**0.416**	**0.8**	24	3,122(3,122/ 0)	5,670	12.14
DCHE	**0.520**	**1.0**	24	3,070(3,070/ 0)	5,580	13.53
DCHE	**0.780**	**1.5**	24	2,992(2,992/ 0)	5,445	15.62
DCHE	**1.040**	**2.0**	24	2,951(2,951/ 0)	5,373	16.74

5.3.3. Effect of the fresh-recirculation air ratio

As a rule of thumb, drivers commonly open a window to circulating the air when fogging up on a windshield. Because the ambient air contains low humidity usually in the winter season. Thus, the average relative humidity rapidly drops when mixing with outdoor air and cabin air. However, it is a disadvantage for heating the cabin air up. Therefore, energy analysis is needed to investigate the effect of the fresh-recirculation air ratio, which is defined as **Eq. (2.15)**. Here, the fresh-recirculation air ratio (ψ_{OA}) is reminded as **Eq. (5.1)**.

$$\psi_{OA} \equiv \frac{\dot{m}_{OA}}{\dot{m}_{SA}} = \frac{\dot{m}_{OA}}{\dot{m}_{RA} + \dot{m}_{OA}} \qquad \text{Eq. (5.1)}$$

The exhalation air of the passenger contains more water vapor than the ambient air usually. Thereby, when the system operates with a high ψ_{OA}, the cabin maintains a low humidity ratio and dew point. For this reason, the condensing mode is not needed during high ψ_{OA} operating condition as shown in **Table 5.3**. However, the MHP operates more times for heating mode since the cold ambient air flow into the cabin. Hence, it leads to high energy consumption (see **Figure 5.8**). Meanwhile, when the system performs with the low ψ_{OA}, the results describe that waste heat recovery without dehumidification is not effectively helpful in energy saving, as mentioned above in **Section 5.3.1**. However, the energy reduction can be led by recovering

waste heat at the high ψ_{OA}. It is a reason that the heated air through the additional heat exchanger increases the evaporating temperature of IDEVA to reduce the compression ratio and improve the coefficient of performance (COP). Nevertheless, the case of utilized DCHE indicates slightly better performance than the plain heat exchanger cases, because the adsorption heat, that is generated while adsorbing moisture as following **Eq. (3.8)**, leads to a more increasing air temperature of the IDEVA inlet and evaporating temperature. Therefore, it appears that DCHE can reduce the heating energy compared to the base case, regardless of the mixing ratio of the ambient air (ψ_{OA}).

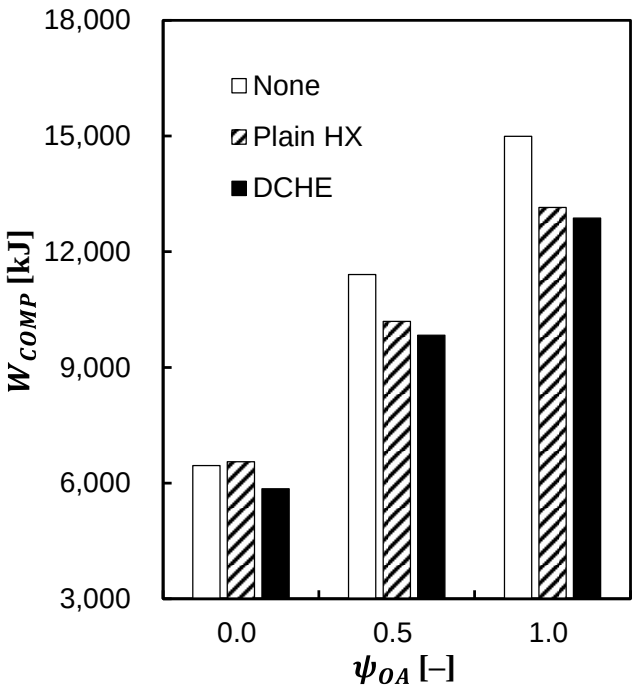

Figure 5.8 Energy consumption according to fresh-recirculation air ratio.

Table 5.3 Simulation conditions and results according to the fresh-recirculation air ratio.

Additional HX	T_{OA} [°C]	ψ_{OA} [−]	$T_{\mathrm{w,HX,in}}$ [°C]	t_{tot} ($t_{\mathrm{H}}/t_{\mathrm{C}}$) [s]	W_{COMP} [kJ]	Saving ratio [%]
None	**7**	**0**	20	3,700(3,328/372)	6,453	-
None	**7**	**0.5**	20	6,882(6,882/ 0)	11,409	−76.79
None	**7**	**1**	20	9,877(9,877/ 0)	14,993	−132.34
Plain HX	**7**	**0**	20	37,67(3,397/370)	6,556	−1.59
Plain HX	**7**	**0.5**	20	6,042(6,042/ 0)	10,194	−57.97
Plain HX	**7**	**1**	20	8,354(8,354/ 0)	13,149	−103.76
DCHE	**7**	**0**	20	3,228(3,228/ 0)	5,851	9.33
DCHE	**7**	**0.5**	20	5,796(5,796/ 0)	9,837	−52.43
DCHE	**7**	**1**	20	8,106(8,106/ 0)	12,874	−99.49

5.3.4. Effect of the ambient temperature

In **Section 2.5.1**, it observed that the heating load is correlated with the ambient air temperature. But the calculation of the heating load is obtained by only considering how much energy is required to reach the target air temperature. However, the MHP should operate to not only raising cabin air temperature but also to reduce moisture. To determine the effect of the outdoor temperature, a simulation is conducted.

As a result, energy consumption tends to show a negative correlation with the outdoor temperature, regardless of the existence and type of the additional heat exchanger, as presented in **Figure 5.9** and **Table 5.4**. The dehumidification process is more required for fog formation when the ambient temperature is lower. In the cases of utilized the plain heat exchanger, energy saving has not been achieved under various ambient temperatures because the system operates the condensing mode. On the other hand, in the case of DCHE, energy consumption is able to be reduced. The condensation mode is not performed despite the low outside temperature when the DCHE is applied in the system.

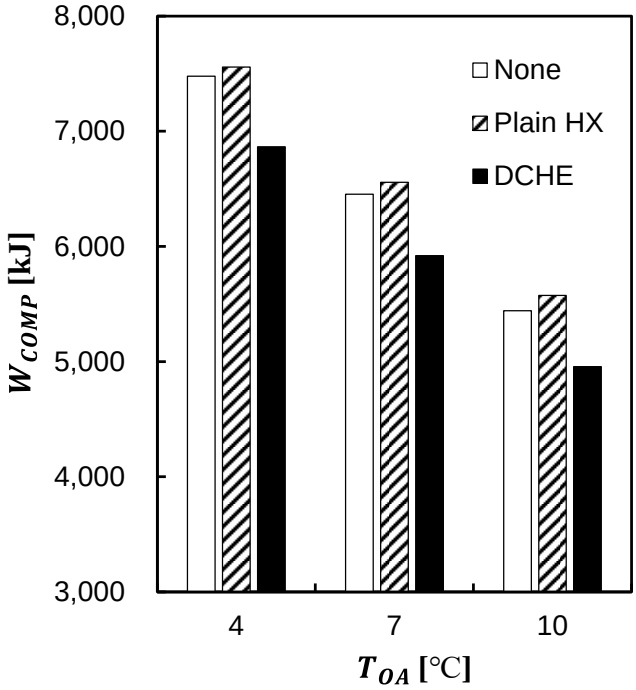

Figure 5.9 Energy consumption according to the ambient temperature at constant 65% relative humidity.

Table 5.4 Simulation conditions and results subjected to ambient temperature and the type of the additional heat exchanger.

Additional HX	T_{OA} [°C]	RH_{OA}[%] / w_{OA}[g/kg]	ψ_{OA} [–]	$T_{w,HX,in}$ [°C]	t_{tot} (t_H/t_C) [s]	W_{COMP} [kJ]	Saving ratio [%]
None	**7**	**65** / 4.02	0	20	3,700(3,328/372)	6,453	-
Plain HX	**7**	65 / 4.02	0	20	3,767(3,397/370)	6,556	−1.6
DCHE	**7**	65 / 4.02	0	20	3,269(3,269/ 0)	5,920	8.3
None	**4**	65 / 3.26	0	20	4,675(4,277/398)	7,478	−15.9
Plain HX	**4**	65 / 3.26	0	20	4,731(4,336/395)	7,558	−17.1
DCHE	**4**	65 / 3.26	0	20	4,150(4,150/ 0)	6,866	−6.4
None	**10**	65 / 4.94	0	20	2,880(2,525/355)	5,442	15.7
Plain HX	**10**	65 / 4.94	0	20	2,964(2,609/355)	5,574	13.6
DCHE	**10**	65 / 4.94	0	20	2,506(2,506/ 0)	4,955	23.2

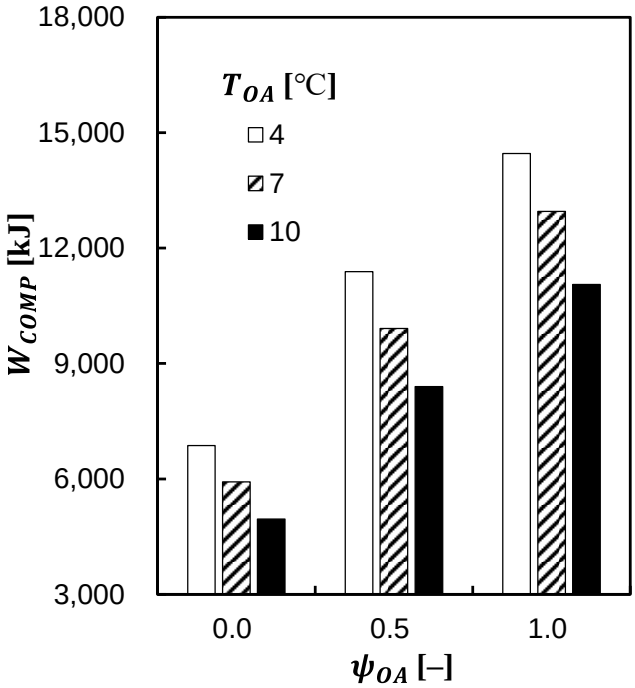

Figure 5.10 Energy consumption according to the ambient temperature at constant 65% relative humidity.

Table 5.5 Simulation conditions and results according to ambient temperature and the fresh-recirculation air ratio.

Additional HX	T_{OA} [°C]	RH_{OA}[%] / w_{OA}[g/kg]	ψ_{OA} [–]	$T_{w,HX,in}$ [°C]	t_{tot} (t_H/t_C) [s]	W_{COMP} [kJ]	Saving ratio [%]
DCHE	**4**	65 / 3.26	**0**	20	4,150(4,150/ 0)	6,866	−15.98
DCHE	**4**	65 / 3.26	**0.5**	20	7,452(7,452/ 0)	11,384	−92.31
DCHE	**4**	65 / 3.26	**1**	20	10,211(10,211/ 0)	14,459	−144.23
DCHE	**7**	**65** / 4.02	**0**	20	3,269(3,269/ 0)	5,920	-
DCHE	**7**	65 / 4.02	**0.5**	20	5,848(5,848/ 0)	9,913	−67.44
DCHE	**7**	65 / 4.02	**1**	20	8,170(8,170/ 0)	12,952	−118.78
DCHE	**10**	65 / 4.94	**0**	20	2,506(2,506/ 0)	4,955	16.30
DCHE	**10**	65 / 4.94	**0.5**	20	4,480(4,480/ 0)	8,400	−41.90
DCHE	**10**	65 / 4.94	**1**	20	6,242(6,242/ 0)	11,051	−86.68

5.3.5. Effect of the DCHE inlet coolant temperature

Based on the coolant temperature, the amount of heat recovery and the adsorption capacity are changed [20, 134]. Thereby, the simulation was conducted according to the coolant temperature that flows into the additional heat exchanger, plain HX or DCHE, to determine the energy consumption.

In case of the absence of the additional heat exchanger, i.e., 'None' in **Figure 5.11** and **Table 5.6**, the performance of the MHP stays constant regardless of the coolant temperature. Because there is no thermal connection between the coolant cycle and the refrigerant cycle. When the plain heat exchanger is utilized, the IDCOND outlet air temperature is raised up by heat recovery waste heat from the PEEM. It leads to the total MHP operation time is shortened and the energy consumption is reduced when the coolant temperature is higher than the target cabin air temperature ($T_{a,cabin,target}$=24°C), i.e. $T_{w,HX,in,D}$ is 25°C or 30°C. When the cold fluid is passed through the DCHE during dehumidification mode, the adsorption performance is enhanced as described in **Figure 3.17**. However, the energy is more required because the heating load might be increased by applying the cold brine into the additional heat exchanger. In the case of DCHE, the results show 9.3% and 36.7% energy saving by waste heat recovery at the coolant

temperature of 20 and 30°C, respectively. Because the DCHE leads to raising the cabin air temperature by waste heat recovery. Thus, the operation time is reduced by removing the water molecules in the cabin at an ambient air temperature of 7°C and coolant temperature of 20°C.

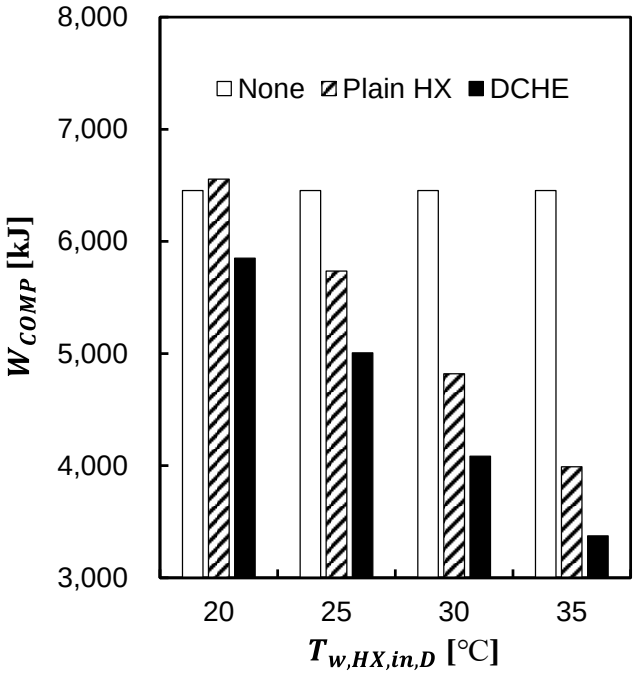

Figure 5.11 Energy consumption according to the coolant temperature.

Table 5.6 Simulation conditions and results according to coolant temperature.

Additional HX	T_{OA} [°C]	$T_{OA,WB}$[°C] / w_{OA}[g/kg]	ψ_{OA} [−]	$T_{w,HX,in,D}$ [°C]	t_{tot} (t_H/t_C) [s]	W_{COMP} [kJ]	Saving ratio [%]
None	7	6 / 5.39	0	**20**	3,700(3,328/372)	6,453	-
None	7	6 / 5.39	0	**25**	3,700(3,328/372)	6,453	0.00
None	7	6 / 5.39	0	**30**	3,700(3,328/372)	6,453	0.00
None	7	6 / 5.39	0	**35**	3,700(3,328/372)	6,453	0.00
Plain HX	7	6 / 5.39	0	**20**	3,767(3,397/370)	6,556	−1.6
Plain HX	7	6 / 5.39	0	**25**	3,274(2,901/373)	5,736	11.1
Plain HX	7	6 / 5.39	0	**30**	2,758(2,378/380)	4,819	25.3
Plain HX	7	6 / 5.39	0	**30**	2,303(1,920/383)	3,991	38.2
DCHE	7	6 / 5.39	0	**20**	3,228(3,228/ 0)	5,851	9.3
DCHE	7	6 / 5.39	0	**25**	2,735(2,735/ 0)	5,007	22.4
DCHE	7	6 / 5.39	0	**30**	2,224(2,224/ 0)	4,084	36.7
DCHE	7	6 / 5.39	0	**30**	1,829(1,829/ 0)	3,374	47.7

5.3.6. Effect of the number of the passenger

Since water vapor accumulates in the vehicle due to the exhalation of passengers, the fogging up on the windshield in the winter season. Hence, the ventilation or dehumidification process should be performed to defogging. The amount of water evaporating from a human body strongly corresponded to the number of passengers as calculating by **Eq. (2.9)**. Also, the number of passengers affects the heating load because the human body acts as a heat source as described in **Eq. (2.6)**.

To investigate the effect of the number of passengers, an energy analysis was conducted. As a result, less energy is required when increasing the number of passengers as shown in **Figure 5.12**. and **Table 5.7**. As the number of people increased, the time to reach the target air temperature became shorter since the heat generation of the human. In addition, the power consumption of the compressor is reduced because the heating load is decreased. However, the amount of discharged water vapor from passengers enlarges as increasing the number of persons. Thereby, the condensing mode is required when the system has not utilized the dehumidifier. When the DCHE is applied, the time to enter the condensing mode is shortened and the energy reduction effect is amplified.

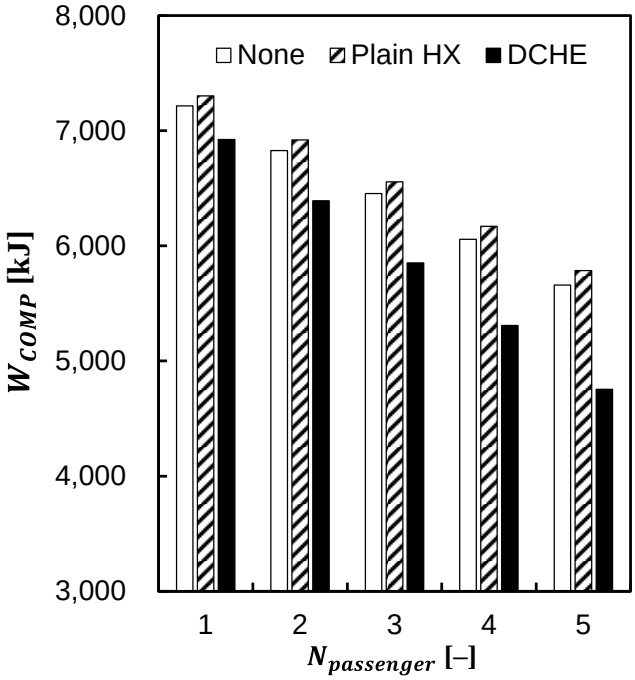

Figure 5.12 Energy consumption according to the number of the passenger.

Table 5.7 Simulation conditions and results according to the number of the passenger.

Additional HX	T_{OA} [°C]	$T_{OA,WB}$[°C] / w_{OA}[g/kg]	ψ_{OA} [–]	$T_{w,HX,in}$ [°C]	$N_{passenger}$ [–]	t_{tot} (t_H/t_C) [s]	W_{COMP} [kJ]	Saving ratio [%]
None	7	6 / 5.39	0	20	**1**	4,032(3,909/123)	7,215	−11.8
Plain HX	7	6 / 5.39	0	20	**1**	4,095(3,972/123)	7,303	−13.2
DCHE	7	6 / 5.39	0	20	**1**	3,820(3,820/ 0)	6,924	−7.3
None	7	6 / 5.39	0	20	**2**	3,863(3,615/248)	6,827	−5.8
Plain HX	7	6 / 5.39	0	20	**2**	3,927(3,678/249)	6,921	−7.2
DCHE	7	6 / 5.39	0	20	**2**	3,526(3,526/ 0)	6,391	1.0
None	7	6 / 5.39	0	20	**3**	3,700(3,328/372)	6,453	-
Plain HX	7	6 / 5.39	0	20	**3**	3,767(3,397/370)	6,556	−1.6
DCHE	7	6 / 5.39	0	20	**3**	3,228(3,228/ 0)	5,851	9.3
None	7	6 / 5.39	0	20	**4**	3,526(3,028/498)	6,056	6.2
Plain HX	7	6 / 5.39	0	20	**4**	3,596(3,102/494)	6,170	4.4
DCHE	7	6 / 5.39	0	20	**4**	2,929(2,929/ 0)	5,308	17.7
None	7	6 / 5.39	0	20	**5**	3,352(2,729/623)	5,660	12.3
Plain HX	7	6 / 5.39	0	20	**5**	3,427(2,805/622)	5,786	10.3
DCHE	7	6 / 5.39	0	20	**5**	2,625(2,625/ 0)	4,755	26.3

5.3.7. Effect of the refrigerant type

The thermal properties of a refrigerant are crucial to determine the performance of the heat pump. In the traditional MHP, the R-134a is used. However, the R-134a should be phased out because it is a high global warming potential (GWP) value as mentioned in **Section 4.1.1**. The considered alternative refrigerants are R-1234yf and R-152a. According to the refrigerant type, the energy analysis is conducted as shown in **Figure 5.13** and **Table 5.8**. As a result, the energy consumption of the R-1234yf slightly larger than the R-134a case. Because the R-1234yf discharge temperature of the compressor is lower than the R-134a case as depicted in **Figure 4.1**. Thus, the condensing pressure of the R-1234yf should be raised to heat exchange with the cabin air. It leads to increasing the compressor ratio and accretion of energy consumption. Meanwhile, the R-152a case shows better performance.

The effect of the fresh-recirculation ratio (ψ_{OA}) and refrigerant type is investigated in **Figure 5.14** and **Table 5.9**. Like Section 5.3.3., the energy consumption is enlarged under the high ψ_{OA} condition since the heating load is increase due to the entering the cold ambient air into the cabin.

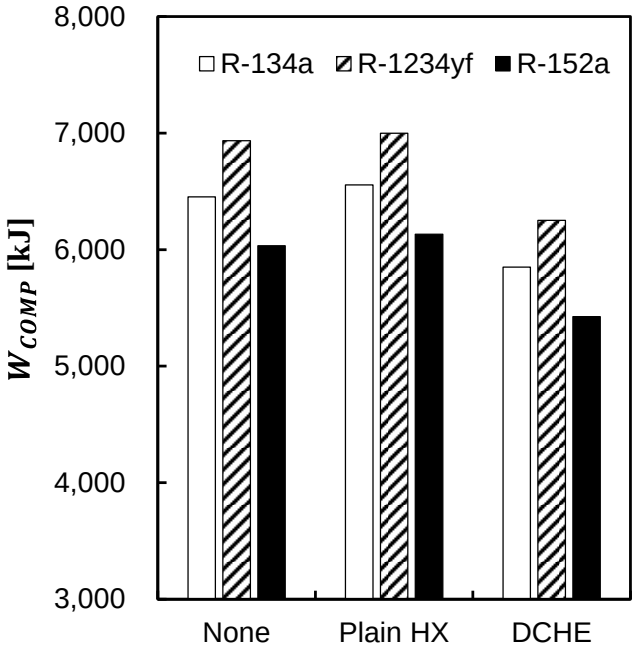

Figure 5.13 Energy consumption according to the type of refrigerant.

Table 5.8 Simulation conditions and results according to the refrigerant type of the heat pump system.

Refrigerant	Additional HX	T_{OA} [°C]	w_{OA} [g/kg]	ψ_{OA} [−]	$T_{w,HX,in}$ [°C]	t_{tot} (t_H/t_C) [s]	W_{COMP} [kJ]	Saving ratio [%]
R-134a	None	7	5.39	0	20	3,700(3,328/372)	6,453	-
R-134a	Plain HX	7	5.39	0	20	3,767(3,397/370)	6,556	-1.59
R-134a	DCHE	7	5.39	0	20	3,228(3,228/ 0)	5,851	9.33
R-1234yf	None	7	5.39	0	20	4,027(3,656/371)	6,934	-7.4
R-1234yf	Plain HX	7	5.39	0	20	4,087(3,719/368)	6,999	-8.5
R-1234yf	DCHE	7	5.39	0	20	3,484(3,484/ 0)	6,251	3.1
R-152a	None	7	5.39	0	20	3,898(3,502/396)	6,032	6.5
R-152a	Plain HX	7	5.39	0	20	3,963(3,570/393)	6,133	5.0
R-152a	DCHE	7	5.39	0	20	3,313(3,313/ 0)	5,424	15.9

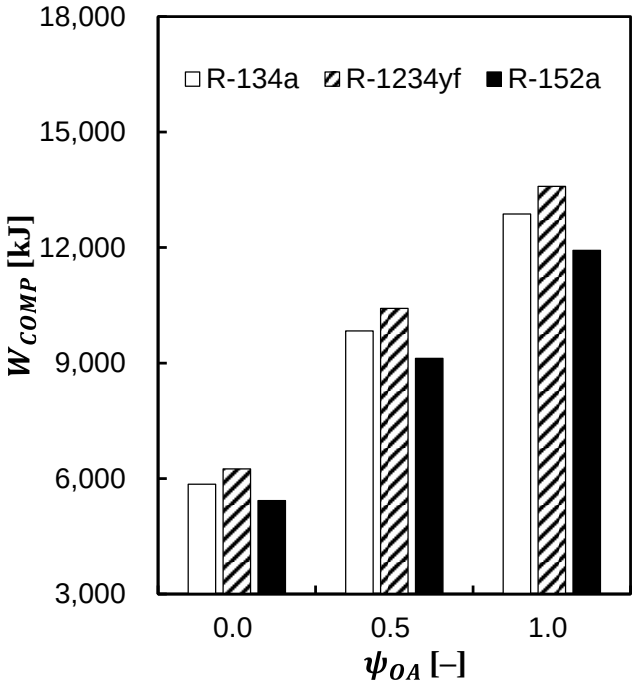

Figure 5.14 Energy consumption according to the type of the refrigerant and the fresh-circulation air ratio.

Table 5.9 Simulation conditions and results according to the refrigerant and the fresh-circulation air ratio.

Refrigerant	Additional HX	T_{OA} [°C]	w_{OA} [g/kg]	ψ_{OA} [−]	$T_{w,HX,in}$ [°C]	$t_{tot}(t_H/t_C)$ [s]	W_{COMP} [kJ]	Saving ratio [%]
R-134a	None	7	5.39	0	20	3,700(3,328/372)	6,453	-
R-134a	DCHE	7	5.39	**0**	20	3,228(3,228/ 0)	5,851	9.33
R-134a	DCHE	7	5.39	**0.5**	20	5,796(5,796/ 0)	9,837	−52.43
R-134a	DCHE	7	5.39	**1**	20	8,106(8,106/ 0)	12,874	−99.49
R-1234yf	DCHE	7	5.39	**0**	20	3,484(3,484/ 0)	6,251	3.1
R-1234yf	DCHE	7	5.39	**0.5**	20	6,258(6,258/ 0)	10,421	−61.5
R-1234yf	DCHE	7	5.39	**1**	20	8,620(8,620/ 0)	13,589	−110.6
R-152a	DCHE	7	5.39	**0**	20	3,313(3,313/ 0)	5,424	15.9
R-152a	DCHE	7	5.39	**0.5**	20	5,936(5,936/ 0)	9,125	−41.4
R-152a	DCHE	7	5.39	**1**	20	8,257(8,257/ 0)	11,929	−84.9

5.3.8. Effect of the number of the DCHE

The single DCHE is not able to operate the dehumidification mode continuously because it is needed that switching the dehumidification and regeneration mode. To overcome the problem, the double DCHE is introduced as illustrated in **Figure 5.15**. By applying the 4 ways valves, the air and coolant path will be controlled to switching. To considered the space for installing heat exchangers in an electric vehicle, the total frontal area of DCHEs is constrained to energy analysis.

As seen results of the energy analysis in **Figure 5.16** and **Table 5.10**, the double DCHE can be achieved energy saving. However, the positive effect seems not dramatic as considering the increasing the system complexity.

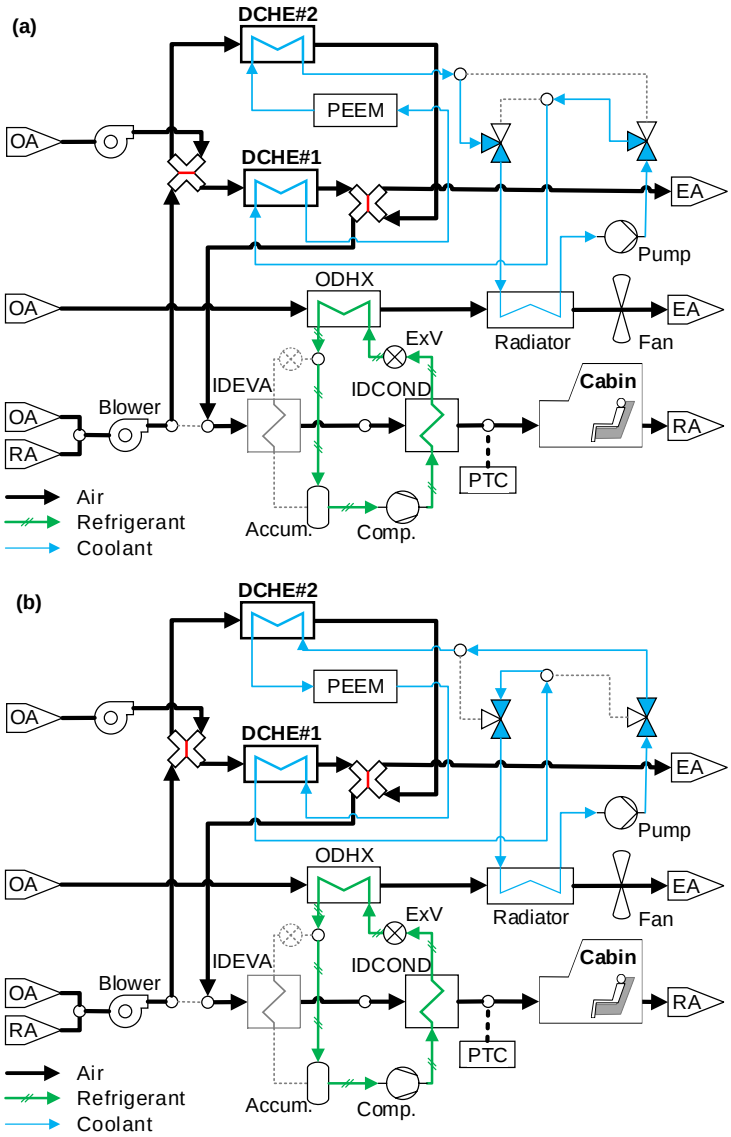

Figure 5.15 Schematic of the automotive heat pump system (MHP) with double desiccant coated heat exchanger (DCHE) for continuous operating. (a) DCHE#1 is in the dehumidification mode and DCHE#2 is in the regeneration mode, (b) DCHE#1 is in regeneration mode and DCHE#2 is in dehumidification mode.

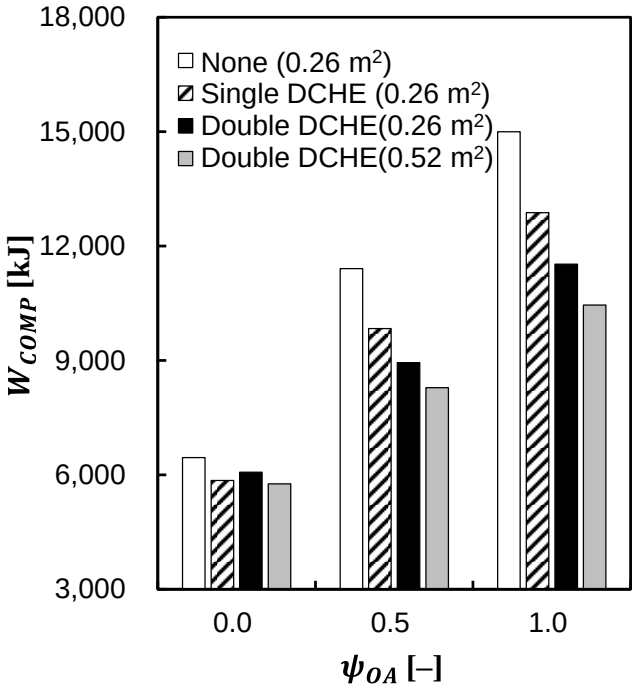

Figure 5.16 Energy consumption according to the number of the DCHE.

Table 5.10 Simulation conditions and results according to the number of the DCHE.

N_{DCHE} [EA]	$A_{HX,tot}$ [m^2]	L_{HX} [m]	Tube per row [EA]	T_{OA} [°C]	w_{OA} [g/kg]	ψ_{OA} [–]	$T_{w,HX,in}$ [°C]	t_{tot} (t_H/t_C) [s]	W_{COMP} [kJ]	Saving ratio [%]
None	0.26	0.50	24	7	5.39	**0**	20	3,700(3,328/372)	6,453	-
Single	0.26	0.50	24	7	5.39	**0**	20	3,228(3,228/ 0)	5,851	9.33
Single	0.26	0.50	24	7	5.39	**0.5**	20	5,796(5,796/ 0)	9,837	−52.43
Single	0.26	0.50	24	7	5.39	**1**	20	8,106(8,106/ 0)	12,874	−99.49
Double	**0.26**	**0.25**	24	7	5.39	**0**	20	3,364(3,364/ 0)	6,069	6.0
Double	0.26	0.25	24	7	5.39	**0.5**	20	5,169(5,169/ 0)	8,940	−38.5
Double	0.26	0.25	24	7	5.39	**1**	20	6,997(6,997/ 0)	11,522	−78.5
Double	**0.52**	0.50	24	7	5.39	**0**	20	3,184(3,184/ 0)	5,763	10.7
Double	0.52	0.50	24	7	5.39	**0.5**	20	4,738(4,738/ 0)	8,282	−28.3
Double	0.52	0.50	24	7	5.39	**1**	20	6,205(6,205/ 0)	10,452	−62.0

5.4. Summary

In this chapter, the simulation of the integrated system was conducted on various operating conditions to estimate the energy consumption for heating and defogging. The developed numerical models, which are discussed in previous sections, were interconnected within the Simulink program.

To examine the effect of the desiccant coated heat exchanger (DCHE) on energy consumption, simulation results were compared for three different configurations: The first system is a traditional case without an additional heat exchanger. The second configuration is a case that is adopted the plain heat exchanger without desiccant coating. The last case is the proposed system which is utilized the DCHE.

As a result, the application of DCHE led to an energy reduction of about 10%. Since the proposed MHP required less operation because the DCHE help to reduce the running time as condensing mode by capturing the moisture in the cabin air, and by heating to quickly reach the cabin air temperature to the target room temperature. As the lower the outside temperature and the higher the fresh-recirculation air ratio (ψ_{OA}), the higher the thermal load of the cabin, thus the energy consumption increase to satisfy the target condition. However, by adding an additional heat exchanger, the results were obtained that the reduced

energy consumption by recovery waste heat of the power electronics and electric machinery (PEEM). The more passengers board the vehicle, the positive effect of the DCHE on energy reduction is enhanced. The reason is that as the number of passenger increase, the defogging process is more required operation since the amount of released moisture from the human body increases. The traditional MHP increases the operating time in condensing mode for defogging, whereas the utilized DCHE case reveals that reduces the total operating time. Because the passenger's metabolic heat becomes a heat source and decreases the thermal load of the cabin. As a result of conducting a simulation considering the R-1234yf and the R-152a as alternative refrigerants by replacing the R-134a with high GWP, it was calculated that the case of the R-1234yf consumes about 7% more energy than the R-134a case, meanwhile, the R-152a consumes about 7% less than the R-134a case. However, in order to apply the R-152a in a vehicle, additional safety technologies might be necessary since the R-152a is classified as A2 (lower flammability) refrigerant according to the ASHARE standard [107].

Since the regeneration process of solid desiccant is inevitable to recover the adsorption performance, the system which is installed a single DCHE is difficult to operate continuously. To overcome the transmitting adsorption performance, double DCHEs were utilized and continuous operation was

carried out alternately. Even though the double DCHE case shows that less energy consumption than the single DCHE case, the reduction rate of energy consumption seems not dramatic significant as considering the increase in the complexity of the system.

Chapter 6. Conclusions

When an automotive heat pump system (MHP) consumes a lot of energy to deal with the heating loads in winter seasons, this causes a drastic decrease in the driving distance of the electric vehicle due to the MHP should operate for two purposes. The first purpose is heating the cabin air temperature to the target air temperature. The other aim of the MHP operation is defogging.

The conventional MHP operates to suit each purpose by controlling the expansion valves and solenoid valves. For sensible heating, the temperature of the cabin air increase by heat transfer through the indoor condenser (IDCOND), and the outdoor heat exchanger (ODHX) performs as an evaporator. Meanwhile, in order to dehumidify, the indoor evaporator (IDEVA) cools down the air temperature to lower than a dew point, then the water molecule condensates on the fins of IDEVA, thereby the air is dried. But the temperature of the dry air after dehumidification is too cold to supply into the cabin. Thus, the dry air should be heated up again. This process requires a lot of energy consumption. In this study, to overcome the drawback of the traditional MHP for dehumidification and heating, the solid desiccant is introduced in the dehumidification process since it is able to capture the moisture without condensing process.

In chapter 2, a cabin model was developed and calculated for the cabin thermal load and the passenger's moisture production. For this purpose, the cabin model was coded using mass and energy balances. The nonlinear ordinary differential equations were solved to obtain the thermal load of the cabin. The thermophysical and transport properties of wet air differ from dry air due to the content ratio of water vapor. For instance, the specific heat capacity is twice at the saturated state as comparing it of the dry air. The vehicle is postulated as light-duty. The cabin thermal load depends not only on the environmental conditions but also on the human metabolic rate and vehicle driving speed. The developed model is validated by comparing the results of the other researcher.

The model of the desiccant coated heat exchanger (DCHE) is evaluated in Chapter 3. In the first step, the dehumidifier material was selected through a literature survey to find a proper pair of solid desiccant and binder. In this study, the silica-gel and hydroxyethyl cellulose (HEC) were considered as the solid desiccant and the binder, respectively. In order to determine the optimum mixing ratio that is able to maximize the adsorption performance, the physical properties of the adsorbent were investigated. The physical properties of the adsorbent such as surface area, pore volume, and pore size were measured by the BET method. And the moisture uptake amount was determined by the water vapor sorption analyzer according to the binder contain ratio. Through the

analysis of the physical properties, the 5% weight percentage of HEC was selected. To investigate the adsorption and heat transfer performance of the DCHE, the numerical model was developed using thermal resistance. In order to validate the developed numerical model, experimental equipment was built, and experiments were performed under various conditions. As a result of comparing the experimental and simulation results, the predicted performance of the DCHE shows good agreement with the experimental data.

In Chapter 4, the mobile heat pump system is developed. The conventional automobile heat pump (MHP) has consisted of the compressor, heat exchangers, and expansion valves. Since the performance of the compressor is crucial upon the energy consumption. Thus, the preliminary study was conducted to measure the compressor characteristics such as isentropic efficiency, volumetric efficiency, and mechanical efficiency. The heat exchangers were modeled by divided into discrete segments. To validate the developed numerical model of the MHP, the experimental facility was constructed. The preceding test was conducted according to the refrigerant charge amount to achieve its optimum performance. Because the performance of the closed-loop cycle strongly depends on the charged amount of working media. After figure out the optimum charge amount, the experiment was conducted under the heating capacity rating

condition. In comparison with the experimental data, the numerical model of the MHP is validated.

In Chapter 5, the developed models were integrated into the Simulink platform to determine the effect of the DCHE on the energy consumption of the electric vehicle. Owing to comparison the results depend on the configuration, the base system is a traditional MHP. And the second system applied an additional heat exchanger without coating desiccant. Meanwhile, the proposed system is utilized with the DCHE. Simulation results show that the DCHE cases required less energy to satisfy the cabin target condition. Because the DCHE helps to reduce the running time as the condensing mode by capturing the moisture in the cabin air, and by heating to reach the cabin air temperature to the target room temperature quickly regardless of given conditions.

In conclusion, the DCHE was able to reduce energy consumption by capturing the water molecules in the air directly and recovering the waste heat of PEEM. It led to decreasing the MHP operating time and the power consumption of the compressor under all conditions considered in this study.

References

[1] W.M. Organization. WMO Statement on the State of the Global Climate in 2019. World Meteorological Organization2020.

[2] W.M. Organization. Global Annual to Decadal Climate Update 2019.

[3] R.K. Pachauri, M.R. Allen, V.R. Barros, J. Broome, W. Cramer, R. Christ, et al. Climate change 2014: synthesis report. Contribution of Working Groups I, II and III to the fifth assessment report of the Intergovernmental Panel on Climate Change. IPCC 2014.

[4] IEA, World Energy Balances. International Energy Agency, Paris, 2020.

[5] IEA, CO2 Emissions from Fuel Combustion. International Energy Agency, Paris, 2020.

[6] IEA, Global EV Outlook 2020. International Energy Agency, Paris, 2020.

[7] I. Burch, J. Gilchrist. Survey of global activity to phase out internal combustion engine vehicles. Center of Climate Protection: Santa Rosa, CA, USA2018.

[8] KIA. Kia Soul EV (PS EV) 2015-2020 Service Manual. in: KIAmotors, (Ed.).2020.

[9] AAA Electric Vehicle Range Testing Report. American Automobile Association, Inc. 2019.

[10] K. Liu, J. Wang, T. Yamamoto, T. Morikawa. Exploring the interactive effects

of ambient temperature and vehicle auxiliary loads on electric vehicle energy consumption. Applied Energy. 227 (2018) 324-31.

[11] Y. Higuchi, H. Kobayashi, Z. Shan, M. Kuwahara, Y. Endo, Y. Nakajima. Efficient Heat Pump System for PHEV/BEV. SAE International2017.

[12] K. Degirmenci, M.H. Breitner. Consumer purchase intentions for electric vehicles: Is green more important than price and range? Transportation Research Part D: Transport and Environment. 51 (2017) 250-60.

[13] L. Pérez-Lombard, J. Ortiz, C. Pout. A review on buildings energy consumption information. Energy and Buildings. 40 (2008) 394-8.

[14] P. Vivekh, M. Kumja, D.T. Bui, K.J. Chua. Recent developments in solid desiccant coated heat exchangers – A review. Applied Energy. 229 (2018) 778-803.

[15] N.A. Pennington. Humidity changer for air-conditioning. US Patent. US Patent, United States, 1955.

[16] M.C. Georg. Method for the manufacture of gas conditioning packing. US Patent, United States, 1968.

[17] R. Dunkle. Method of solar air conditioning. Mechanical and Chemical Transaction MCI. 1 (1965) 73-8.

[18] W.M. Worek, M. Chung-Ju. Simulation of an integrated hybrid desiccant vapor-compression cooling system. Energy. 11 (1986) 1005-21.

[19] P.L. Dhar, S.K. Singh. Studies on solid desiccant based hybrid air-conditioning systems. Applied Thermal Engineering. 21 (2001) 119-34.

[20] T.S. Ge, Y.J. Dai, R.Z. Wang, Z.Z. Peng. Experimental comparison and analysis on silica gel and polymer coated fin-tube heat exchangers. Energy. 35 (2010) 2893-900.

[21] Q. Ma, R.Z. Wang, Y.J. Dai, X.Q. Zhai. Performance analysis on a hybrid air-conditioning system of a green building. Energy and Buildings. 38 (2006) 447-53.

[22] C.S. Khalid Ahmed, P. Gandhidasan, A.A. Al-Farayedhi. Simulation of a hybrid liquid desiccant based air-conditioning system. Applied Thermal Engineering. 17 (1997) 125-34.

[23] K.C. Ng, H.T. Chua, C.Y. Chung, C.H. Loke, T. Kashiwagi, A. Akisawa, et al. Experimental investigation of the silica gel–water adsorption isotherm characteristics. Applied Thermal Engineering. 21 (2001) 1631-42.

[24] T.S. Ge, J.Y. Zhang, Y.J. Dai, R.Z. Wang. Experimental study on performance of silica gel and potassium formate composite desiccant coated heat exchanger. Energy. 141 (2017) 149-58.

[25] G. Restuccia, A. Freni, F. Russo, S. Vasta. Experimental investigation of a solid adsorption chiller based on a heat exchanger coated with hydrophobic zeolite. Applied Thermal Engineering. 25 (2005) 1419-28.

[26] P. Vivekh, M.R. Islam, K.J. Chua. Experimental performance evaluation of a composite superabsorbent polymer coated heat exchanger based air dehumidification system. Applied Energy. 260 (2020) 114256.

[27] Y. Fang, S. Zuo, X. Liang, Y. Cao, X. Gao, Z. Zhang. Preparation and performance of desiccant coating with modified ion exchange resin on finned tube heat exchanger. Applied Thermal Engineering. 93 (2016) 36-42.

[28] B. Park, S. Lee. Investigation on heat and mass transfer characteristics for a zeolite-coated heat exchanger using comparatively low-temperature energy: Heating humidification mode and cooling dehumidification mode. Indoor and Built Environment. (2020) 1420326X2094229.

[29] A. Myat, N. Kim Choon, K. Thu, Y.-D. Kim. Experimental investigation on the optimal performance of Zeolite–water adsorption chiller. Applied Energy. 102 (2013) 582-90.

[30] B.N. Truong, J. Park, O.K. Kwon, I. Park. Water adsorption capacity enhancement of ferroaluminophosphate (FAPO4-5) by impregnation of CaCl2. Materials Letters. 215 (2018) 137-9.

[31] L.J. Hua, X.Y. Sun, Y. Jiang, T.S. Ge, R.Z. Wang. Graphic general solutions for desiccant coated heat exchangers based on dimensional analysis. International Journal of Heat and Mass Transfer. 154 (2020) 119654.

[32] L. Liu, T. Zeng, H. Huang, M. Kubota, N. Kobayashi, Z. He, et al. Numerical

modelling and parametric study of an air-cooled desiccant coated cross-flow heat exchanger. Applied Thermal Engineering. 169 (2020) 114901.

[33] L.J. Hua, T.S. Ge, R.Z. Wang. A mathematical model to predict the performance of desiccant coated evaporators and condensers. International Journal of Refrigeration. 109 (2020) 188-207.

[34] T. Higashi, L. Zhang, M. Saikawa, M. Yamaguchi, C. Dang, E. Hihara. Theoretical and experimental studies on isothermal adsorption and desorption characteristics of a desiccant-coated heat exchanger. International Journal of Refrigeration. 84 (2017) 228-37.

[35] Y.D. Tu, R.Z. Wang, L.J. Hua, T.S. Ge, B.Y. Cao. Desiccant-coated water-sorbing heat exchanger: Weakly-coupled heat and mass transfer. International Journal of Heat and Mass Transfer. 113 (2017) 22-31.

[36] X. Zheng, R. Wang, W. Ma. Dehumidification assessment for desiccant coated heat exchanger systems in different buildings and climates: Fast choice of desiccants. Energy and Buildings. 221 (2020) 110083.

[37] Y.D. Tu, R.Z. Wang, T.S. Ge. New concept of desiccant-enhanced heat pump. Energy Conversion and Management. 156 (2018) 568-74.

[38] M. Suzuki. Application of adsorption cooling systems to automobiles. Heat Recovery Systems and CHP. 13 (1993) 335-40.

[39] S. Vasta, A. Freni, A. Sapienza, F. Costa, G. Restuccia. Development and lab-

test of a mobile adsorption air-conditioner. International Journal of Refrigeration. 35 (2012) 701-8.

[40] A. Alahmer. Thermal analysis of a direct evaporative cooling system enhancement with desiccant dehumidification for vehicular air conditioning. Applied Thermal Engineering. 98 (2016) 1273-85.

[41] C.-C.D. Huang. A Dynamic Computer Simulation Model for Automobile Passenger Compartment Climate Control and Evaluation. Michigan Technological University1998.

[42] A.E.-S.A.E. Gado. Development of a dynamic test facility for environmental control systems. 2006.

[43] F. Brèque, M. Nemer. Cabin Thermal Needs: Modeling and Assumption Analysis. Proceedings of the 12th International Modelica Conference, Prague, Czech Republic, May 15-17, 2017. Linköping University Electronic Press2017. pp. 771-81.

[44] J.P. Rugh, R.B. Farrington, J.A. Boettcher. The Impact of Metal-free Solar Reflective Film on Vehicle Climate Control. SAE International2001.

[45] R. Levinson, H. Pan, G. Ban-Weiss, P. Rosado, R. Paolini, H. Akbari. Potential benefits of solar reflective car shells: Cooler cabins, fuel savings and emission reductions. Applied Energy. 88 (2011) 4343-57.

[46] H. Khayyam, A.Z. Kouzani, E.J. Hu, S. Nahavandi. Coordinated energy

management of vehicle air conditioning system. Applied Thermal Engineering. 31 (2011) 750-64.

[47] G.T. Kim. (An) Integrated Electric Vehicle Thermal Management System for Range Extension. Seoul national university, Seoul, 2020.

[48] D. Du Bois, E.F. Du Bois. Clinical Calorimetry Archives of Internal Medicine. XVII (1916) 863.

[49] K. Gładyszewska-Fiedoruk, T.J. Teleszewski. Modeling of Humidity in Passenger Cars Equipped with Mechanical Ventilation. Energies. 13 (2020) 2987.

[50] E. Bruck. Water in expired air: Physiology and measurement. The Journal of Pediatrics. 60 (1962) 869-81.

[51] N.A. Taylor, C.A. Machado-Moreira. Regional variations in transepidermal water loss, eccrine sweat gland density, sweat secretion rates and electrolyte composition in resting and exercising humans. Extreme Physiology & Medicine. 2 (2013) 4.

[52] P.O. Fanger. Thermal comfort. Analysis and applications in environmental engineering. Copenhagen: Danish Technical Press.1970.

[53] L. Ferrus, H. Guenard, G. Vardon, P. Varene. Respiratory water loss. Respir Physiol. 39 (1980) 367-81.

[54] M. Akdeniz, S. Gabriel, A. Lichterfeld-Kottner, U. Blume-Peytavi, J. Kottner.

Transepidermal water loss in healthy adults: a systematic review and meta-analysis update. Br J Dermatol. 179 (2018) 1049-55.

[55] H. Lee, Y. Hwang, I. Song, K. Jang. Transient thermal model of passenger car's cabin and implementation to saturation cycle with alternative working fluids. Energy. 90 (2015) 1859-68.

[56] L. Zhang, K. Hashimoto, H. Hasegawa, M. Saikawa. Performance analysis of a heat pump system with integrated desiccant for electric vehicles. International Journal of Refrigeration. 86 (2018) 154-62.

[57] P.T. Tsilingiris. Review and critical comparative evaluation of moist air thermophysical properties at the temperature range between 0 and 100 °C for Engineering Calculations. Renewable and Sustainable Energy Reviews. 83 (2018) 50-63.

[58] A. Wexler, R. Hyland, R. Stewart. Thermodynamic properties of dry air, moist air and water and SI psychrometric charts. ASHRAE1983.

[59] ASHRAE, Handbook: Fundamentals 2017. American Society of Heating, Refrigerating and Air-Conditioning Engineers2017.

[60] F.H. Rohles. Thermal Sensations of Sedentary Man in Moderate Temperatures. Human Factors. 13 (1971) 553-60.

[61] A. Rosca, L. Tecnico. Light duty vehicle test cycle generation based on real-world data. Master thesis. (2013).

[62] X.-J. Zhang. Van der Waals Forces. in: Q.J. Wang;, Y.-W. Chung, (Eds.), Encyclopedia of Tribology. Springer, Boston, MA, USA, 2013. pp. 3945-7.

[63] J. Do, D. Cha, I. Park, O.K. Kwon, J. Bae, J. Park. Hydrothermal synthesis and application of adsorbent coating for adsorption chiller. Progress in Organic Coatings. 128 (2019) 59-68.

[64] J. Canivet, A. Fateeva, Y. Guo, B. Coasne, D. Farrusseng. Water adsorption in MOFs: fundamentals and applications. Chem Soc Rev. 43 (2014) 5594-617.

[65] S.H. Kim, K. Cho, J.-N. Kim, H.T. Beum, H.C. Yoon, C.H. Lee. Improvement of cooling performance of water adsorption chiller by using aluminophophate adsorbent. Microporous and Mesoporous Materials. 309 (2020) 110572.

[66] E.-P. Ng, S. Mintova. Nanoporous materials with enhanced hydrophilicity and high water sorption capacity. Microporous and Mesoporous Materials. 114 (2008) 1-26.

[67] B. Dawoud, Y. Aristov. Experimental study on the kinetics of water vapor sorption on selective water sorbents, silica gel and alumina under typical operating conditions of sorption heat pumps. International Journal of Heat and Mass Transfer. 46 (2003) 273-81.

[68] H.T. Chua, K.C. Ng, A. Chakraborty, N.M. Oo, M.A. Othman. Adsorption Characteristics of Silica Gel + Water Systems. Journal of Chemical & Engineering Data. 47 (2002) 1177-81.

[69] K.S.W. Sing. Reporting physisorption data for gas/solid systems with special reference to the determination of surface area and porosity. Pure and Applied Chemistry. 57 (1985) 603-19.

[70] A. Li, K. Thu, A.B. Ismail, M.W. Shahzad, K.C. Ng. Performance of adsorbent-embedded heat exchangers using binder-coating method. International Journal of Heat and Mass Transfer. 92 (2016) 149-57.

[71] M.M. Younes, I.I. El-sharkawy, A.E. Kabeel, K. Uddin, A. Pal, S. Mitra, et al. Synthesis and characterization of silica gel composite with polymer binders for adsorption cooling applications. International Journal of Refrigeration. 98 (2019) 161-70.

[72] A. Li. Experimental and theoretical studies on the heat transfer enhancement of adsorbent coated heat exchangers. Department of mechanical engineering. National University of Singapore2014.

[73] S. Brunauer, P.H. Emmett, E. Teller. Adsorption of Gases in Multimolecular Layers. Journal of the American Chemical Society. 60 (1938) 309-19.

[74] G. Fagerlund. Determination of specific surface by the BET method. Matériaux et Constructions. 6 (1973) 239-45.

[75] M. Thommes, K. Kaneko, A.V. Neimark, J.P. Olivier, F. Rodriguez-Reinoso, J. Rouquerol, et al. Physisorption of gases, with special reference to the evaluation of surface area and pore size distribution (IUPAC Technical Report). Pure and

Applied Chemistry. 87 (2015) 1051-69.

[76] I. Langmuir. The adsorption of gases on plane surfaces of glass, mica and platinum. Journal of the American Chemical Society. 40 (1918) 1361-403.

[77] R. Bardestani, G.S. Patience, S. Kaliaguine. Experimental methods in chemical engineering: specific surface area and pore size distribution measurements—BET, BJH, and DFT. The Canadian Journal of Chemical Engineering. 97 (2019) 2781-91.

[78] K. Sing. The use of nitrogen adsorption for the characterisation of porous materials. Colloids and Surfaces A: Physicochemical and Engineering Aspects. 187-188 (2001) 3-9.

[79] E.P. Barrett, L.G. Joyner, P.P. Halenda. The determination of pore volume and area distributions in porous substances. I. Computations from nitrogen isotherms. Journal of the American Chemical society. 73 (1951) 373-80.

[80] S. Lowell, J.E. Shields, M.A. Thomas, M. Thommes. Characterization of porous solids and powders: surface area, pore size and density. Springer Science & Business Media2012.

[81] National Center for Biotechnology Information, PubChem Compound Summary for CID 4327536, Hydroxyethylcellulose. National Library of Medicine (US)2021.

[82] A. Nuhnen, C. Janiak. A practical guide to calculate the isosteric heat/enthalpy

of adsorption via adsorption isotherms in metal–organic frameworks, MOFs. Dalton Transactions. 49 (2020) 10295-307.

[83] S. Poyet, S. Charles. Temperature dependence of the sorption isotherms of cement-based materials: Heat of sorption and Clausius–Clapeyron formula. Cement and Concrete Research. 39 (2009) 1060-7.

[84] V. Gnielinski. New equations for heat and mass transfer in turbulent pipe and channel flow. International Journal of Chemical Engineering. 16 (1976) 359-68.

[85] C.-C. Wang, K.-Y. Chi, C.-J. Chang. Heat transfer and friction characteristics of plain fin-and-tube heat exchangers, part II: Correlation. International Journal of Heat and Mass Transfer. 43 (2000) 2693-700.

[86] T.E. Schmidt. Heat transfer calculations for extended surfaces. Refrigerating Engineering. 57 (1949) 351-7.

[87] Y. Zhao, Y.J. Dai, T.S. Ge, X.Y. Sun, R.Z. Wang. On heat and moisture transfer characteristics of a desiccant dehumidification unit using fin tube heat exchanger with silica gel coating. Applied Thermal Engineering. 91 (2015) 308-17.

[88] A.K. Coker. CHAPTER 2 - Physical Property of Liquids and Gases. in: A.K. Coker, (Ed.). Fortran Programs for Chemical Process Design, Analysis, and Simulation. Gulf Professional Publishing, Houston, 1995. pp. 103-49.

[89] J. Welty, G.L. Rorrer, D.G. Foster. Fundamentals of momentum, heat, and mass transfer. John Wiley & Sons2020.

[90] J. Sercombe, R. Vidal, C. Gallé, F. Adenot. Experimental study of gas diffusion in cement paste. Cement and concrete research. 37 (2007) 579-88.

[91] A.A. Pesaran, A.F. Mills. Moisture transport in silica gel packed beds—II. Experimental study. International Journal of Heat and Mass Transfer. 30 (1987) 1051-60.

[92] H. Kang, G. Lee, D.-Y. Lee. Explicit analytic solution for heat and mass transfer in a desiccant wheel using a simplified model. Energy. 93 (2015) 2559-67.

[93] ASHRAE, Laboratory Methods of Testing Fans for Certified Aerodynamic Performance Rating (ANSI/AMCA 210-07, ANSI/ASHRAE 51-07). Air Movement and Control Association2008.

[94] J.P. Holman. Experimental Methods for Engineers2012.

[95] ASHRAE_guideline_Engineering Analysis of Experimental data2010.

[96] Kigali Amendment, The Amendment to the Montreal Protocol Agreed by the Twenty-Eighth Meeting of the Parties. UNEP Ozone Secretariat. (2016).

[97] Regulation (EU) No 517/2014 of the European Parliament and of the Council of 16 April 2014 on fluorinated greenhouse gases and repealing Regulation (EC) No 842/2006. Official Journal of the European Union. 20.5 (2014).

[98] Directive 2006/40/EC of the European Parliament and of the Council of 17 May

2006 relating to emissions from air conditioning systems in motor vehicles and amending Council Directive 70/156/EEC Official Journal of the European Union. 14.6 (2006).

[99] L. Cremaschi, X. Wu, A. Biswas, P. Deokar. Experimental study of compressor operating characteristics and performance when using refrigerants R32, R1234yf, and two new low GWP developmental refrigerants as drop-in replacements for R410A. 8th International Conference on Compressors and their Systems. Woodhead Publishing2013. pp. 57-66.

[100] D. Demma. Compressor Overheating. Sporlan Division of Parker Hannifin Corporation, Washington, MO, USA, 2005.

[101] H.-S. Sim, Y.-C. Lee, S.-C. Cha. Studies on Surface Defects of Enamel Coated Magnet Wires. IEEE.

[102] S. Simmons. ASHRAE, UN Environment Programme Announce Lower GWP Award Selections. ASHRAE, Atlanta, GA, USA, 2019.

[103] The availability of refrigerants for new split air conditioning systems that can replace fluorinated greenhouse gases or result in a lower climate impact The European Partnership for Energy and the Environment (EPEE), European Commission (EC), Brussels, Belgium, 2020.

[104] M. Ghodbane, T.D. Craig, J.A. Baker. Demonstration of an energy-efficient secondary loop HFC-152a mobile air conditioning system. (2007).

[105] K. Li, D. Xu, J. Lan, L. Su, Y. Fang. An experimental and theoretical investigation of refrigerant charge on a secondary loop air-conditioning heat pump system in electric vehicles. International Journal of Energy Research. 43 (2019) 3381-98.

[106] S. Andersen, S. Chowdhury, T. Craig, S. Kapoor, J. Meena, P. Nagarhalli, et al. Comparative Manufacturing and Ownership Cost Estimates for Secondary Loop Mobile Air Conditioning Systems (SL-MACs). SAE International2017.

[107] ANSI/ASHRAE Standard 34, Designation and Safety Classification of Refrigerants. American Society of Heating, Refrigerating and Air-Conditioning Engineers, Georgia, USA, 2019.

[108] S. Gligorovski, R. Strekowski, S. Barbati, D. Vione. Environmental Implications of Hydroxyl Radicals (•OH). Chemical Reviews. 115 (2015) 13051-92.

[109] P.A. Domanski, R. Brignoli, J.S. Brown, A.F. Kazakov, M.O. McLinden. Low-GWP refrigerants for medium and high-pressure applications. International Journal of Refrigeration. 84 (2017) 198-209.

[110] L. Huang. Energy and exergy performance comparison of different HFC/R1234yf mixtures in vapor-compression cycles. Journal of Thermal Analysis and Calorimetry. 140 (2020) 2447-59.

[111] Y. Wu, X. Liang, X. Tu, R. Zhuang. Study of R161 refrigerant for residential

air-conditioning applications. (2012).

[112] M. Youbi-Idrissi, J. Bonjour. The effect of oil in refrigeration: Current research issues and critical review of thermodynamic aspects. International Journal of Refrigeration. 31 (2008) 165-79.

[113] B. Shen, E. Groll. Review Article: A Critical Review of the Influence of Lubricants on the Heat Transfer and Pressure Drop of Refrigerants, Part 1: Lubricant Influence on Pool and Flow Boiling. HVAC&R Research. 11 (2005) 341-59.

[114] B. Shen, E. Groll. Review Article: A Critical Review of The Influence of Lubricants on the Heat Transfer and Pressure Drop of Refrigerants—Part II: Lubricant Influence on Condensation and Pressure Drop. HVAC&R Research. 11 (2005) 511-26.

[115] BITZER. Refrigerant report 21. 2020.

[116] S.B. Hong, J.W. Yoo, M.S. Kim. A theoretical refrigerant charge prediction equation for air source heat pump system based on sensor information. International Journal of Refrigeration. 104 (2019) 335-43.

[117] Y.H. Eom, J.W. Yoo, S.B. Hong, M.S. Kim. Refrigerant charge fault detection method of air source heat pump system using convolutional neural network for energy saving. Energy. 187 (2019) 115877.

[118] F.W. Dittus, L.M.K. Boelter. Heat transfer in automobile radiators of the tubular

type. International Communications in Heat and Mass Transfer. 12 (1985) 3-22.

[119] S. Koyama, K. Kuwahara, K. Nakashita, K. Yamamoto. An experimental study on condensation of refrigerant R134a in a multi-port extruded tube. International Journal of Refrigeration. 26 (2003) 425-32.

[120] S. Smith. Void fractions in two-phase flow: a correlation based upon an equal velocity head model. Heat and Fluid Flow. 1 (1971) 22-39.

[121] M.-H. Kim, C.W. Bullard. Air-side thermal hydraulic performance of multi-louvered fin aluminum heat exchangers. International Journal of Refrigeration. 25 (2002) 390-400.

[122] L. Sun, K. Mishima. An evaluation of prediction methods for saturated flow boiling heat transfer in mini-channels. International Journal of Heat and Mass Transfer. 52 (2009) 5323-9.

[123] R.J. Dossat. Principles of refrigeration. John Wiley & Son1961.

[124] ASHRAE Standard 41.2, Standard methods for laboratory air-flow measurement. American Society of Heating, Refrigerating and Air-Conditioning Engineers, Atlanta, 1987.

[125] P. Mithraratne, N.E. Wijeysundera. An experimental and numerical study of hunting in thermostatic-expansion-valve-controlled evaporators. International Journal of Refrigeration. 25 (2002) 992-8.

[126] R.J. Otten. Superheat control for air conditioning and refrigeration systems:

Simulation and experiments. Mechanical Engineering. University of Illinois at Urbana-Champaign, Urbana, Illinois, USA, 2010.

[127] M.J. Moran, H.N. Shapiro, D.D. Boettner, M.B. Bailey. Fundamentals of engineering thermodynamics. John Wiley & Sons2010.

[128] K. Seong, D. Lee, J. Lee. The Effects of Wet Compression by the Electronic Expansion Valve Opening on the Performance of a Heat Pump System. Applied Sciences. 7 (2017) 248.

[129] A.K. Dutta, T. Yanagisawa, M. Fukuta. A study on compression characteristic of wet vapor refrigerant. International Compressor Engineering Conference1996. p. 1112.

[130] SAE. Procedure for Measuring System COP [Coefficient of Performance] of a Mobile Air Conditioning System on a Test Bench. International Surface Vehicle Standard2008.

[131] ISO. 16358-2:2013, Air-cooled air conditioners and air-to-air heat pumps — Testing and calculating methods for seasonal performance factors — Part 2: Heating seasonal performance factor. the International Organization for Standardization2013.

[132] ISO. 5151:2017, Non-ducted air conditioners and heat pumps — Testing and rating for performance. the International Organization for Standardization2017.

[133] S.-I. Na, Y. Chung, M.S. Kim. Performance analysis of an electric vehicle heat

pump system with a desiccant dehumidifier. Energy Conversion and Management. 236 (2021) 114083.

[134] P. Vivekh, D.T. Bui, M.R. Islam, K. Zaw, K.J. Chua. Experimental performance and energy efficiency investigation of composite superabsorbent polymer and potassium formate coated heat exchangers. Applied Energy. 275 (2020) 115428.

국 문 초 록

차량 탑승객의 열쾌적성과 운전 안전성 확보를 위하여, 냉난방 공조 시스템을 가동하여 차량실내 냉난방 및 김서림 제거한다. 이러한 공조시스템을 운전하기 위한 에너지 소비는 불가피하다. 기존 내연기관 차량의 경우, 충분한 연소열량을 활용하여 난방 및 김서림 방지를 위해 사용할 수 있었다. 하지만 전기자동차의 경우, 내연기관 차량과 달리 충분한 열원이 존재하지 않을뿐더러 탑재된 배터리에 저장된 에너지량에 따라 주행거리가 의존적이므로, 공조시스템을 운전할수록 전기자동차의 주행거리가 급감하는 문제가 존재한다. 이를 해결하기 위해서는 공조시스템의 에너지 사용량을 줄이고 효율을 높여야 한다. 기존 차량에서는 김서림 제거를 위하여, 실내공기를 이슬점보다 낮게 만들어 공기내 수분이 열교환기에 응축시켜 제습한 후 재가열하여 실내로 공급하는 방법을 보편적으로 사용하고 있다. 이는 불합리적인 에너지 소비를 야기한다. 이러한 문제를 해결하기 위해, 고체 제습제를 활용하여 공기내 수분을 직접 흡착시켜 제습하는 방안을 고안하였다. 또한, 모터 및 인버터와 같은 전장품들의 폐열을 회수하여 공조에 활용하기 위해 추가 열교환기를 고려하였다.

본 연구에서, 제습제 코팅 열교환기 (DCHE, Desiccant coated heat exchanger)를 제안하고, 해당 열교환기를 적용한 전기자동차용 히트펌프 시스템의 에너지 사용량에 대한 분석을 실시하였다. 이를 위하여, 차량실내 열적 모델, 제습제 코팅 열교환기 모델, 그리고 차량용 히트펌프 모델을 구축 및 검증하였다. 탑승자의 호흡 및 피부에서 증발하는 수분량을 계산하여 차량실내 열적 모델을 구축하고, 다른 연구진의 모델과 비교 검증하였다. 제습제 코팅 열교환기의 해석 모델을 열 및 물질 저항 모델을 활용하여 차분화하여 구축하였다. 이 해석 모델을 검증하기 위하여, 다양한 조건에서 DCHE 의 흡착 성능측정을 실험하여 그 결과를 예측

성능과 비교하였다. 제습제 코팅 열교환기는 흡착제와 접착제의 비율에 따른 흡착성능을 분석한 결과를 바탕으로 제작하였다. 차량용 히트펌프 실험장비를 구축하고 다양한 조건에서 실험하였으며, 그 결과를 차량용 히트펌프 해석 모델의 예측 성능값과 비교하여 검증하였다. 따라서, 개발 및 검증된 모델을 Simulink 에 활용하여 다양한 운전조건에 대한 시스템의 소비동력에 미치는 영향을 분석하였다. 그 결과, 기존 전기자동차에 비하여 제습제 코팅 열교환기를 적용할 경우, 차량용 히트펌프의 냉매압축기 소비동력이 줄어든다는 결론을 얻었다.

본 연구에서 제시한 제습제 코팅 열교환기를 전기자동차에 적용한다면, 전기자동차용 공조시스템이 사용하는 에너지를 줄임으로써, 겨울철 차량의 주행거리를 확보할 수 있을 뿐만 아니라 미래 전기자동차의 보급 및 확산에도 기여할 수 있을 것으로 기대한다.

주요어: 전기자동차, 제습, 흡착, 열교환기, 열펌프

학 번: 2017-36824